PSFC/RR-08-2

Thermal Equilibrium Theory of Periodically Focused Charged-Particle Beams

Samokhvalova, K.R.

Plasma Science and Fusion Center
Massachusetts Institute of Technology
Cambridge MA 02139 USA

This work was supported by the U.S. Department of Energy, Office of High-Energy Physics, Grant No. DE-FG02-95ER40919, and Air Force Office of Scientific Research, Grant No. FA9550-06-1-0269.

Thermal Equilibrium Theory of Periodically Focused Charged-Particle Beams

by

Ksenia R. Samokhvalova

M.S. Physics, Nizhniy Novgorod State University, Russia (2003)
B.S. Physics, Nizhniy Novgorod State University, Russia (2001)

Submitted to the Department of Nuclear Science and Engineering
in Partial Fulfillment of the Requirements for the Degree of

Doctor of Philosophy

at the

MASSACHUSETTS INSTITUTE OF TECHNOLOGY
June 2008

Author……
Department of Nuclear Science and Engineering
March 18, 2008

Certified by……....
Chiping Chen
Principal Research Scientist
Thesis Supervisor

Certified by……
Jeffrey P. Freidberg
Professor of Nuclear Science and Engineering
Thesis Reader

Accepted by…….....
Jacquelyn C. Yanch
Professor of Nuclear Science and Engineering
Chairman, Department Committee on Graduate Students

Thermal Equilibrium Theory of Periodically Focused Charged-Particle Beams

by
Ksenia R. Samokhvalova
Submitted to the Department of Nuclear Science and Engineering
on March 18, 2008 in Partial Fulfillment of the Requirements for the Degree of
Doctor of Philosophy

Abstract

A thermal equilibrium theory of periodically focused charged-particle beams is presented in the framework of both warm-fluid and kinetic descriptions. In particular, the thermal beam equilibria are discussed for paraxial beams in periodic solenoidal and quadrupole magnetic focusing fields, and the theory is compared with the experimental measurements.

A warm-fluid equilibrium theory for a thermal beam in a periodic solenoidal focusing field is presented. The warm-fluid beam equilibrium equations are solved in the paraxial approximation, and the beam density and flow velocity are obtained. The self-consistent root-mean-square (rms) beam envelope equation and the self-consistent Poisson equation, governing the beam density and potential distributions, are derived. The beam equilibrium is adiabatic, i.e., there is no heat flow in the system, which results in rms beam emittance being conserved. The beam temperature is constant across the cross-section of the beam. For high-intensity beams, the beam density profile is flat in the center of the beam and falls off rapidly within a few Debye lengths at the edge of the beam. Such density profile provides a more realistic representation of a laboratory beam than the uniform density profile in the Kapchinskij-Vladimirskij beam equilibrium which had been used in experimental data analyses.

A kinetic equilibrium theory for the thermal beam in the periodic solenoidal focusing field, which is equivalent to the warm-fluid equilibrium theory, is also presented. The Hamiltonian for single-particle motion is analyzed to find the approximate and exact invariants of motion, i.e., a scaled transverse Hamiltonian (nonlinear space charge included) and the angular momentum, from which a Maxwell-Boltzmann-like beam equilibrium distribution is constructed. The approximation of the scaled transverse Hamiltonian as an invariant of motion is validated analytically for highly emittance-dominated beams and highly space-charge-dominated beams, and numerically tested to be valid for cases in between with moderate vacuum phase advances ($\sigma_v < 90°$). The beam envelope and emittances are determined self-consistently with the beam equilibrium distribution.

A warm-fluid equilibrium theory for a thermal beam in a periodic quadrupole magnetic (AG) focusing field is presented. The beam equilibrium is adiabatic. The warm-

fluid beam equilibrium equations are solved in the paraxial approximation. The rms beam envelope equations and the self-consistent Poisson equation, governing the beam density and potential distributions, are derived. It is shown numerically that the equilibrium equipotential contours and constant density contours are ellipses. Because the thermal beam equilibrium is adiabatic, the 4D thermal rms emittance of the beam is conserved. For high-intensity beams, the beam density profile is flat in the center of the beam and falls off rapidly within a few Debye lengths, which is similar to the beam density profile in the periodic solenoidal focusing field. An interesting property of the equilibrium is that the rate at which the density falls is transversely isotropic.

Quantitative comparisons are made between the thermal equilibrium theories and recent experiments at the University of Maryland Electron Ring [S. Bernal, B. Quinn, M. Reiser and P. G. O'Shea, Phys. Rev. Special Topics – Accel. Beams **5**, 064202 (2002); S. Bernal, R. A. Kishek, M. Reiser, and I. Haber, Phys. Rev. Lett. **82**, 4002 (1999)]. In the case of the periodic solenoidal focusing experiment, good agreement is found between theory and the experimental measurements from the anode aperture to a distance prior to wave breaking. In the case of the AG focusing experiment, there is reasonably good agreement between the theoretical and experimentally measured density profiles in one transverse direction along which the beam is close to equilibrium.

Thesis supervisor: Chiping Chen
Title: Principal Research Scientist

Acknowledgements

This thesis would not be possible without the help of many people. First and foremost, I want to thank my advisor, Dr. Chiping Chen, for his guidance and help with my research. I have learned a great deal about beam and nonneutral plasma physics from him. He also taught me how to write papers, how to organize and present my thoughts clearly, and how to make steady progress in research. I would like to thank my thesis reader, Professor Freidberg for reading my thesis and for asking thought-provoking and challenging questions — it helped to improve my thesis substantially. Thanks go to my thesis committee members, Professor Ian Hutchinson and Professor Ronald Parker. I would like to thank Dr. Santiago Bernal for providing the experimental data from the University of Maryland Electron Ring experiment, and for patiently answering my questions.

This thesis would have been impossible without my colleague, officemate, and friend Dr. Jing Zhou who helped me considerably with the theory, proofread my thesis, and was always there to discuss my research and answer my questions about various aspects of beam and accelerator physics. Special thanks go to Dr. Richard Temkin for his support over the years that I have been in his group. I would like to thank all past and present members of the Waves and Beam Division of PSFC. In particular, thank you to Dr. Michael Shapiro for watching over me, supporting me, and answering all the questions I came to him with; to Dr. Jagadishwar Sirigiri for his help with HFSS and my misbehaving computers; to Dr. Mark Hess, Dr. Amit Kesar, Dr. Ronak Bhatt, and Roark Marsh for helpful discussions and for the fun we had at various conferences over the years; to Dr. Eunmi Choi for providing a great support, for cooking me tasty Korean food, for great conversations, and for making my first year away from home easier; to Dr. Evgenya Smirnova, for helping me with applications to graduate school, for helpful discussions, for her hospitality, and for all the great times we had together.

Thanks go to my first research supervisor Dr. Vladimir Bratman for introducing me to the beauty of electrodynamics and for being a great teacher a student can only wish for. Thanks go to all my Professors at Advanced School of General and Applied Physics and at MIT; special thank you to Professors Grigorij Gislin and George Kocur, I learned a lot from you. I am grateful to the administrative assistants in the Nuclear Science and Engineering department, Heather Geddry and Clare Egan, for being there when I needed help.

I would like to thank the wonderful friends I met while in Boston and at MIT. Special thank you to Luisa Chiesa—without whom I would never have gotten through this—for listening, for great dinners, for supporting and encouraging me, for being patient, for listening and commenting on all my presentations, grazie, amica. Thank you to Antonio Damato for all the coffees we had when I needed a break, and for your sense of humor that always makes talking to you a great delight. Thank you to my friends Gretchen DeVries, Darwin James, Chudi Ndubaku, Corey Reed, Sejal Patel, Paolo Ferroni, Humberto Pereira, Cristina Thomas, Amanda Giermann, Oliver Dial, Miranda McGill, Matteo Chiesa, Ishani Kulatilaka, Myfanwy Callahan, Carolyn Jones, Danielle Reese, Jennifer Ellsworth, and Ken Marr. Special thanks go to Maya Hanelin, for listening and helping me to get through difficult times. I would like to thank the roommates I have had

at Adrian street over the years, especially Luisa Chiesa, Jen Winsor, Keshini Samerawickreme, Jesse Lonergan, and Matt Lambert, for great conversations and support.

Thank you to Ira Slabina for writing me every day for the past five years, you never doubted me; to Masha Ilina for being there for me when I needed you the most; to Ira Rypina and Ilya Udovydchenkov, for the conversations and laughs and fun I had visiting you in sunny Florida. Thank you to Ira Didenkulova for being a great friend—no distance could keep us apart. Thank you to Ilya Bandurkin, for answering my obscure questions and for your sense of humor. Thank you to Misha and Grisha Kagan, Natasha Sutin, and Jenya Kamenetskiy. A special thank you to Erik Nygren for his love, support, and patience, for helping me to get through with this work, for proofreading my thesis, and for being simply wonderful.

I would not have been able to do this without my family. Thanks go to my sister Anna for teaching me how to make things with my own hands. Thank you to my wonderful nieces Masha and Dasha, you are my pride and my joy. Lastly, and most importantly, I wish to thank my parents, Roman Vasil'evich Samokhvalov and Maria Alexeevna Gorshkova. Without you, this work would not have been possible. Thank you for your love and encouragement, thank you for always believing in me and for supporting me no matter what. I dedicate this thesis to you.

To my beloved parents,

Roman Vasil'evich Samokhvalov and Maria Alexeevna Gorshkova

Contents

1 Introduction

1.1 Applications of Charged-Particle Beams

High-brightness charged-particle beams are used in many areas of scientific research, as well as for a variety of applications. To mention a few examples, high-intensity charged-particle beams are used in high-energy colliders [1, 2], particle accelerators [3], spallation neutron sources [4], photoinjectors [5], x-ray sources [6], high-power microwave sources [7], vacuum electron devices [8], and material processing such as ion implantation [9].

High-energy colliders help scientists answer questions about matter and the Universe. For example, results from the Large Hadron Collider (LHC) [2], which is scheduled to begin operation in March of 2008, will advance knowledge about dark energy, dark matter, extra dimensions, Higgs phenomenon, and supersymmetry. In the LHC, whose beam tunnel has a circumference of 26.659 km, proton beams will collide at 14 TeV. Results from the LHC will be complemented by results from the International Linear Collider (ILC) [1], which is currently being designed. With the data from the ILC, scientists hope to determine the mass, spin, and interactions strengths of the Higgs boson, and to investigate TeV-scale extra dimensions and the lightest supersymmetric particles, which are possible candidates for dark matter. In the ILC, high-intensity electron and positron beams, produced by two linear accelerators, 12 km long each, will collide at 500 GeV.

The Spallation Neutron Source (SNS) [10], which is currently the most powerful neutron source in the world, provides a unique tool for neutron scattering research.

In the SNS, an H^- beam is accelerated to 1 GeV. The H^- beam is then transported to an accumulator ring, where it is both converted to protons by stripping away the electrons and bunched into a less than 10^{-6} sec pulse. Finally, the pulsed proton beam is directed onto a liquid mercury target to create neutrons through the spallation reactions of protons with the mercury nuclei. The purpose of the SNS is to study fundamental neutron physics and the structural and dynamic behavior of materials.

Not all accelerators that utilize high-intensity charged-particle beams are as large as the LHC, the ILC, or the SNS. The University of Maryland Electron Ring (UMER) [11], whose circumference is only 11.52 m, uses a scaled low-energy electron beam to access the high-brightness regime of beam operation in accelerators, at a much lower cost than larger and more energetic machines. UMER therefore makes an ideal testbed for experimenting on pushing up the brightness of existing and future accelerators [12—15].

For high-energy density physics (HEDP) and heavy ion fusion (HIF) research, high-brightness ion beams are being studied in the Virtual National Laboratory for Heavy-Ion Fusion [16]. These experiments include a high-brightness ion beam injector experiment to study the generation of ion beams with high current density and low emittance, the High-Current Experiment (HCX) [17] to investigate beam transport, acceleration and steering, the Neutralized Transport Experiment (NTX) [18] to model aspects of beam transport in a fusion chamber, and the Neutralized Drift Compression Experiment (NDCX) [19] to study beam compression for HEDP research. In HIF, high-brightness ion beams will have an energy of 3-10 GeV, a focal spot radius of 3 mm, and a total current of 40 kA on target. They will be used to heat a small (~1 cm) inertial fusion target for about 10^{-8} sec, which will then emit intense X-rays that compress the fuel capsule to

thousands of times its initial density and heat it, near the center, to thermonuclear temperatures. The resulting fusion reaction, which occurs in less than 10^{-9} sec, should produce about 100 times more energy than is supplied by the beams.

High-brightness electron beams are also used for generation of high-power electromagnetic waves in high-power microwave (HPM) sources such as klystrons, in vacuum electron devices, as well as in free electron lasers.

1.2 Charged-Particle Sources

Discussions of the dynamics of the charged-particle beam would be incomplete without discussions about particle sources, since they impose practical and fundamental limits for the beam current and emittance (i.e., the overall beam brightness and performance).

For electron beams, the source is usually a diode or a radiofrequency (rf) gun, where electrons are emitted from a conducting plate called the cathode. In an electron diode, electrons are then accelerated across the potential difference between the cathode and the other electrode, called the anode. The anode has a hole or a mesh to allow the beam to propagate into the beam tunnel downstream. The cathode can be either heated (thermal emission) or cold (field emission). It can also produce electrons by photoemission. In an rf gun, the cathode is located inside the first cavity of an rf injector-linac structure. After electrons are emitted from the cathode, they are accelerated to high energy by the strong axial electric field in the cavity.

For ion beams, positive or negative ions are typically extracted from either a plasma of a gas discharge or a fixed ion source. Then, they are accelerated in a vacuum drift tube and exit through a hole in the extraction electrode.

There is always a spread in the kinetic energy and velocity distributions of the particles in the beam. This intrinsic velocity spread remains present in the beam as it propagates through the beam tunnel. The beam quality can be described by the beam emittance, which is proportional to the product of beam's width and beam divergence. The most widely used beam emittance is the normalized root-mean-square (rms) emittance defined in one direction (say, the $x-$direction) as

$$\varepsilon_{xn} = \gamma_b \beta_b \varepsilon_{xrms}, \qquad (1.2.1)$$

where ε_{xrms} is the unnormalized rms emittance in the $x-$direction, defined as

$$\varepsilon_{xrms} = \left(\left\langle x^2 \right\rangle_\Gamma \left\langle x'^2 \right\rangle_\Gamma - \left\langle xx' \right\rangle_\Gamma^2 \right)^{1/2}, \qquad (1.2.2)$$

with the statistical average of χ over the phase space defined by $\left\langle \chi \right\rangle_\Gamma = N_b^{-1} \int \chi \, f_b dx dy dp_x dp_y$.

However, the beam emittance by itself is not sufficient to characterize the beam quality. A comprehensive measure of beam quality is the normalized 6D brightness

$$B_{6D} = \frac{N}{\varepsilon_{xn} \varepsilon_{yn} \sigma_\gamma \sigma_z}, \qquad (1.2.3)$$

where N is the number of particles in a bunch, ε_{xn} and ε_{yn} are the transverse normalized rms emittances, σ_z is the rms bunch length, and σ_γ is the rms energy spread.

In the case of a long beam, a 4D projection of the 6D brightness defined in Eq. (1.2.3) is commonly used, i.e.,

$$B_{4D} = \frac{I}{\varepsilon_{xn} \varepsilon_{yn}}, \qquad (1.2.4)$$

where I is the beam current. We will specialize to the case of two-dimensional continuous dc beams in the remainder of the thesis.

1.3 Space-Charge-Dominated Beams

An extreme regime of high-brightness charged-particle beams is the space-charge-dominated regime. When the beam brightness increases sufficiently, the beam becomes space-charge dominated. In the space-charge-dominated regime, the space-charge force is much greater than the thermal pressure force, which can be described by condition

$$K >> \frac{8\varepsilon_{xrms}^2}{r_{brms}^2}, \qquad (1.3.1)$$

where

$$K \equiv \frac{2N_b q^2}{\gamma_b^3 m \beta_b^2 c^2} \qquad (1.3.2)$$

is the self-field perveance of the beam and $r_{brms} = \sqrt{\langle r^2 \rangle_\Gamma} = \sqrt{\langle x^2 \rangle_\Gamma + \langle y^2 \rangle_\Gamma}$ is the rms radius of the beam.

The beam equilibrium in the space-charge-dominated regime is characterized by a beam core with a transversely uniform density distribution and a sharp edge where the beam density falls rapidly to zero in a few Debye lengths. For particle accelerators, high-brightness, space-charge-dominated charged-particle beams provide high beam intensities. For medical accelerators and x-ray sources, they provide higher and more precise radiation dosage. For ion implantation, they improve deposition uniformity and speed. For vacuum electron devices, they permit high-efficiency, low-noise operation with depressed collectors.

Table 1.1 illustrates that many applications discussed in Sec. 1.1 operate in the space-charge dominated regime.

Table 1.1 Examples of space-charge-dominated beams.

Device	Particle	Beam energy (MeV)	Current (mA)	Unnormalized rms emittance, ε_{xrms} (μm)	Rms beam radius (mm)	$\frac{Kr_{brms}^2}{8\varepsilon_{xrms}^2}$
UMER [20]	e^-	0.01	0.5-0.7	1.38	1.3-1.4	0.42-0.68
			5.8	4	2.9	2.85
			23	5	5.0	21.55
			100	15	10.3	44.13
HCX [17]	K^+	1	180	1.69	5.15	8.48
Fermilab A0-photoinjector [5]	e^-	14-18	$2.76 \cdot 10^5$	0.38	2.12	4.17-5.32

1.4 Periodic Focusing

The simplest way to focus a charged-particle beam is to apply a uniform magnetic focusing field. However, in many practical applications, the beams are focused by a periodic focusing field rather than a uniform magnetic focusing field [21] due to the limitations on the size of the magnets. Indeed, important applications of periodic focusing are in vacuum electron devices such as traveling-wave tubes, high-current beam transport over large distances, linear accelerators, sector-focusing cyclotrons, synchrotrons and rings, and other devices for recirculating electron beams.

One of the simplest cases of periodic focusing is a beam transport system with a periodic configuration of identical short solenoids. Figure 1.1 shows schematics of the solenoidal focusing lattices producing periodic solenoidal magnetic focusing fields with axial periodicity length S. In Fig. 1-1(a) the solenoidal field is produced by set of coils with the same polarity, spaced with a distance of S, resulting in the magnetic field on axis which oscillates about a non-zero average value. By contrast, in Fig. 1-1(b) the solenoidal field is produced by set of coils with alternating polarity, spaced with a distance of $S/2$. The configuration of coils in Fig. 1-1(b) results in the magnetic field on axis which oscillates about a zero average value. An advantage of the solenoidal focusing is its axisymmetry. However, the focusing strength of the axially symmetric solenoidal focusing field is relatively weak. Periodic solenoidal focusing is often referred to as weak focusing.

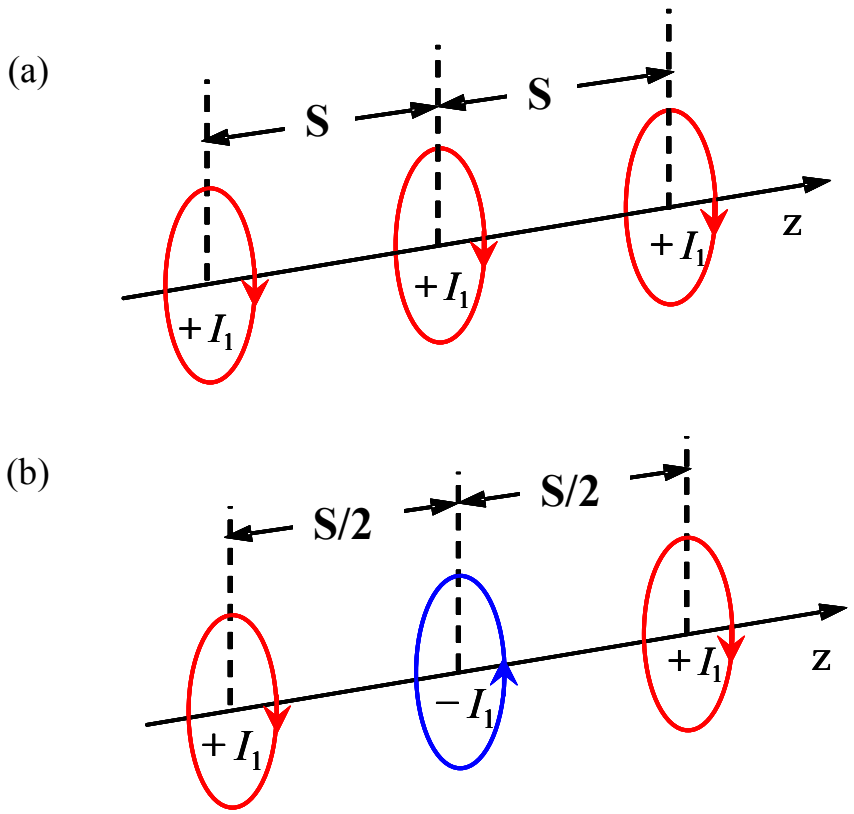

Fig. 1-1 Schematics of the coil sets producing solenoidal magnetic focusing fields with periodicity length S. The successive coils have (a) the same polarity and (b) alternating polarity.

An alternative to using a periodic solenoidal magnetic field for focusing is to use an array of quadrupole magnets. In Fig. 1-2, a set of magnets producing an alternating-gradient quadrupole magnetic focusing field with axial periodicity length S is shown. The magnet sets in Fig. 1-2 are rotated every half-period of the lattice by 90^0. Even though quadrupole magnetic focusing field does not have the azimuthal symmetry of a periodic solenoidal magnetic focusing field, magnetic quadrupole lenses are widely used, for instance, in high-energy accelerators, since they provide stronger focusing than magnetic solenoidal lenses at high particle kinetic energies. The alternating-gradient quadrupole magnetic focusing is often referred to as strong focusing.

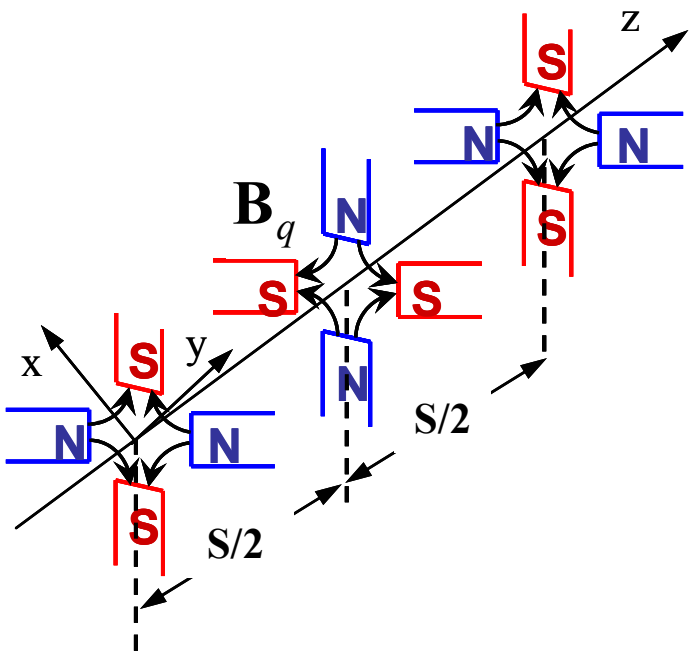

Fig. 1-2 Schematic of the magnet set producing an alternating-gradient quadrupole magnetic focusing field with periodicity length S.

1.5 Theoretical and Numerical Models for Charged-Particle Beams

Since charged-particle beams consist of one kind of charged particles, they are an example of nonneutral plasmas [22]. In nonneutral plasmas, where there is no overall charge neutrality, the space-charge forces play an important role. A variety of theoretical and numerical methods can be employed to describe collective and discrete particle effects in charged-particle beams. The statistical models used to describe collective effects are based either on fluid model, which solves fluid-Maxwell equations, or kinetic model, which solves Vlasov-Maxwell equations; whereas the discrete particle effects can be described with Klimontovich-Maxwell equations (see Chapter 2 in Ref. [22] and references therein).

In most practical beams, collision time is much greater than the time that particles spend in the systems, making collisions a relatively small effect [21]. The notable exceptions are the Boersch effect [23, 24] at low energies and intrabeam scattering [25—27] in the high-energy synchrotrons and storage rings. In this thesis we consider collisions to be unimportant.

Particle-in-cell (PIC) simulations have become a powerful tool for studying effects in non-neutral plasmas. PIC simulations follow the motion of a large assembly of charged particles in their self-consistent electric and magnetic fields. It has been shown [28—30] that when appropriate methods are used, even a small system of a few thousand particles is sufficient to adequately describe the collective effects in a real plasma. To perform such numerical simulation, considerable computer power is often required.

1.6 Why Beam Equilibria are Important

A fundamental understanding of the equilibrium and stability properties of high-intensity electron and ion beams in periodic focusing fields is important in high energy density physics research, in the design and operation of particle accelerators, such as storage rings, rf and induction linacs, and high-energy colliders, as well as in the design and operation of vacuum electron devices, such as klystrons and traveling-wave tubes with periodic permanent magnet (PPM) focusing. For such systems, beams of high quality (i.e., low emittance, high current, small energy spread, and low beam loss) are required. Exploration of equilibrium states of charged-particle beams and their stability properties is critical to the advancement of basic particle accelerator physics.

Of particular concern are emittance growth and beam losses which are related to the evolution of charged-particle beams in their non-equilibrium states. To minimize

emittance growth and control beam losses, it is critical to find equilibrium distributions of high-brightness charged-particle beams in accelerators and beam transport systems.

1.7 Previously Known Beam Equilibria

Several kinetic equilibria have been discovered for periodically focused intense charged-particle beams. Well-known equilibria for periodically focused intense beams include the Kapchinskij-Vladmirskij (KV) equilibrium [22, 31, 32] in an alternating-gradient quadrupole magnetic focusing field and the periodically focused rigid-rotor Vlasov equilibrium [33] in a periodic solenoidal magnetic focusing field. Both beam equilibria [22, 31—33] have a singular (δ – function) distribution in the four-dimensional phase space. Such a δ – function distribution gives a uniform density profile across the beam in the transverse directions, and a transverse temperature profile which peaks on axis and decreases quadratically to zero on the edge of the beam. Because of the singularity in the distribution functions, both equilibria are not likely to occur in real physical systems and cannot provide realistic models for theoretical and experimental studies and simulations except for the zero-temperature limit. For example, the KV equilibrium model cannot be used to explain the beam tails in the radial distributions observed in recent high-intensity beam experiments [34].

In general, a beam is generated by a gun which has a uniformly heated emitting surface. The resulting beam is in the thermal equilibrium with the uniform temperature across the transverse beam's cross-section (see discussion in Appendix A). A theoretical understanding of thermal equilibrium and stable transport is desirable. Kinetic and warm-fluid theories of a thermal equilibrium in a uniform magnetic focusing field have been studied in Ref. [22]. A formal multiple scale analysis (a third-order averaging technique)

has been applied to obtain an approximate periodically focused thermal equilibrium in periodic solenoidal and periodic quadrupole magnetic fields [35]. Such an averaging procedure is expected to be valid for sufficiently small vacuum phase advances, whereas typical accelerators operate in the regime with moderate vacuum phase advances.

1.8 Thesis Outline

The primary purpose of this thesis is to establish thermal equilibrium theory of periodically focused charged-particle beams. In particular, thermal beam equilibria are discussed for paraxial beams in periodic solenoidal and quadrupole magnetic focusing fields, the two magnetic focusing field configurations most commonly used in accelerators.

In Chapter 2, a warm-fluid equilibrium theory for a thermal beam in a periodic solenoidal focusing field is presented. Solving the warm-fluid equations in the paraxial approximation, the beam density and flow velocity are obtained. The self-consistent rms beam envelope equation and the self-consistent Poisson equation, governing the beam density and potential distributions, are derived. The equation of state for the beam is adiabatic, i.e., there is no heat flow in the system, which results in rms beam emittance being conserved. The beam temperature is constant across the cross-section of the beam. For high-intensity beams, the beam density profile is shown to be flat in the center of the beam. It falls off rapidly within a few Debye lengths at the edge of the beam. Such a density profile provides a more realistic representation of the beam than the uniform density profile in previous theories (see, for example, Ref. [31, 33, and 36]).

In Chapter 3, a kinetic equilibrium theory for a thermal beam in a periodic solenoidal focusing field is presented. The kinetic theory, while being equivalent to the warm-fluid

theory discussed in Chapter 2, provides more information about the thermal beam equilibrium, especially, the detailed equilibrium distribution function in the particle phase space. The Hamiltonian for single particle motion is analyzed to find the approximate and exact invariants of motion, i.e., a scaled transverse Hamiltonian (nonlinear space charge included) and the angular momentum, from which the beam equilibrium distribution is constructed. The approximation of the scaled transverse Hamiltonian as an invariant of motion is validated analytically for highly emittance-dominated beams and highly space-charge-dominated beams, and is numerically tested to be valid for cases in between with moderate vacuum phase advances ($\sigma_v < 90°$). The beam envelope and emittances are then determined self-consistently with the beam equilibrium distribution.

In Chapter 4, a warm-fluid equilibrium theory for a thermal beam in periodic quadrupole magnetic focusing field is presented. In the periodic quadrupole magnetic focusing field, the cross section of the beam is in general elliptical. An adiabatic process is considered. The warm-fluid equilibrium theory for the thermal beam in a periodic solenoidal magnetic focusing field (presented in Chapter 2) is generalized to the case of the thermal beam in a periodic quadrupole magnetic focusing field. The rms beam envelope equations and the self-consistent Poisson equation, governing the beam density and potential distributions, are derived. It is shown that the equilibrium equipotential contours and constant density contours are ellipses. Because the thermal equilibrium is adiabatic, the 4D thermal rms emittance of the beam is conserved. The equilibrium density profile has the same basic property as the equilibrium density profile for the thermal beam in a periodic solenoidal focusing field; that is, for the high-intensity beams the beam density profile is flat in the center of the beam and then falls off rapidly within a

few Debye lengths at the edge of the beam. An interesting property of the equilibrium is that the rate at which the density falls is transversely isotropic.

In Chapter 5, quantitative comparisons are made between the equilibrium theories presented in Chapters 2-4 and results of recent experiments at the University of Maryland Electron Ring [34, 37]. In the case of the periodic solenoidal focusing experiment, good agreement is found between our theory and the experimental measurements from the anode aperture to a distance prior to wave breaking. In the case of the AG focusing experiment, reasonably good agreement is also found between theoretical and experimentally measured density profiles in one transverse direction along which the beam is close to equilibrium.

2 Warm-Fluid Equilibrium Theory of Thermal Charged-Particle Beams in Periodic Solenoidal Focusing Fields

2.1 Introduction

As mentioned in Chapter 1, it is important to gain a fundamental understanding of the thermal equilibrium of charged-particle beams in periodic focusing fields. Periodic solenoidal focusing fields are widely used for beam focusing in many experiments and applications. Even though a periodic solenoidal focusing field provides weaker focusing than a periodic quadrupole magnetic focusing field, it is attractive because it keeps the beam axisymmetric, thereby yielding a higher degree of symmetry than a periodic quadrupole magnetic focusing field.

Several equilibria have been discovered for intense charged-particle beams in periodic focusing solenoidal fields. A Vlasov beam equilibrium has been found for the periodically focused rigid rotor in a periodic solenoidal magnetic focusing field [33, 38]. However, the Vlasov beam equilibrium uses a $\delta-$function phase-space distribution, which is unphysical. A cold-fluid beam equilibrium has also been found for an intense beam propagating in a periodic focusing solenoidal field [36], but it does not take into account beam temperature effects. In addition, a formal multiple scale analysis (i.e., a third-order averaging technique) has been applied to obtain approximate Vlasov and thermal equilibria in periodic solenoidal focusing fields [35]. Such an averaging procedure is valid for sufficiently small vacuum phase advances, whereas typical accelerators operate in the regime with moderate vacuum phase advances.

We describe collective effects in charged-particle beams by adopting warm-fluid theory and solving fluid-Maxwell equations. A warm-fluid theory, which is less difficult for one to develop than a kinetic theory, provides good insight into the beam equilibrium, the rms beam envelope, the beam temperature, the beam fluid velocity, and the beam density. It is readily shown that for the thermal rigid-rotor beam equilibrium in a uniform focusing field, the kinetic and warm-fluid theories are equivalent, i.e., they both predict the same rms beam envelope, beam temperature, beam fluid velocity, and beam density. In Chapter 3, we will develop a kinetic theory for a thermal equilibrium beam in a periodic solenoidal magnetic focusing field which is equivalent to the warm-fluid theory presented in this chapter.

Our warm-fluid model requires assumptions about the equation of state and the heat flux in the system to provide a closure for the fluid equations. In the present analysis, we impose zero heat flux and consider the beam equilibrium to be adiabatic.

In this chapter, we present a paraxial warm-fluid equilibrium theory for a thermal charged-particle beam in a periodic solenoidal focusing field [39, 40]. The transverse rms emittance of the beam is conserved, and the beam temperature is constant across the cross-section of the beam but varies with the propagating distance. For high-intensity beams, the beam density profile is shown to be flat in the center of the beam. It falls off rapidly within a few Debye lengths at the edge of the beam.

This chapter is organized as follows. In Sec. 2.2, the basic assumptions in the present warm-fluid model are presented. Warm-fluid equilibrium equations are used to derive expressions for the flow velocity profile and beam density distribution, an rms beam envelope equation, and a self-consistent Poisson equation. In Sec. 2.3, a numerical

technique for computing thermal beam equilibria is discussed. Several examples of thermal beam equilibria are presented. The radial confinement of the beam is discussed. In Sec. 2.4, a summary is presented.

2.2 Warm-Fluid Beam Equilibrium Equations

We consider a thin, continuous, axisymmetric ($\partial/\partial\theta = 0$), single-species charged-particle beam, propagating with constant axial velocity $V_z\hat{\mathbf{e}}_z$ through an applied periodic solenoidal magnetic focusing field. The applied periodic solenoidal focusing field inside the beam can be approximated by [39, 40]

$$\mathbf{B}^{ext}(r,s) = -\frac{1}{2}B_z'(s)r\,\hat{\mathbf{e}}_r + B_z(s)\hat{\mathbf{e}}_z\,, \qquad (2.2.1)$$

where $s = z$ is the axial coordinate, $r = \sqrt{x^2 + y^2}$ is the radial distance from the beam axis, prime denotes the derivative with respect to s, and $B_z(s) = B_z(s+S)$ is the axial magnetic field, which is periodic along the z-axis with periodicity length S.

In the paraxial approximation, $r_{brms} << S$ is assumed, where r_{brms} is the rms beam envelope. The transverse kinetic energy of the beam is assumed to be small compared with its axial kinetic energy, i.e., $|V_z| >> |V_\perp|$. In the paraxial approximation, we assume $\nu/\gamma_b^3\beta_b^2 << 1$, where $\nu \equiv q^2 N_b/mc^2$ is the Budker parameter [22] of the beam, q and m are the particle charge and rest mass, respectively, c is the speed of light in vacuum, $N_b = 2\pi\int_0^\infty dr\, r\, n_b(r,s)$ is the number of particles per unit axial length, and γ_b is the relativistic mass factor, which, to leading order, is $\gamma_b = const = (1-\beta_b^2)^{-1/2}$ with $\beta_b = V_b/c \cong V_z/c$.

It is convenient to express the self-electric and self-magnetic fields, produced by the space charge and axial current of the beam, in terms of the scalar and vector potentials, i.e.,

$$\mathbf{E}^{self}(r,s) = -\nabla\phi^{self}(r,s) \tag{2.2.2}$$

and

$$\mathbf{B}^{self}(r,s) = \nabla\times\mathbf{A}^{self}(r,s). \tag{2.2.3}$$

In the paraxial approximation, the self-field potentials ϕ^{self} and $\mathbf{A}^{self}$ are related by the familiar expression (see, for example, Ref. [22] and Appendix A)

$$\mathbf{A}^{self} = A_z^{self}\hat{\mathbf{e}}_z = \beta_b\phi^{self}(r,s)\hat{\mathbf{e}}_z. \tag{2.2.4}$$

Consequently, the self-magnetic field is

$$B_\theta^{self}\hat{\mathbf{e}}_\theta = -\beta_b\frac{\partial\phi^{self}}{\partial r}\hat{\mathbf{e}}_\theta. \tag{2.2.5}$$

In the paraxial approximation, the warm-fluid beam equilibrium ($\partial/\partial t = 0$) equations are [22, 39, 40]

$$n_b\,\mathbf{V}\cdot\nabla(\gamma_b m\mathbf{V}) = n_b q\left[-\nabla\phi^{self} + \frac{\mathbf{V}}{c}\times\left(\mathbf{B}^{ext}+\mathbf{B}^{self}\right)\right] - \nabla\cdot\vec{\mathbf{P}}(\mathbf{x}), \tag{2.2.6}$$

$$\nabla\cdot(n_b\mathbf{V}) = 0, \tag{2.2.7}$$

$$\nabla^2\phi^{self}(r,s) = -4\pi q\,n_b(r,s), \tag{2.2.8}$$

$$p_\perp(r,s) = n_b(r,s)k_B T_\perp(s), \tag{2.2.9}$$

$$T_\perp(s)r_{brms}^2(s) = const. \tag{2.2.10}$$

In Eqs. (2.2.6)-(2.2.10), $\vec{\mathbf{P}}(r,s) = p_\perp(r,s)(\hat{\mathbf{e}}_r\hat{\mathbf{e}}_r + \hat{\mathbf{e}}_\theta\hat{\mathbf{e}}_\theta) + p_{||}(r,s)\hat{\mathbf{e}}_z\hat{\mathbf{e}}_z$ is the pressure tensor, $p_\perp(r,s)$ and $p_{||}(r,s)$ are transverse and parallel thermal pressures, respectively,

$T_\perp(s)$ is the transverse beam temperature which remains constant across the transverse cross-section of the beam, and $r_{brms}(s)$ is the root-mean-square (rms) radius of the beam defined by

$$r_{brms}^2(s) = N_b^{-1}\, 2\pi \int_0^\infty dr\, r^3\, n_b(r,s). \qquad (2.2.11)$$

As shown in Appendix A, for the equilibrium in the present analysis, Eq. (2.2.10) states that the beam motion is adiabatic. Note that for the axisymmetric beam in the paraxial approximation, we can approximate $\nabla^2 \cong \frac{1}{r}\frac{\partial}{\partial r} r \frac{\partial}{\partial r}$ to leading order in the Poisson equation (2.2.8). In the present paraxial analysis, we do not consider the axial component of the momentum equation (2.2.6) (see Appendix A for more discussion).

We seek a solution for the equilibrium velocity profile of the form

$$V_r(r,s) = r\frac{r'_{brms}(s)}{r_{brms}(s)}\beta_b c\,, \qquad (2.2.12)$$

$$V_\theta(r,s) = r\,\Omega_b(s), \qquad (2.2.13)$$

which corresponds to a beam undergoing rotation with the angular frequency $\Omega_b(s)$ to be determined self-consistently later [see Eq.(2.2.28)].

The radial component of the momentum equation (2.2.6) can be rewritten as

$$\frac{\partial}{\partial r}\ln[n_b(r,s)] \qquad (2.2.14)$$
$$= -\frac{\gamma_b m}{k_B T_\perp(s)} r\left\{\beta_b^2 c^2 \frac{r''_{brms}(s)}{r_{brms}(s)} - \Omega_b(s)\cdot[\Omega_b(s)+\Omega_c(s)]\right\} - \frac{q}{\gamma_b^2 k_B T_\perp(s)}\frac{\partial \phi^{self}(r,s)}{\partial r},$$

where use has been made of Eqs. (2.2.9), (2.2.12), and (2.2.13) and $\Omega_c(s) = qB_z(s)/mc\gamma_b$ is the relativistic cyclotron frequency. Equation (2.2.14) can be integrated to give the density profile

$$n_b(r,s) \qquad (2.2.15)$$
$$= f(s)\exp\left(-\frac{\gamma_b m\beta_b^2 c^2 r^2}{2k_B T_\perp(s)}\left\{\frac{r''_{brms}(s)}{r_{brms}(s)} - \frac{\Omega_b(s)\cdot[\Omega_b(s)+\Omega_c(s)]}{\beta_b^2 c^2}\right\} - \frac{q\phi^{self}(r,s)}{\gamma_b^2 k_B T_\perp(s)}\right),$$

where $f(s)$ is an arbitrary function of s to be determined later [see Eq. (2.2.26)]. The density in the center of the beam, i.e., the peak density, is

$$n_b^{peak}(s) \equiv n_b(0,s) = f(s)\exp\left[-q\phi^{self}(0,s)/\gamma_b^2 k_B T_\perp(s)\right]. \qquad (2.2.16)$$

Using the density profile given in Eq. (2.2.15), we obtain a useful expression for the rms beam radius, i.e.,

$$r_{brms}^2(s) = 2\left[\frac{k_B T_\perp(s)}{\gamma_b m\beta_b^2 c^2} + \frac{q^2 N_b}{2\gamma_b^3 m\beta_b^2 c^2}\right]\left\{\frac{r''_{brms}(s)}{r_{brms}(s)} - \frac{\Omega_b(s)[\Omega_b(s)+\Omega_c(s)]}{\beta_b^2 c^2}\right\}^{-1}, \qquad (2.2.17)$$

where we have assumed that the beam density is infinitely small at $r = \infty$.

Since $k_B T_\perp(s) = \frac{m\gamma_b}{2}\left\langle(\mathbf{v}_\perp - \mathbf{V}_\perp)^2\right\rangle_\Gamma = m\gamma_b\left\langle(v_x - V_x)^2\right\rangle_\Gamma$, $\left\langle x^2\right\rangle_\Gamma = r_{brms}^2(s)/2$, we can express the rms thermal emittance of the beam as

$$\varepsilon_{th}^2 = (\beta_b c)^{-2}\left\langle x^2\right\rangle_\Gamma\left\langle(v_x - V_x)^2\right\rangle_\Gamma = \frac{k_B T_\perp(s) r_{brms}^2(s)}{2m\gamma_b\beta_b^2 c^2}, \qquad (2.2.18)$$

where the statistical average of χ is defined in the usual manner by

$$\langle\chi\rangle_\Gamma = N_b^{-1}\int \chi\, f_b\, dxdydp_x dp_y \qquad (2.2.19)$$

with f_b being the particle distribution function corresponding to the warm-fluid beam equilibrium [41,42]. Combining Eqs. (2.2.17) and (2.2.18) yields the following rms beam envelope equation

$$r''_{brms}(s)-\frac{\Omega_b(s)\left[\Omega_b(s)+\Omega_c(s)\right]}{\beta_b^2 c^2}r_{brms}(s)-\frac{K}{2r_{brms}(s)}=\frac{4\varepsilon_{th}^2}{r_{brms}^3(s)}, \qquad (2.2.20)$$

where

$$K\equiv\frac{2N_b q^2}{\gamma_b^3 m\beta_b^2 c^2} \qquad (2.2.21)$$

is the self-field perveance.

Substituting Eq. (2.2.20) into Eq. (2.2.15) we obtain the simplified expression for the equilibrium beam density

$$n_b(r,s)=f(s)\exp\left\{-\frac{r^2}{4\varepsilon_{th}^2}\left[\frac{K}{2}+\frac{4\varepsilon_{th}^2}{r_{brms}^2(s)}\right]-\frac{q\phi^{self}(r,s)}{\gamma_b^2 k_B T_\perp(s)}\right\}, \qquad (2.2.22)$$

where the scalar potential for the self-electric field satisfies the Poisson equation

$$\frac{1}{r}\frac{\partial}{\partial r}\left[r\frac{\partial}{\partial r}\phi^{self}(r,s)\right]=-4\pi q f(s)exp\left\{-\frac{r^2}{4\varepsilon_{th}^2}\left[\frac{K}{2}+\frac{4\varepsilon_{th}^2}{r_{brms}^2(s)}\right]-\frac{q\phi^{self}(r,s)}{\gamma_b^2 k_B T_\perp(s)}\right\}. \qquad (2.2.23)$$

Note that when $B_z(s)=const$, the beam density in Eq. (2.2.22) recovers the well-known thermal rigid-rotor equilibrium in a uniform magnetic field [22].

Density profile in the form of Eq. (2.2.22) and the velocity profiles (2.2.12) and (2.2.13) have to satisfy the continuity equation (2.2.7). Substituting Eqs. (2.2.12), (2.2.13), and (2.2.22) into Eq. (2.2.7), and integrating over the cross section of the beam yields

$$\left[2\frac{r'_{brms}(s)}{r_{brms}(s)}+\frac{1}{f(s)}\frac{df(s)}{ds}\right]-\frac{K}{4\varepsilon_{th}^2}\frac{d}{ds}\left[\frac{r_{brms}^2(s)}{2}+r_{brms}^2(s)\left\langle\frac{\phi^{self}(r,s)}{qN_b}\right\rangle\right]=0. \qquad (2.2.24)$$

Note that Eq. (2.2.24) is equivalent to the conservation of the total number of particles per unit axial length, i.e.,

$$\frac{dN_b}{ds}=0 \text{ or } N_b=const. \qquad (2.2.25)$$

Setting the sum of the first two terms in Eq. (2.2.24) to zero gives

$$f(s)\equiv\frac{C}{r_{brms}^2(s)}. \qquad (2.2.26)$$

where C is a constant of integration.

We solve the Poisson equation (2.2.23) to determine the electric self-field potential, with $f(s)$ satisfying Eq. (2.2.26), where the electric self-field potential on axis $\phi^{self}(r=0,s)$ is determined by setting the sum of the third and fourth terms in Eq. (2.2.24) to zero. A numerical scheme for determining $\phi^{self}(r=0,s)$ will be described in Sec. 2.3. The electric self-field potential energy on axis $q\phi^{self}(0,s)$ is very small compared with the beam transverse thermal energy, which will be demonstrated in Sec. 2.3.

To gain further insight into the azimuthal motion of the beam, we make use of Eqs. (2.2.12) and (2.2.13) to express the azimuthal component of the momentum equation (2.2.6) as

$$n_b(r,s)\left[r\frac{r'_{brms}(s)}{r_{brms}(s)}\beta_b c\frac{\partial}{\partial r}+\beta_b c\frac{\partial}{\partial s}\right]\left[\Omega_b(s)r^2+\frac{1}{2}\Omega_c(s)r^2\right]=0. \qquad (2.2.27)$$

Consistent with Eq. (2.2.13), we find the solution to Eq. (2.2.27) as

$$\Omega_b(s) = -\frac{1}{2}\Omega_c(s) + \frac{\omega_b r_{b0}^2}{r_{brms}^2(s)}, \qquad (2.2.28)$$

where ω_b and r_{b0} are constants. In Eq. (2.2.28), the term $\omega_b r_{b0}^2 / r_{brms}^2(s)$ represents the azimuthal beam rotation relative to the Larmor frame, which rotates at the frequency $-\Omega_c(s)/2$ relative to the laboratory frame.

Substituting Eq. (2.2.28) into Eq. (2.2.20), we obtain the following alternative form of the rms beam envelope equation:

$$r_{brms}''(s) + \left[\kappa_z(s) - \frac{\omega_b^2 r_{b0}^4}{r_{brms}^4(s)\beta_b^2 c^2}\right] r_{brms}(s) - \frac{K}{2r_{brms}(s)} = \frac{4\varepsilon_{th}^2}{r_{brms}^3(s)}, \qquad (2.2.29)$$

where

$$\sqrt{\kappa_z(s)} \equiv \frac{qB_z(s)}{2\gamma_b\beta_b mc^2} \qquad (2.2.30)$$

is the focusing parameter. In the limit $\varepsilon_{th} = 0$, Eq. (2.2.29) recovers the previous envelope equation for the cold-fluid beam equilibrium [36].

Note that the term proportional to $\omega_b^2 r_{b0}^4 / r_{brms}^3(s)$ in Eq. (2.2.29) plays the role of an effective emittance contribution to the envelope equation associated with the average azimuthal beam rotation relative to the Larmor frame. Also note that the rms beam envelope equation (2.2.29) agrees with the well-known rms envelope equation [43], with the interpretation of the total emittance

$$\varepsilon_T^2 = 16\varepsilon_{th}^2 + 4\frac{\omega_b^2 r_{b0}^4}{\beta_b^2 c^2}. \qquad (2.2.31)$$

In Appendix A, we present a more general derivation of this equilibrium and show that it is equivalent to the above derivation. In particular, we use Eq. (A.4.4) as an equation of state and radial velocity profile in the form of Eq. (A.3.1). We then demonstrate that

Eq. (A.4.4) can be written as Eq. (2.2.10) and Eq. (A.3.1) can be written as Eq. (2.2.12), making the two derivations equivalent.

2.3 Numerical Calculations of Warm-Fluid Beam Equilibria

In this section, we present a numerical technique for computing the warm-fluid beam equilibria. We calculate the beam density by solving the self-consistent Poisson equation and present several examples of warm-fluid beam equilibria. We show that thermal beam equilibria exist for a wide range of parameters and discuss the radial confinement of the beam.

To determine the warm-fluid beam equilibrium numerically, we obtain the matched rms beam envelope by solving the rms beam envelope equation (2.2.29) with the periodic boundary conditions [33], i.e.,

$$r_{brms}(s) = r_{brms}(s+S). \qquad (2.3.1)$$

We then use the matched rms beam envelope in the calculation of the beam density and potential at any given s from Eqs. (2.2.22) and (2.2.23).

We calculate the scalar potential for the self-electric field using the Poisson equation (2.2.23). We rewrite the Poisson equation (2.2.23) as

$$\begin{aligned} &\frac{1}{r}\frac{\partial}{\partial r}\left[r\frac{\partial}{\partial r}\Delta\phi(r,s)\right] \qquad (2.3.2)\\ = \quad &-\frac{4\pi q C}{r_{brms}^2(s)} exp\left[-\frac{q\,\phi^{self}(r=0,s)}{\gamma_b^2 k_B T_\perp(s)}\right] exp\left\{ -\frac{r^2}{4\varepsilon_{th}^2}\left[\frac{K}{2}+\frac{4\varepsilon_{th}^2}{r_{brms}^2(s)}\right] - \frac{q\,\Delta\phi(r,s)}{\gamma_b^2 k_B T_\perp(s)}\right\}, \end{aligned}$$

where $\Delta\phi(r,s) \equiv \phi^{self}(r,s) - \phi^{self}(r=0,s)$ and use has been made of Eq. (2.2.26). We solve Eq. (2.3.2) with the boundary conditions

$$\Delta\phi(0,s)=0 \text{ and } \left.\frac{\partial\Delta\phi(r,s)}{\partial r}\right|_{r=0}=0, \tag{2.3.3}$$

such that the resulting self-field potential correspond to the radially confined beam. We integrate Eq. (2.3.2) from $r=0$ to a few r_{brms}, paying special attention to the singularity at $r=0$. To avoid the singularity, we analytically integrate Eq. (2.3.2) with boundary conditions (2.3.3) near the z-axis from $r=0$ to $r=\Delta r$ (with $\Delta r << r_{brms}$), treating the beam density as a constant. Then, we approximate $\Delta\phi(r,s)$ by the scalar potential of the space-charge-dominated beam with $SK/\varepsilon_{th} >> 1$ as

$$\Delta\phi(r,s)\approx -\frac{qN_b}{2r_{brms}^2(s)}r^2, \text{ for } r\le\sqrt{2}r_{brms}. \tag{2.3.4}$$

Using this potential we numerically integrate Eq. (2.3.2) outwards from $r=\Delta r$.

For the purposes of numerical calculations, it is useful to rewrite Eq. (2.2.25) as

$$\begin{aligned}\Delta &\equiv 1-N_b^{-1}\int_0^\infty 2\pi\, n_b r dr \\ &= 1-\hat{C}(s)\exp\left[-\frac{q\,\phi^{self}(r=0,s)}{\gamma_b^2 k_B T_\perp(s)}\right]\int_0^\infty \exp\left\{-\frac{r^2}{4\varepsilon_{th}^2}\left[\frac{K}{2}+\frac{4\varepsilon_{th}^2}{r_{brms}^2(s)}\right]-\frac{q\,\Delta\phi(r,s)}{\gamma_b^2 k_B T_\perp(s)}\right\} r dr = 0,\end{aligned} \tag{2.3.5}$$

where $\hat{C}(s)=2\pi C N_b^{-1} r_{brms}^{-2}(s)$. In our numerical calculations, an iterative procedure is applied to solve Eq. (2.3.5), and Δ is less than 10^{-4}.

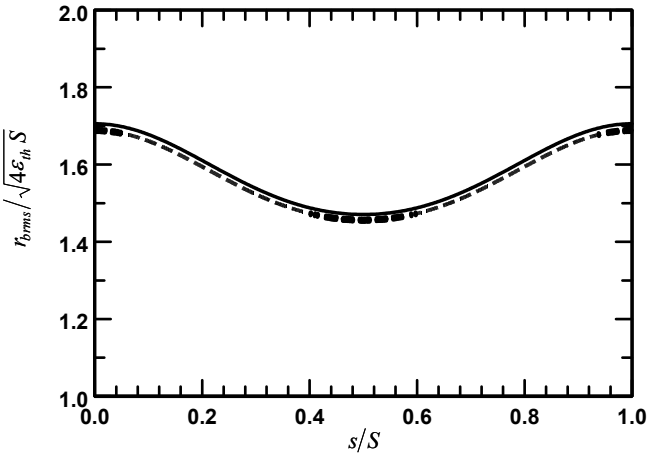

Fig. 2-1 Normalized beam envelope profiles for $S\sqrt{\kappa_z(s)} = a_0 + a_1\cos(2\pi s/S)$, $a_0 = a_1 = 1.14$, $\omega_b = 0$, a warm-fluid (solid curve) beam equilibrium with $\hat{K} = 10$, and a cold-fluid (dashed curve) beam equilibrium [40].

In Fig. 2-1, we show the rms envelope profiles for $S\sqrt{\kappa_z(s)} = a_0 + a_1\cos(2\pi s/S)$, $a_0 = a_1 = 1.14$, $\omega_b = 0$, a warm-fluid (solid curve) beam equilibrium with the "scaled" normalized perveance $\hat{K} \equiv KS/4\varepsilon_{th} = 10$, and a cold-fluid (dashed curve) beam equilibrium with $\hat{K} = \infty$. The rms beam radius $r_{brms}^{cold}(s)$ for the cold-fluid beam equilibrium is determined from Eq. (2.2.29) with the right-hand side equal to zero. In Fig. 2-1 the effects of the finite temperature enlarge the rms beam envelope by 1%.

In Fig. 2-2, we plot the on-axis electric self-field potential energy relative to the beam transverse thermal energy, $\dfrac{q\phi^{self}(0,s)}{\gamma_b^2 k_B T_\perp(s)}$, as a function of s/S for $\hat{K} = 0.1$, 1 and 10. The rest of the parameters are the same as in Fig. 2-1. The integration constant C is chosen such that $\phi^{self}(0,S/4) = 0$. The electric self-field potential on axis is indeed small.

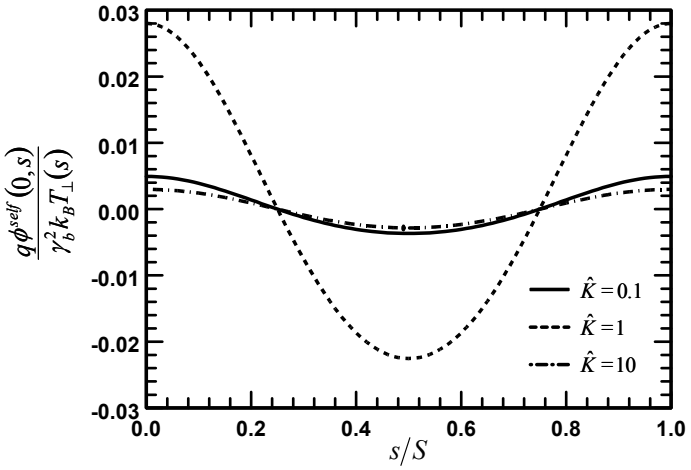

Fig. 2-2 Plot of the on-axis electric self-field potential energy relative to the beam transverse thermal energy as a function of s/S for $\hat{K} = 0.1$, 1, and 10. The other system parameters are the same as in Fig. 2-1 [40].

In Fig. 2-3, the density profiles are plotted for the warm-fluid (solid curve) and cold-fluid (dashed curve) beam equilibria corresponding to the examples shown in Fig. 2-1. The warm-fluid beam density is nearly uniform up to the beam edge where it falls rapidly within a few Debye lengths. Here, the Debye length is defined as

$$\lambda_D \equiv \sqrt{\frac{\gamma_b^2 k_B T_\perp(s)}{4\pi q^2 n_b(0,s)}}. \qquad (2.3.6)$$

For the warm-fluid beam equilibrium, $r_{brms} \approx 15.4\lambda_D$. The density of the cold [$T_\perp(s) \equiv 0$] beam is (see, for example, Ref. [36])

$$n_{cold}(r,s) = \frac{N_b}{2\pi r_{brms}^{cold}(s)^2}, \text{ for } r \le \sqrt{2} r_{brms}^{cold}(s). \qquad (2.3.7)$$

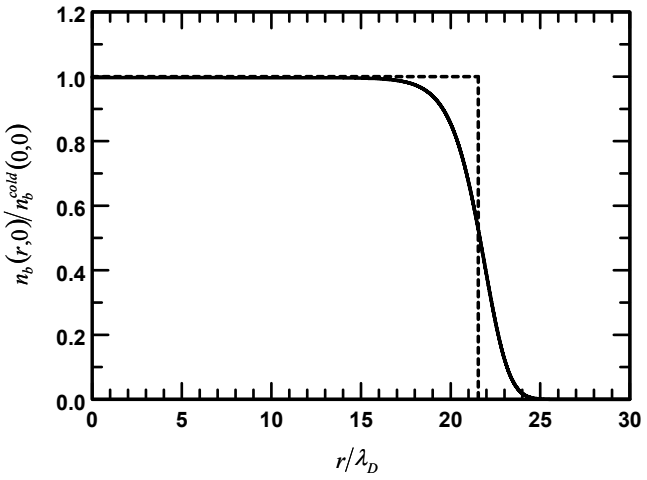

Fig. 2-3 Plot of the relative beam density vs. r/λ_D for a warm-fluid beam equilibrium (solid curve) and a cold-fluid beam equilibrium (dashed curve) at $s = 0$ for the same parameters as in Fig. 2-1. Here, $r_{brms} \approx 15.4\,\lambda_D$ for the warm-fluid beam equilibrium [40].

The effect of the beam temperature on beam density distribution is illustrated in Fig. 2-4. As we increase the beam temperature and keep other system parameters the same, $\hat{K}$ decreases, and the density profile makes the transition from a step-function profile (for $T_\perp = 0$) to a bell-shaped profile, as shown in Fig. 2-4.

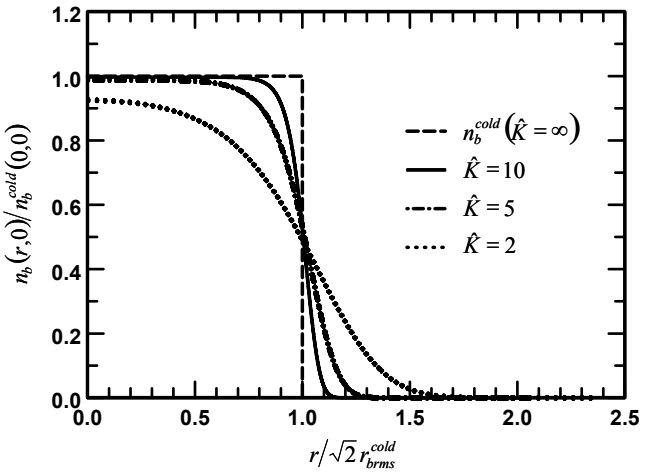

Fig. 2-4 Plot of the relative density profiles at $s=0$ at several temperatures: $\hat{K}=\infty$ (cold), 10, 5, and 2. The other system parameters are kept the same as in Fig. 2-1 [40].

There is a wide range of parameters for which the warm-fluid beam equilibrium exists in a periodic solenoidal focusing channel. For practical purposes, it is useful to determine the radial confinement in an average sense. In Fig. 2-5, we plot the normalized angular frequency of beam rotation in the Larmor frame, $\frac{S}{\sigma_v \beta_b c}\left\langle \Omega_b(s)+\frac{\Omega_c(s)}{2}\right\rangle$, as a function of the effective self-field parameter $\langle s_e\rangle \equiv \frac{S^2\langle \omega_{pb}^2(s)\rangle}{2\gamma_b^2\sigma_v^2\beta_b^2c^2}$ for $\hat{K}=0.1$, 0.2, 1, and 10. The beam propagates in a periodic solenoidal focusing field with $S\sqrt{\kappa_z(s)}=a_0+a_1\cos(2\pi s/S)$, where $a_0=a_1=1.14$. The beam current is kept the same while the rms thermal emittance ε_{th} of the beam decreases. Here, $\omega_{pb}(s)\equiv\left[4\pi q^2 n_b(0,s)/\gamma_b m\right]^{1/2}$ is the plasma frequency, $\sigma_v \equiv \int_0^S w_0^{-2}(s)ds$ is the vacuum

phase advance over one axial period S, the amplitude function $w_0(s)$ satisfies the following equation (see, for example, Ref. [21])

$$w_0''(s) + \kappa_z(s) w_0(s) = \frac{1}{w_0^3(s)}, \qquad (2.3.8)$$

and $\langle f(s) \rangle = S^{-1} \int_0^S f(s) ds$ denotes the average of the function $f(s)$ over one axial period of the system.

While Fig. 2-5 is computed for the specific periodic solenoidal focusing field with $S\sqrt{\kappa_z(s)} = a_0 + a_1 \cos(2\pi s/S)$, where $a_0 = a_1 = 1.14$, we observe no change in the Fig. 2-5 if we vary the values of a_0 and a_1, provided that the vacuum phase advance σ_v of the magnetic field does not change. For $a_1 = 0$, Fig. 2-5 recovers the thermal beam equilibrium in a uniform magnetic focusing field (see Ref. [22]).

As shown in Fig. 2-5, each curve at a particular value of $\hat{K}$ has two branches. For any value of the effective self-field parameter $\langle s_e \rangle$ below a critical value, a confined beam can rotate at two angular frequencies, either positive or negative relative to the Larmor frame. For each value of $\hat{K}$, the maximum (critical) value of the effective self-field parameter for a confined beam is reached when the beam does not rotate relative to the Larmor frame. In Fig. 2-6, the critical effective self-field parameter $\langle s_e \rangle$ is plotted as a function of $\hat{K} \equiv KS/4\varepsilon_{th}$. The parameter space for radial beam confinement is indicated by the shaded region in Fig. 2-6.

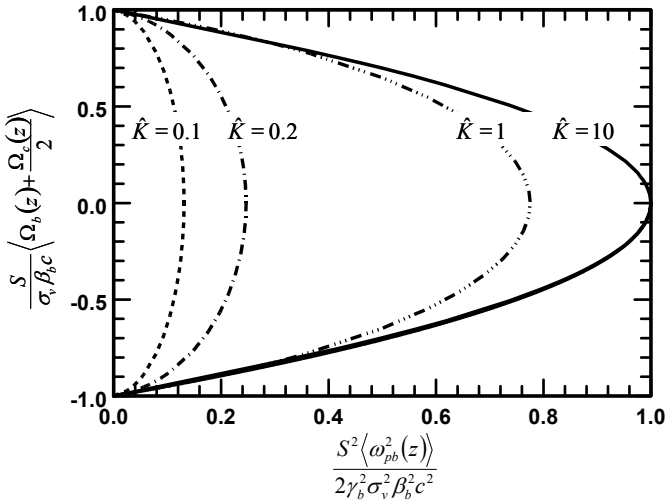

Fig. 2-5 Plot of the normalized angular frequency of beam rotation in the Larmor frame as a function of the effective self-field parameter for normalized perveances $\hat{K}=0.1$, 0.2, 1, and 10 [40].

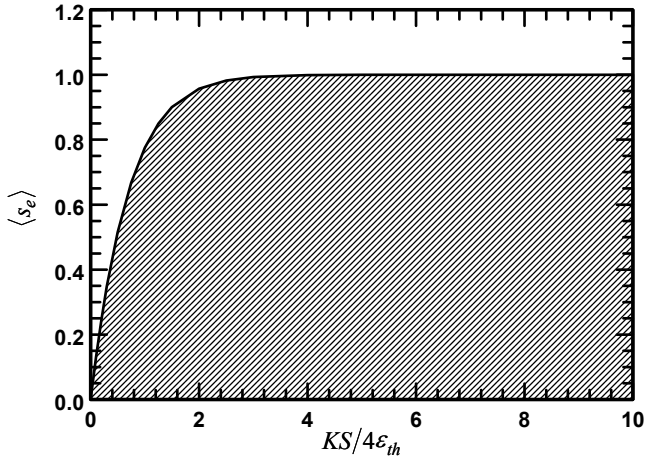

Fig. 2-6 Plot of the critical effective self-field parameter $\langle s_e\rangle$ as a function of $\hat{K}\equiv KS/4\varepsilon_{th}$. The shaded region gives the parameter space for radial beam confinement [40].

2.4 Summary

In this chapter we presented a warm-fluid equilibrium beam theory of a thermal charged-particle beam propagating through a periodic solenoidal focusing field. We solved the warm-fluid beam equations in the paraxial approximation. We derived the rms beam envelope equation and solved it numerically. We also derived the self-consistent Poisson equation, governing the beam density and potential distributions. We computed the density profiles numerically for high-intensity and low-intensity beams. We investigated the temperature effects in such beams, and we found that the thermal beam equilibrium has a bell-shaped density profile and a uniform temperature profile across the beam cross-section. Finally, we discussed the radial confinement of the beam.

3 Kinetic Equilibrium Theory of Thermal Charged-Particle Beams in Periodic Solenoidal Focusing Fields

3.1 Introduction

In general, a kinetic equilibrium theory provides more information about the beam equilibrium. Because a kinetic equilibrium theory requires constants of motion, developing a kinetic equilibrium theory is more difficult than developing a warm-fluid equilibrium theory.

In a kinetic equilibrium theory, the time-independent Vlasov equation is solved for collisionless beams. Any distribution that depends only on constants of motion satisfies the time-independent Vlasov equation and hence represents an equilibrium beam. From a practical point of view, it is useful to know which one of many possible Vlasov equilibrium distributions best represents a laboratory beam. A laboratory beam equilibrium is most likely to be a thermal beam equilibrium because it has the maximum entropy.

As discussed in Sec. 2.1, several Vlasov equilibria have been found for a charged-particle beam in a periodic solenoidal focusing field. The rigid-rotor KV equilibrium distribution [33, 38], despite its unrealistic δ – function phase-space distribution, is often used to model high-intensity beams. This is because it has a simple uniform density profile distribution and it models well the evolution of the rms envelope of any high-intensity beam. However, the KV distribution does not correctly model actual transverse density profiles observed in experiments. An approximate kinetic thermal equilibrium has

also been found in periodic solenoidal magnetic focusing fields with sufficiently small vacuum phase advances [35].

Laboratory beams are usually not in isothermal equilibrium. They may have different transverse and longitudinal temperatures, $T_\perp$ and $T_\parallel$. In circumstances where temperature relaxation due to collisions and nonlinear forces is slow compared to the lifetime of the beam, is it useful to study non-isothermal beam equilibrium.

In this chapter we present a kinetic theory describing an adiabatic thermal equilibrium of an intense charged-particle beam propagating through a periodic solenoidal magnetic focusing field. For continuous beams with long pulses, the longitudinal energy spread is small such that the longitudinal motion can be treated as "cold" and decoupled from the transverse motion which is kept nonrelativistic. The beam pulsates in transverse directions adiabatically like an ideal gas in an adiabatic process, in which the invariant is the product of the transverse temperature and the effective beam area. It differs from the usual thermal equilibrium in which the temperature is kept constant (i.e., independent of the propagation distance) [44, 45]. In the present treatment, the Hamiltonian for single particle motion is analyzed to find the approximate and exact invariants of motion, i.e., a scaled transverse Hamiltonian (nonlinear space charge included), and the angular momentum, from which the beam equilibrium distribution is constructed. The approximation of the scaled transverse Hamiltonian as an invariant of motion is validated analytically for highly emittance-dominated beams and highly space-charge-dominated beams, and is numerically tested to be valid for cases in between with moderate vacuum phase advances ($\sigma_v < 90°$). The beam envelope and emittances are determined self-consistently with the beam equilibrium distribution. Because the distribution function has

a Maxwell-Boltzmann form, it solves not only the Vlasov equation but also the Fokker-Planck equation. It is expected to be stable in a similar manner as the beam thermal equilibrium in a smooth-focusing approximation [44, 45].

This chapter is organized as follows. In Sec. 3.2, the theoretical model is introduced; exact and approximate constants of motion are found for the single-particle Hamiltonian in the paraxial approximation; and the equilibrium distribution is constructed. In Sec. 3.3, the statistical properties of the beam equilibrium, such as the beam envelope equation, emittances and beam temperature, are discussed. In Sec. 3.4, the numerical calculations of the beam density and potential are presented. Finally, a summary is presented in Sec. 3.5.

3.2 Beam Equilibrium Distribution

We consider a continuous, intense charged-particle beam propagating with constant axial velocity $\beta_b c\mathbf{e}_z$ through an applied periodic solenoidal magnetic focusing field. The periodic solenoidal magnetic focusing field is described by (2.2.1).

The single-particle Hamiltonian can be written as

$$H = \left[m^2c^4 + \left(c\mathbf{P} - q\mathbf{A}\right)^2\right]^{1/2} + q\phi^{self}, \qquad (3.2.1)$$

where the canonical momentum $\mathbf{P}$ is related to the mechanical momentum $\mathbf{p}$ by $\mathbf{P} = p + q\mathbf{A}/c$, $\mathbf{A} = \mathbf{A}^{ext} + \mathbf{A}^{self}$ is the vector potential for the total magnetic field, $\mathbf{A}^{self}$ is the vector potential for the self-magnetic field, $\mathbf{A}^{ext}\left(x,y,s\right) = B_z\left(s\right)\left(-y\hat{\mathbf{e}}_x + x\hat{\mathbf{e}}_y\right)/2$ is the vector potential for the applied magnetic field, ϕ^{self} is the scalar potential for self-electric field, m and q are particle rest mass and charge, and c is the speed of light in vacuum. The scalar and vector potentials ϕ^{self} and $\mathbf{A}^{self}$ are related by Eq. (2.2.4).

In the paraxial approximation, we assume $\nu/\gamma_b^3\beta_b^2 << 1$, where $\nu \equiv q^2 N_b/mc^2$ is the Budker parameter [22] of the beam, $N_b = \int^{\infty} n_b(x,y,s)dxdy = const$ is the number of particles per unit axial length, and $\gamma_b = \left(1-\beta_b^2\right)^{-1/2}$ is the relativistic mass factor, as in Sec. 2.2. The axial energy is approximately

$$\gamma_b mc^2 \cong \left(m^2c^4 + c^2P_z^2\right)^{1/2}. \qquad (3.2.2)$$

Because $\nu/\gamma_b^3\beta_b^2 << 1$, the longitudinal particle motion can be decoupled from the transverse particle motion, and the total Hamiltonian for single particle motion is approximated by

$$H \approx \gamma_b mc^2 + H_\perp, \qquad (3.2.3)$$

where the longitudinal Hamiltonian $H_\parallel = \gamma_b mc^2$ is a constant.

We introduce the reduced distribution function $f_b(x,y,P_x,P_y,s)$ defined by [46]

$$f_b(x,y,P_x,P_y,s) = \int dH\, f_{b6D}^0(x,y,P_x,P_y,-H,s), \qquad (3.2.4)$$

where f_b^0 is the distribution function which satisfies nonlinear Vlasov equation. The reduced distribution function $f_b(x,y,P_x,P_y,s)$ satisfies nonlinear Vlasov equation integrated over H (see, for example, Sec. 5.2.2 in Ref. [46]). We assume that the distribution function $f_{b6D}^0(x,y,P_x,P_y,-H,s)$ has a narrow energy spread about the constant value $H = \gamma_b mc^2$ such that axial velocity of the beam is a constant, $V_z \cong \beta_b c$, consistent with the present paraxial treatment.

The normalized transverse Hamiltonian $\hat{H}_\perp = H_\perp/\gamma_b m\beta_b^2 c^2$ is expressed as

$$\hat{H}_\perp\left(x,y,P_x,P_y,s\right)=\frac{1}{2}\left\{\left[\hat{P}_x+\sqrt{\kappa_z(s)}y\right]^2+\left[\hat{P}_y-\sqrt{\kappa_z(s)}x\right]^2\right\}+\frac{K}{2qN_b}\phi^{self}, \tag{3.2.5}$$

where $\sqrt{\kappa_z(s)}$ is the focusing parameter defined in Eq. (2.2.30), $\hat{\mathbf{P}}_\perp=\mathbf{P}_\perp/\gamma_b m\beta_b c$, and $K\equiv 2q^2N_b/\gamma_b^3 m\beta_b^2c^2$ is the beam perveance. The scalar and vector potentials for the self-electric and self-magnetic fields satisfy $\nabla_\perp^2\phi^{self}=-4\pi q n_b(x,y,s)$, $\nabla_\perp^2\mathbf{A}^{self}=-4\pi\beta_b cqn_b(x,y,s)\hat{\mathbf{e}}_z$ and are related by Eq. (2.2.4). Associated with the Hamiltonian in Eq. (3.2.5) equations of motion are

$$\frac{d^2x}{ds^2}-2\sqrt{\kappa_z(s)}\frac{dy}{ds}-\frac{d\sqrt{\kappa_z(s)}}{ds}y+\frac{K}{2qN_b}\frac{\partial\phi^{self}}{\partial x}=0, \tag{3.2.6}$$

$$\frac{d^2y}{ds^2}+2\sqrt{\kappa_z(s)}\frac{dx}{ds}+\frac{d\sqrt{\kappa_z(s)}}{ds}x+\frac{K}{2qN_b}\frac{\partial\phi^{self}}{\partial y}=0. \tag{3.2.7}$$

In order to simplify the transverse Hamiltonian $\hat{H}_\perp\left(x,y,P_x,P_y,s\right)$, we perform a two-step canonical transformation. The first step is to transform from the Cartesian coordinates into the Larmor frame which rotates with one half of the cyclotron frequency relative to the laboratory frame. The second step is a Courant-Snyder type of transformation. The first transformation uses the second type of the generating function

$$\widetilde{F}_2\left(x,y;\widetilde{P}_x,\widetilde{P}_y,s\right)=\left[x\cos\varphi(s)-y\sin\varphi(s)\right]\widetilde{P}_x+\left[x\sin\varphi(s)+y\cos\varphi(s)\right]\widetilde{P}_y, \tag{3.2.8}$$

where $\varphi(s)=\int_0^s\sqrt{\kappa_z(s)}ds$. The transformation is

$$\widetilde{x}=\frac{\partial\widetilde{F}_2}{\partial\widetilde{P}_x}=x\cos\varphi(s)-y\sin\varphi(s), \tag{3.2.9}$$

$$\widetilde{y}=\frac{\partial\widetilde{F}_2}{\partial\widetilde{P}_y}=x\sin\varphi(s)+y\cos\varphi(s), \tag{3.2.10}$$

$$P_x = \frac{\partial \widetilde{F}_2}{\partial x} = \widetilde{P}_x \cos\varphi(s) + \widetilde{P}_y \sin\varphi(s), \tag{3.2.11}$$

$$P_y = \frac{\partial \widetilde{F}_2}{\partial y} = -\widetilde{P}_x \sin\varphi(s) + \widetilde{P}_y \cos\varphi(s). \tag{3.2.12}$$

The transverse Hamiltonian after the first transformation is expressed as

$$\begin{aligned} \widetilde{H}_\perp(\widetilde{x},\widetilde{y},\widetilde{P}_x,\widetilde{P}_y,s) &= \hat{H}_\perp(x,y,P_x,P_y,s) + \frac{\partial \widetilde{F}_2}{\partial s} \\ &= \frac{1}{2}\left[\widetilde{P}_x^2 + \widetilde{P}_y^2 + \kappa_z(s)(\widetilde{x}^2 + \widetilde{y}^2)\right] + \frac{K}{2qN_b}\phi^{self}(\widetilde{x},\widetilde{y},s). \end{aligned} \tag{3.2.13}$$

Note that $(\partial^2/\partial x^2 + \partial^2/\partial y^2)\phi^{self}(x,y,s) = (\partial^2/\partial \widetilde{x}^2 + \partial^2/\partial \widetilde{y}^2)\phi^{self}(\widetilde{x},\widetilde{y},s)$. Equations of motion associated with the transverse Hamiltonian in Eq. (3.2.13) are

$$\frac{d^2\widetilde{x}}{ds^2} + \kappa_z(s)\widetilde{x} + \frac{K}{2qN_b}\frac{\partial \phi^{self}}{\partial \widetilde{x}} = 0, \tag{3.2.14}$$

$$\frac{d^2\widetilde{y}}{ds^2} + \kappa_z(s)\widetilde{y} + \frac{K}{2qN_b}\frac{\partial \phi^{self}}{\partial \widetilde{y}} = 0. \tag{3.2.15}$$

The second canonical transformation uses the second type of the generating function

$$\overline{F}_2(\widetilde{x},\widetilde{y};\overline{P}_x,\overline{P}_y,s) = \frac{\widetilde{x}}{w(s)}\left[\overline{P}_x + \frac{1}{2}\frac{dw(s)}{ds}\widetilde{x}\right] + \frac{\widetilde{y}}{w(s)}\left[\overline{P}_y + \frac{1}{2}\frac{dw(s)}{ds}\widetilde{y}\right], \tag{3.2.16}$$

where $w(s)$ satisfies the differential equation

$$\frac{d^2w(s)}{ds^2} + \kappa_z(s)w(s) - \frac{K}{2r_{brms}^2(s)}w(s) = \frac{1}{w^3(s)}, \tag{3.2.17}$$

and $r_{brms}(s)$ is the rms beam radius. It will be shown in Sec. 3.3 that the function $w(s)$ is related to the rms beam radius [see Eq. (3.3.2)]. The transformation is

$$\overline{x} = \frac{\partial \overline{F}_2}{\partial \overline{P}_x} = \frac{\widetilde{x}}{w(s)}, \tag{3.2.18}$$

$$\bar{y} = \frac{\partial \bar{F}_2}{\partial \bar{P}_y} = \frac{\tilde{y}}{w(s)}, \tag{3.2.19}$$

$$\tilde{P}_x = \frac{\partial \bar{F}_2}{\partial \tilde{x}} = \frac{1}{w(s)}\left[\bar{P}_x + \tilde{x}\frac{dw(s)}{ds}\right], \tag{3.2.20}$$

$$\tilde{P}_y = \frac{\partial \bar{F}_2}{\partial \tilde{y}} = \frac{1}{w(s)}\left[\bar{P}_y + \tilde{y}\frac{dw(s)}{ds}\right]. \tag{3.2.21}$$

Using Eqs. (3.2.18)-(3.2.21), the transverse Hamiltonian is transformed into

$$\begin{aligned} &\bar{H}_\perp\left(\bar{x},\bar{y},\bar{P}_x,\bar{P}_y,s\right) \\ &= \frac{1}{2w^2(s)}\left[\bar{P}_x^2 + \bar{P}_y^2 + \bar{x}^2 + \bar{y}^2\right] + \frac{K}{2qN_b}\phi^{self}\left(\bar{x},\bar{y},s\right) + \frac{K}{4r_{brms}^2(s)}w^2(s)\left(\bar{x}^2 + \bar{y}^2\right). \end{aligned} \tag{3.2.22}$$

The equations of motion associated with the Hamiltonian in Eq. (3.2.22) are

$$\frac{d\bar{x}}{ds} = \frac{\partial \bar{H}_\perp}{\partial \bar{P}_x} = \frac{\bar{P}_x}{w^2(s)}, \tag{3.2.23}$$

$$\frac{d\bar{y}}{ds} = \frac{\partial \bar{H}_\perp}{\partial \bar{P}_y} = \frac{\bar{P}_y}{w^2(s)}, \tag{3.2.24}$$

$$\frac{d\bar{P}_x}{ds} = -\frac{\partial \bar{H}_\perp}{\partial \bar{x}} = -\frac{\bar{x}}{w^2(s)} - \frac{K}{2qN_b}\frac{\partial \phi^{self}}{\partial \bar{x}} - \frac{K}{2r_{brms}^2(s)}w^2(s)\bar{x}, \tag{3.2.25}$$

$$\frac{d\bar{P}_y}{ds} = -\frac{\partial \bar{H}_\perp}{\partial \bar{y}} = -\frac{\bar{y}}{w^2(s)} - \frac{K}{2qN_b}\frac{\partial \phi^{self}}{\partial \bar{y}} - \frac{K}{2r_{brms}^2(s)}w^2(s)\bar{y}. \tag{3.2.26}$$

In order to construct a beam equilibrium distribution, we need to find constants of motion of the system. Two constants of motion can be found using the transverse Hamitonian in Eq. (3.2.22). It is readily shown that the canonical angular momentum P_θ is a constant of motion, i.e.,

$$\frac{dP_\theta}{ds} = 0. \tag{3.2.27}$$

In deriving Eq. (3.2.27), we have used Eqs. (3.2.23)-(3.2.26) and the axial symmetry property of the self-field potential, i.e., $\hat{\phi}^{self}$ is only a function of $\bar{r} = \sqrt{\bar{x}^2 + \bar{y}^2}$ and s.

We also find that the scaled transverse Hamiltonian for single particle motion

$$\overline{E} \equiv w^2(s)\overline{H}_\perp\left(\bar{x}, \bar{y}, \overline{P}_x, \overline{P}_y, s\right) \tag{3.2.28}$$

is an approximate invariant. The transverse Hamiltonian is a highly oscillating function. We use the periodic function $w^2(s)$ to scale the transverse Hamiltonian and to eliminate the oscillations such that the scaled transverse Hamiltonian is an approximate invariant with small residual oscillations. As will be discussed in Sec. 3.3, the small residual oscillations are numerically estimated to be a few percent. Using Eqs. (3.2.23)-(3.2.26), the derivative of the scaled transverse Hamiltonian can be evaluated, giving

$$\begin{aligned}\frac{d\overline{E}}{ds} &= \frac{d}{ds}\left\{\frac{1}{2}\left(\bar{x}^2 + \bar{y}^2 + \overline{P}_x^2 + \overline{P}_y^2\right) + \frac{K}{2qN_b}w^2(s)\phi^{self}(\bar{r}, s) + \frac{Kw^4(s)}{4r_{brms}^2(s)}\bar{r}^2\right\} \\ &= \frac{\partial}{\partial s}\left[\frac{K}{2qN_b}w^2(s)\phi^{self}(\bar{r}, s) + \frac{Kw^4(s)}{4r_{brms}^2(s)}\bar{r}^2\right].\end{aligned} \tag{3.2.29}$$

It is readily shown that $d\overline{E}/ds$ is approximately zero in two limiting cases: (a) a highly space-charged-dominated beam with $SK/\varepsilon_{th} >> 1$, and (b) a highly emittance-dominated beam with $SK/\varepsilon_{th} \to 0$, where ε_{th} is the thermal beam emittance defined later in Eq. (3.3.8). For a highly space-charge-dominated beam with $SK/\varepsilon_{th} >> 1$,

$$\phi_{cold}^{self}(\bar{r}, s) \cong -\frac{qN_b w^2(s)}{2r_{brms}^2(s)}\bar{r}^2, \text{ for } r < \sqrt{2}r_{brms} \tag{3.2.30}$$

and $d\overline{E}/ds \cong 0$. For a highly emittance-dominated beam with $SK/\varepsilon_{th} \to 0$, $\phi_{emit}^{self} \cong 0$ and $d\overline{E}/ds = 0$. For cases in which the space-charge effect is comparable to the emittance effect, we will numerically demonstrate in Sec. 3.4 that $d\overline{E}/ds \cong 0$.

We choose the reduced beam equilibrium distribution in the form similar to the Maxwell-Boltzman distribution, i.e.,

$$f_b = \overline{C}\, exp\left[-\beta\left(\overline{E} - \overline{\omega}_b \overline{P}_\theta\right)\right], \tag{3.2.31}$$

where $\overline{C}$, β and $\overline{\omega}_b$ are constants. $\overline{C}$ is an integration constant, β is related to the beam emittance, and $\overline{\omega}_b$ is the rotation frequency relative to the Larmor frame. Note that $\overline{\omega}_b = 0$ for Brillouin flow and $\overline{\omega}_b \neq 0$ for general flows in which there is magnetic flux on the emitter. Since $\overline{P}_\theta$ and $\overline{E}$ are the constants of motion, the distribution function f_b defined in Eq. (3.2.31) is indeed a Vlasov equilibrium, i.e., $\partial f_b/\partial s = 0$.

3.3 Statistical Properties

In this section, we will discuss the statistical properties of the kinetic thermal equilibrium developed in Sec. 3.2, including the rms beam radius, rms emittance and thermal emittance, flow velocity, beam temperature, and beam density profile.

The distribution function described in Eq. (3.2.31) has the following statistical properties. First, the rms beam radius

$$r_{brms}^2(s) \equiv \left\langle x^2 + y^2 \right\rangle_\Gamma = N_b^{-1} \iint \left(x^2 + y^2\right) f_b \, d\bar{x} d\bar{y} d\overline{P}_x d\overline{P}_y \tag{3.3.1}$$

can be evaluated to yield

$$r_{brms}^2(s) = \frac{2}{\beta\left(1-\overline{\omega}_b^2\right)} w^2(s) \equiv \frac{\varepsilon_T}{2} w^2(s), \tag{3.3.2}$$

where we have introduced the concept of the total emittance $\varepsilon_T \equiv 4\beta^{-1}\left(1-\overline{\omega}_b^2\right)^{-1}$. Substituting Eq. (3.3.2) into Eq. (3.2.17), we arrive at the rms envelope equation

$$\frac{d^2 r_{brms}}{ds^2} + \kappa_z(s) r_{brms} - \frac{K}{2r_{brms}} = \frac{\varepsilon_T^2}{4r_{brms}^3}. \qquad (3.3.3)$$

Second, the rms beam emittance of the beam equilibrium described in Eq. (3.2.31) are given in the Larmor frame by

$$\varepsilon_{\tilde{x}rms} = \sqrt{\left\langle \tilde{x}^2 \right\rangle_\Gamma \left\langle \tilde{x}'^2 \right\rangle_\Gamma - \left\langle \tilde{x}\tilde{x}' \right\rangle_\Gamma^2} = \varepsilon_T / 4 = const. \qquad (3.3.4)$$

Similarly, $\varepsilon_{\tilde{y}rms} = \varepsilon_T / 4 = const$. Note that Eq. (3.3.3) agrees with the well-known rms envelope equation in Ref. [43] with the interpretation of the total emittance in Eq. (3.3.2). As a third statistical property, in dimensional units, the average (macroscopic flow) transverse velocity of the beam equilibrium is given in the Larmor frame by

$$\begin{aligned} &\mathbf{V}_\perp(r,s) \qquad (3.3.5)\\ = \;& \left[n_b w^2(s)\right]^{-1} \iint \mathbf{v}_\perp f_b d\overline{P}_x d\overline{P}_y = \frac{r'_{brms}(s)}{r_{brms}(s)} \beta_b c r \hat{\mathbf{e}}_r + \left[\frac{\varepsilon_T \overline{\omega}_b}{2r_{brms}^2(s)} - \sqrt{\kappa_z(s)}\right] \beta_b c r \hat{\mathbf{e}}_\theta , \end{aligned}$$

As the fourth property, the beam equilibrium described by Eq. (3.2.31) has the transverse temperature profile (in dimensional units)

$$k_B T_\perp(s) = \left[n_b w^2(s)\right]^{-1} \frac{m\gamma_b}{2} \int \left(\mathbf{v}_\perp - \mathbf{V}_\perp\right)^2 f_b d\overline{P}_x d\overline{P}_y = \frac{\left(1-\overline{\omega}_b^2\right) m\gamma_b \beta_b^2 c^2 \varepsilon_T^2}{8 r_{brms}^2(s)} , \qquad (3.3.6)$$

where k_B is the Boltzmann constant. Note from Eq. (3.3.6) that the product $T_\perp(s) r_{brms}^2(s)$ is a conserved quantity ($d/ds = 0$) as the beam pulsates transversely; that is, the equation of state is

$$T_{\perp}(s) r_{brms}^2(s) = const\,. \qquad (3.3.7)$$

Since $2\pi r_{brms}^2$ is a measure of the effective area of the beam, Eq. (3.3.7) is analogous to the equation of state for a two-dimensional adiabatic plasma [47]. As the fifth property, the thermal beam emittance in the Larmor frame is

$$\varepsilon_{th}^2 \equiv \frac{1}{\beta_b^2 c^2}\left\langle x^2 \right\rangle_{\Gamma}\left\langle \left(v_x - V_x\right)^2 \right\rangle_{\Gamma} = \frac{k_B T_{\perp}(s) r_{brms}^2(s)}{2\gamma_b m \beta_b^2 c^2} = const\,. \qquad (3.3.8)$$

It follows from Eqs. (3.3.4) and (3.3.8) that $\varepsilon_T^2 = 16\varepsilon_{th}^2 + 16\overline{\omega}_b^2 \varepsilon_{\tilde{x}rms}^2$, where the term $16\overline{\omega}_b^2 \varepsilon_{\tilde{x}rms}^2$ corresponds to the contribution from the average azimuthal motion in the Larmor frame to the total emittance. The rms envelope equation (3.3.3) can also be expressed as

$$\frac{d^2 r_{brms}(s)}{ds^2} - \frac{\Omega_b(s)}{\beta_b^2 c^2}\left[\Omega_b(s) + \Omega_c(s)\right] r_{brms}(s) - \frac{K}{2r_{brms}(s)} = \frac{4\varepsilon_{th}^2}{r_{brms}^3(s)}. \qquad (3.3.9)$$

where $\Omega_b(s) = \overline{\omega}_b \varepsilon_T \beta_b c / 2r_{brms}^2(s) - \Omega_c(s)/2$ and $\Omega_c(s) = qB_z(s)/\gamma_b mc$ is the relativistic cyclotron frequency. Finally, the beam density profile is

$$\begin{aligned} & n_b(r,s) = w^{-2}(s) \iint f d\overline{P}_x d\overline{P}_y \qquad (3.3.10) \\ = \quad & \frac{4\pi \overline{C} \varepsilon_{th}^2}{r_{brms}^2(s)} exp\left\{ -\left[\frac{K}{2} + \frac{4\varepsilon_{th}^2}{r_{brms}^2(s)} \right] \frac{r^2}{4\varepsilon_{th}^2} - \frac{q}{\gamma_b^2 k_B T_{\perp}(s)} \phi^{self}(r,s) \right\}, \end{aligned}$$

where the scalar potential for the self-electric field is determined by the Poisson equation

$$\frac{1}{r}\frac{\partial}{\partial r}\left(r \frac{\partial \phi^{self}}{\partial r} \right) = -4\pi q n_b(r,s). \qquad (3.3.11)$$

It is worth to note that in the paraxial approximation, the total number of particles per unit length is kept constant, i.e., $N_b = \int_0^{\infty} n_b(r,s) 2\pi r dr = const$. This requires the on-axis

self-electric potential $\phi^{self}(s, r=0)$ to vary as a function of the longitudinal distance, which will be determined numerically in Sec. 3.4.

It is readily shown that the thermal equilibrium density distribution in Eq. (3.3.10) recovers the well-known thermal rigid-rotor equilibrium in a constant magnetic focusing field [22, 44] by setting $d^2 r_{brms}/ds^2 = 0$ in Eq. (3.3.9).

It is worth pointing out that because the derivation of the theory does not actually assume that the magnetic field profile defined in Eq. (2.2.1) is periodic, it is valid not only for the periodic solenoid magnetic field but also for arbitrarily varying solenoid magnetic fields. Therefore, our results apply for the periodic focusing channel as well as for the matching section between the source and the periodic focusing channel. We will discuss numerical examples in a periodic focusing channel in Sec. 3.4 and compare the theoretical results with the UMER [34] experimental measurements in a short matching solenoid channel in Chapter 5.

3.4 Numerical Calculations of Thermal Beam Equilibria

In this section, we illustrate examples of adiabatic thermal beam equilibria in a periodic solenoidal focusing field and the temperature and beam rotation effects with numerical calculations. We also demonstrate numerically that $d\overline{E}/ds \cong 0$, as promised in Sec. 3.2. A numerical module has been added to the PFB2D code [48] to solve the rms envelope equation (3.3.9) which determines the rms beam radius given the periodic solenoidal magnetic field and beam perveance, and Eqs. (3.3.10) and (3.3.11) which determine the beam density and scalar potential for the self-electric field.

We consider a thermal beam focused by a periodical solenoidal focusing magnetic field defined by the ideal periodic step function $\kappa_z(s) = \kappa_z(s+S)$ with

$$\sqrt{\kappa_z(s)} = \begin{cases} \sqrt{\kappa_{z0}} = const, & -\eta/2 < s/S < \eta/2, \\ 0, & \eta/2 < s/S < 1-\eta/2, \end{cases} \qquad (3.4.1)$$

where η is the filling factor of the periodic solenoidal magnetic focusing field. In Fig. 3-1, the profile of the normalized axial magnetic field $S\sqrt{\kappa_z(s)}$ is plotted as a dashed curve, and the normalized rms beam envelope $\hat{r}_{brms} \equiv r_{brms}/\sqrt{4\varepsilon_{th}S}$ for the thermal beam is plotted as a solid curve. The system parameters are $S\sqrt{\kappa_z(0)} = 2.12$, $\eta = 0.4$, $\hat{K} \equiv SK/4\varepsilon_{th} = 10$ and $\overline{\omega}_b = 0$. The vacuum and space-charge-depressed phase advances of the particle betatron oscillations over one lattice period are evaluated to be $\sigma_0 \equiv \varepsilon_T \int_0^S ds/2r_{brms0}^2 = 78.9°$ and $\sigma = \varepsilon_T \int_0^S ds/2r_{brms}^2 = 10.7°$, respectively.

In Fig. 3-2, the beam density relative to the peak density $n(r,s)/n(0,s)$ is plotted as a function of the radius relative to the Debye length [see Eq. (2.3.6)] at $s = 0$ for the same beam as in Fig. 3-1. The density has a flat top near the center of the beam and drops to zero within a few Debye length near the edge of the beam.

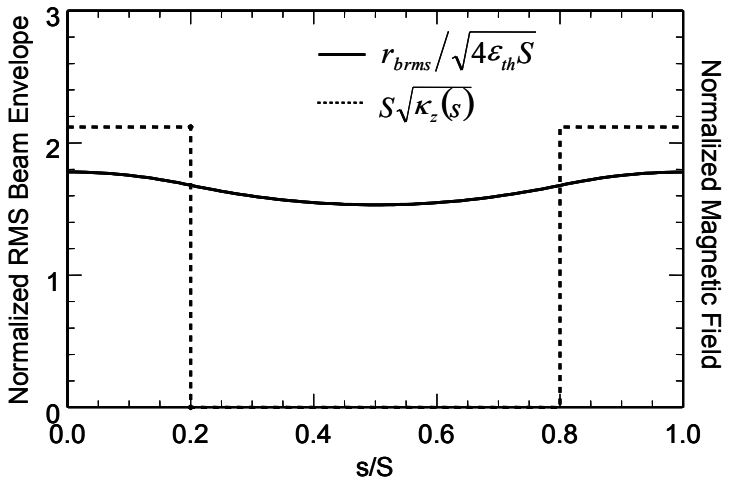

Fig. 3-1 Plots of the normalized axial magnetic field $S\sqrt{\kappa_z(s)}$ (dashed curve) and beam rms envelope $r_{brms}/\sqrt{4\varepsilon_{th}S}$ (solid curve) versus the axial propagation distance s/S for a periodically focused adiabatic thermal beam equilibrium in an applied magnetic field described by the periodic step-function lattice in Eq. (3.4.1). Here, the choice of system parameters corresponds to $S\sqrt{\kappa_z(0)} = 2.12$, $\eta = 0.4$ $(\sigma_0 = 80°)$, $SK/4\varepsilon_{th} = 10.0$, and $\overline{\omega}_b = 0$ [42].

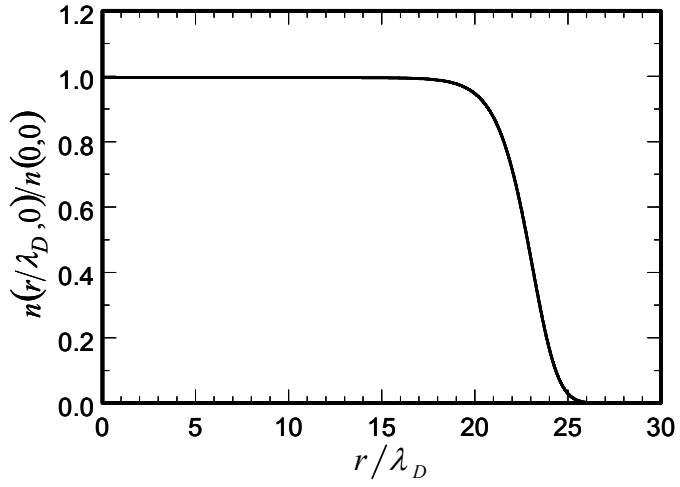

Fig. 3-2 Plot of the relative beam density versus r/λ_D at $s = 0$ for the same beam and focusing field as in Fig. 3-1. Here, $r_{brms} = 16.1\lambda_D$ and the beam densities are normalized to the peak density [42].

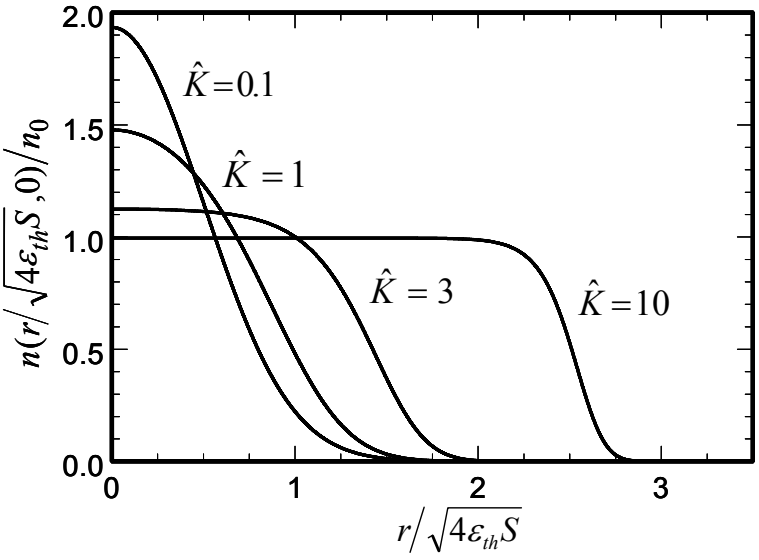

Fig. 3-3 Plot of the relative beam density versus $r/\sqrt{4\varepsilon_{th}S}$ for several beams with $SK/4\varepsilon_{th}=0.1$, 1, 3, and 10, and other system parameters the same as in Fig. 3-1. Here, the beam densities are normalized to the peak density of the beam with $SK/4\varepsilon_{th}=10.0$ [42].

In Fig. 3-3, thermal beam density profiles are plotted for $\hat{K}=0.1$, 1, 3, and 10 with the focusing field in Eq. (3.4.1), $S\sqrt{\kappa_z(0)}=2.12$ and no beam rotation in the Larmor frame (i.e., $\overline{\omega}_b=0$). Here, the beam density is normalized to the peak density n_0 of the beam with $SK/4\varepsilon_{th}=10$. The beam density becomes flat near the beam axis as the normalized perveance $\hat{K}\equiv SK/4\varepsilon_{th}$ increases, i.e., as the beam current increases or the temperature decreases.

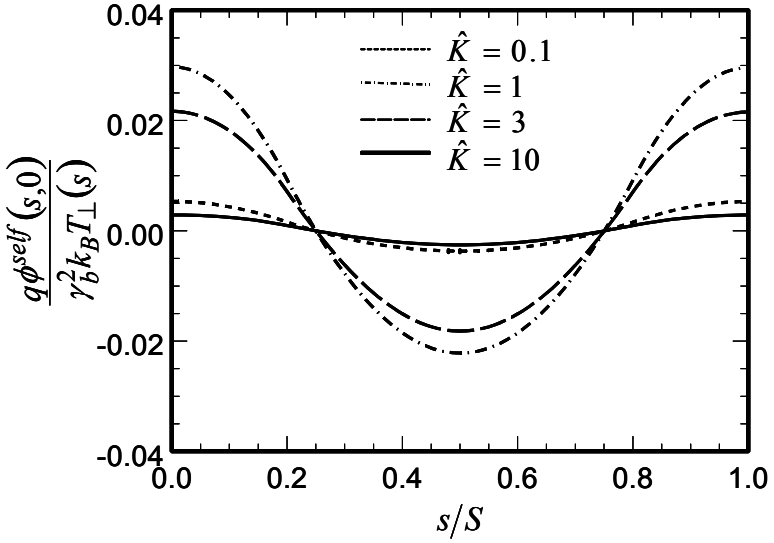

Fig. 3-4 Plot of the on-axis self-electric potential relative to the beam transverse thermal energy as a function of the propagation distance s/S for several beams with $SK/4\varepsilon_{th} = 0.1$, 1, 3, and 10, and other system parameters the same as in Fig. 3-1 [42].

The on-axis self-electric potential is determined numerically, requiring the total number of particles per unit length to be constant. For the detailed numerical method, please refer to Sec. 2.3. In Fig. 3-4, the computed on-axis self-electric potential energy relative to the beam transverse thermal energy $\frac{q\phi^{self}(0,s)}{\gamma_b^2 k_B T_\perp(s)}$ is plotted as a function of s/S for $SK/4\varepsilon_{th} = 0.1$, 1.0, 3.0 and 10.0, and other system parameters the same as in Fig. 3-1. The variation of the on-axis self-electric potential, i.e., the axial electric field, is indeed small.

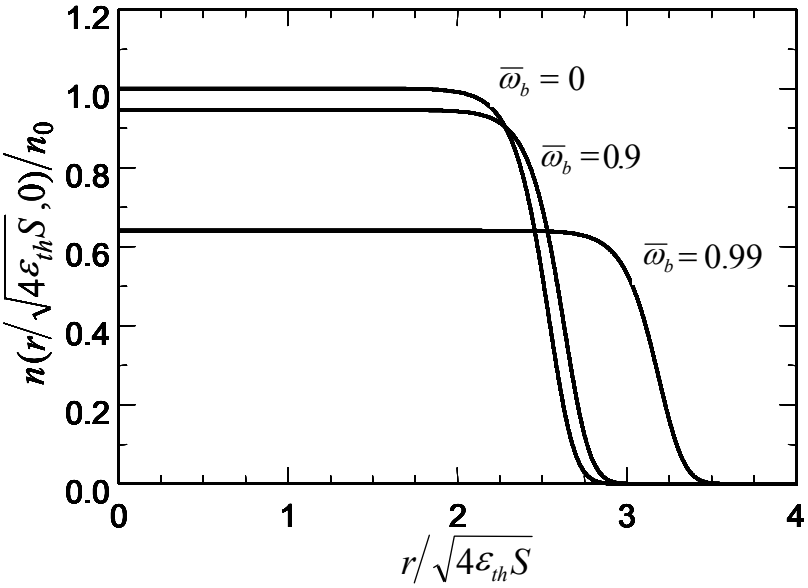

Fig. 3-5 Plot of the relative beam density versus $r/\sqrt{4\varepsilon_{th}S}$ for several beams with $\overline{\omega}_b = 0$, 0.9, and 0.99, and other system parameters the same as in Fig. 3-1. Here, the beam densities are normalized to the peak density of the beam with $\overline{\omega}_b = 0$ [42].

To illustrate the influence of the beam rotation rate in the Larmor frame on the periodically focused thermal beam equilibrium, we plot the relative beam density profiles for three choices of the rotation parameter: $\overline{\omega}_b = 0$, 0.9, and 0.99 in Fig. 3-5. The rest of the system parameters are the same as in Fig. 3-1. As the beam rotation increases, the beam radius increases, and the peak density on the beam axis decreases. However, the Debye length is intact as the beam rotation rate varies.

Finally, we demonstrate the approximate invariant of the scaled transverse Hamiltonian as defined in Eq. (3.2.28) for the cases $SK/\varepsilon_T \to 1$. Instead of showing $d\overline{E}/ds \approx 0$ for each individual particle, which requires very intensive numerical calculations, we demonstrate by numerical calculations that the scaled transverse Hamiltonian $\overline{E}$ is slowly varying at a few radial displacements. In Fig. 3-6, the quantity

$\frac{S}{2\pi\langle\bar{E}\rangle}\frac{d\bar{E}}{ds}$ is plotted as a function of s for various radial displacements $r = 0.5r_{brms}$, r_{brms}, $\sqrt{2}r_{brms}$, and $2r_{brms}$ with other system parameters $\sigma_0 = 80°$, $\hat{K} = 1$ and $\bar{\omega}_b = 0$. Here,

$$\langle\bar{E}\rangle \equiv n_b^{-1}\iint \bar{E} f_b d\bar{P}_x d\bar{P}_y = \frac{1}{2}\left(\bar{r}^2 + \frac{\varepsilon_T}{2}\right) + \frac{K}{2qN_b} w^2(s)\phi^{self}(\bar{r}, s) + \frac{Kw^4(s)}{4r_{brms}^2(s)}\bar{r}^2 \qquad (3.4.2)$$

is the scaled transverse Hamiltonian averaged over the particles located at the same radial displacement. Indeed, a maximum value of $\left|\frac{S}{2\pi\langle\bar{E}\rangle}\frac{d\bar{E}}{ds}\right| = 0.06$, which is achieved at $s/S = 0.2$ and 0.8, assures that $\frac{d\bar{E}}{ds} \cong 0$ in the paraxial approximation.

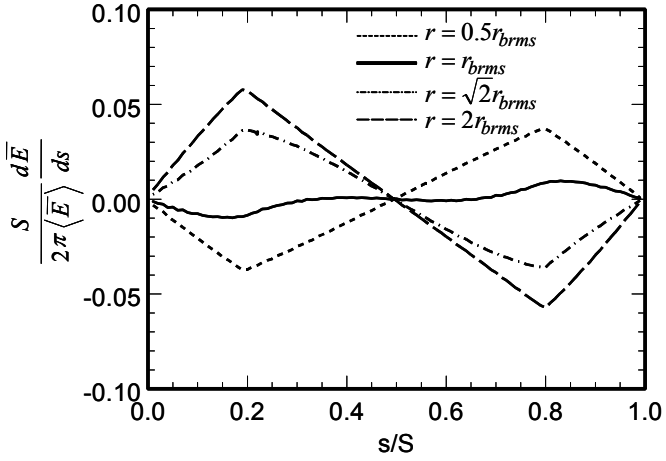

Fig. 3-6. Plot of the quantity $\frac{S}{2\pi\langle\bar{E}\rangle}\frac{d\bar{E}}{ds}$ versus s/S for the four radial displacements of the beam with system parameters $S\sqrt{\kappa_{z0}} = 2.12$, $\eta = 0.4$ $(\sigma_0 = 80°)$, $SK/4\varepsilon_{th} = 1.0$ and $\bar{\omega}_b = 0$ [42].

3.5 Summary

A kinetic adiabatic thermal equilibrium theory was presented for an intense, axisymmetric charged-particle beam propagating through a periodic solenoidal focusing field. The thermal beam distribution function was constructed. The beam rms envelope equation was derived, and the self-consistent nonuniform density profile was calculated. Other statistic properties such as flow velocity, temperature, total emittance and rms thermal emittance, equation of state, and Debye length were studied.

Although the kinetic theory is equivalent to the warm-fluid theory discussed in Chapter 2, it provides more information about the thermal beam equilibrium, especially about the detailed equilibrium distribution function in the particle phase space.

4 Warm-Fluid Equilibrium Theory of Thermal Charged-Particle Beams in Periodic Quadrupole Magnetic Focusing Fields

4.1 Introduction

Many applications of high-intensity beams of charged particles use alternating-gradient (AG) focusing consisting of a periodic quadrupole magnetic focusing field, as discussed in Chapter 1. In general, AG focusing enables much stronger focusing than periodic solenoidal focusing, reducing the beam cross-section (see Ref. [49], and references therein).

However, an AG focusing field does not have the azimuthal symmetry of a periodic solenoidal focusing field which makes theoretical analyses of equilibria of a charged-particle beam in an AG focusing field more difficult.

A kinetic equilibrium has been found for a periodically focused intense charged-particle beam in an alternating-gradient quadrupole magnetic focusing field, i.e., the Kapchinsky-Vladimirsky (KV) beam equilibrium [31]. The KV beam equilibrium uses a δ-function phase-space distribution, which is unphysical. An approximate kinetic thermal equilibrium has also been found in periodic quadrupole magnetic focusing fields with sufficiently small vacuum phase advances [35].

It is difficult to find constants of motion for an intense beam in a periodic quadrupole magnetic focusing field and beam's self-fields, which, in turn, makes a kinetic treatment (in the presence of thermal effects) difficult. Following our success with the warm-fluid

treatment of a thermal charged-particle beam in a periodic solenoidal focusing field (see Chapter 2), we will generalize our warm-fluid treatment to the case of a thermal beam in a periodic quadrupole magnetic focusing field.

In this chapter, a paraxial warm-fluid equilibrium theory of a thermal charged-particle beam in a periodic quadrupole focusing field is presented. The theory predicts that the 4D thermal rms emittance of the beam is conserved. The equilibrium density profile has the same basic properties as the equilibrium density profile for the thermal beam in periodic solenoidal focusing field; that is, for the high-intensity beams, the beam density profile is flat in the center of the beam and then it falls off rapidly within a few Debye lengths. An interesting property of the equilibrium is that the rate at which the density falls is transversely isotropic. Although the density is not self-similar (which is a key assumption in the classic derivation of the rms envelope equations [43]), the constant-density contours are ellipses.

This chapter is organized as follows. In Sec. 4.2, the basic assumptions are presented. Warm-fluid equilibrium equations are used to derive expressions for the flow velocity profile and beam density distribution, the rms beam envelope equations, and a self-consistent Poisson equation. In Sec. 4.3, a numerical technique for computing warm-fluid beam equilibria is discussed. In Sec. 4.4, an example of the thermal beam equilibrium is presented. In Sec. 4.5, the numerical proof of the important relations for the averaged self-electric field, which are used in the establishment of the equilibrium theory in Sec. 4.2, is given. In Sec. 4.6, a summary is presented.

4.2 Warm-Fluid Beam Equilibrium Equations

We consider a thin, continuous, single-species charged-particle beam, propagating with constant axial velocity $V_z\hat{\mathbf{e}}_z$ through an applied quadrupole magnetic focusing field. The applied quadrupole magnetic focusing field inside the beam can be approximated by

$$\mathbf{B}^{ext}(x,y,s) = B_q'(s)\left(y\,\hat{\mathbf{e}}_x + x\hat{\mathbf{e}}_y\right), \qquad (4.2.1)$$

where $s = z$ is the axial coordinate, prime denotes the derivative with respect to z, $B_q'(s) \equiv \partial B_x/\partial y\big|_{(0,0,s)} = \partial B_y/\partial x\big|_{(0,0,s)}$ is the field gradient coefficient which is periodic along the z-axis with periodicity length S, i.e., $B_q'(s) = B_q'(s+S)$.

In the paraxial approximation, $x_{brms} << S$ and $y_{brms} << S$ are assumed, where x_{brms} and y_{brms} are the rms beam envelopes in the x- and y- directions, respectively. The transverse kinetic energy of the beam is assumed to be small compared with its axial kinetic energy, i.e., $|V_z| >> |V_\perp|$. In the paraxial approximation, we assume $\nu/\gamma_b^3\beta_b^2 << 1$, where $\nu \equiv q^2 N_b/mc^2$ is the Budker parameter [22] of the beam, q and m are the particle charge and rest mass, respectively, c is the speed of light in vacuum, $N_b = \int_{-\infty}^{\infty}\int_{-\infty}^{\infty} n_b(x,y,s)dxdy$ is the number of particles per unit axial length, γ_b is the relativistic mass factor, which, to leading order, is $\gamma_b = const = \left(1-\beta_b^2\right)^{-1/2}$ with $\beta_b = V_b/c \cong V_z/c$.

It is convenient to express the self-electric and self-magnetic fields, produced by the space charge and axial current of the beam, in terms of the scalar and vector potentials,

i.e., $\mathbf{E}^{self}(r,s) = -\nabla\phi^{self}(r,s)$ and $\mathbf{B}^{self}(r,s) = \nabla\times\mathbf{A}^{self}(r,s)$. In the paraxial approximation, $\mathbf{A}^{self} = A^{self}\hat{\mathbf{e}}_z = \beta_b\phi^{self}\hat{\mathbf{e}}_z$ and $\mathbf{B}^{self} = -\beta_b\left(\frac{\partial\phi^{self}}{\partial y}\hat{\mathbf{e}}_x - \frac{\partial\phi^{self}}{\partial x}\hat{\mathbf{e}}_y\right)$.

In the paraxial approximation, the warm-fluid equilibrium ($\partial/\partial t = 0$) equations are

$$n_b\,\mathbf{V}\cdot\nabla(\gamma_b m\mathbf{V}) = n_b q\left[-\nabla\phi^{self} + \frac{\mathbf{V}}{c}\times\left(\mathbf{B}^{ext}+\mathbf{B}^{self}\right)\right] - \nabla\cdot\vec{\mathbf{P}}(\mathbf{x}), \tag{4.2.2}$$

$$\nabla\cdot(n_b\mathbf{V}) = 0, \tag{4.2.3}$$

$$\nabla^2\phi^{self}(x,y,s) = -4\pi q\, n_b(x,y,s), \tag{4.2.4}$$

$$p_\perp(x,y,s) = n_b(x,y,s)k_B T_\perp(s), \tag{4.2.5}$$

$$T_\perp(s)x_{brms}(s)y_{brms}(s) = const. \tag{4.2.6}$$

In Eqs. (4.2.2)-(4.2.6), $\vec{\mathbf{P}}(x,y,s) = p_\perp(x,y,s)\left(\hat{\mathbf{e}}_x\hat{\mathbf{e}}_x + \hat{\mathbf{e}}_y\hat{\mathbf{e}}_y\right) + p_{||}(x,y,s)\hat{\mathbf{e}}_z\hat{\mathbf{e}}_z$ is the pressure tensor, $p_\perp(x,y,s)$ and $p_{||}(x,y,s)$ are transverse and parallel thermal pressures, respectively, $T_\perp(s)$ is the transverse beam temperature which remains constant across the cross-section of the beam, the rms beam envelopes $x_{brms}(s)$ and $y_{brms}(s)$ are defined by

$$x_{brms}^2 = \left\langle x^2\right\rangle = N_b^{-1}\int_{-\infty}^{\infty}\int_{-\infty}^{\infty} x^2\, n_b(x,y,s)dxdy \tag{4.2.7}$$

and

$$y_{brms}^2 = \left\langle y^2\right\rangle = N_b^{-1}\int_{-\infty}^{\infty}\int_{-\infty}^{\infty} y^2\, n_b(x,y,s)dxdy\ . \tag{4.2.8}$$

Equation (4.2.6) is the generalization of the adiabatic equation of state for the thin beam propagating in the solenoidal field [see Eq. (2.2.10) from Chapter 2]. The beam motion is adiabatic. As in Chapter 2, we will not analyze the axial component of the momentum

equation (4.2.2). Note that for the beam in the paraxial approximation, we can approximate $\nabla^2 \cong \frac{\partial^2}{\partial x^2} + \frac{\partial^2}{\partial y^2}$ to leading order in the Poisson equation (4.2.4).

We seek a solution for the equilibrium beam velocity profile of the form

$$\mathbf{V}_\perp(x,y,s) = x\frac{x'_{brms}(s)}{x_{brms}(s)}\beta_b c\hat{\mathbf{e}}_x + y\frac{y'_{brms}(s)}{y_{brms}(s)}\beta_b c\hat{\mathbf{e}}_y . \qquad (4.2.9)$$

Substituting Eqs. (4.2.5) and (4.2.9) into the x-component of the momentum equation (4.2.2), we obtain

$$\begin{aligned} & n_b(x,y,s)\beta_b^2 c^2 x\left\{\left[\frac{x'_{brms}(s)}{x_{brms}(s)}\right]^2 + \left[\frac{x'_{brms}(s)}{x_{brms}(s)}\right]'\right\} \qquad (4.2.10) \\ = \; & \frac{qn_b(x,y,s)}{\gamma_b m}\left[-\left(1-\beta_b^2\right)\frac{\partial\phi^{self}(x,y,s)}{\partial x} - x\beta_b B'_q(s)\right] - \frac{k_B T_\perp(s)}{\gamma_b m}\frac{\partial n_b(x,y,s)}{\partial x}, \end{aligned}$$

or

$$\begin{aligned} & \frac{\partial}{\partial x}\ln[n_b(x,y,s)] \qquad (4.2.11) \\ = \; & -\frac{\gamma_b m\beta_b^2 c^2}{k_B T_\perp(s)}\left[\frac{x''_{brms}(s)}{x_{brms}(s)} + \kappa_q(s)\right]x - \frac{q}{\gamma_b^2 k_B T_\perp(s)}\frac{\partial\phi^{self}(x,y,s)}{\partial x}, \end{aligned}$$

where

$$\kappa_q(s) \equiv \frac{qB'_q(s)}{m\gamma_b\beta_b c^2} \qquad (4.2.12)$$

is the quadrupole coupling coefficient. Similarly, from the y-component of the momentum equation, we obtain

$$\begin{aligned} & \frac{\partial}{\partial y}\ln[n_b(x,y,s)] \qquad (4.2.13) \\ = \; & -\frac{\gamma_b m\beta_b^2 c^2}{k_B T_\perp(s)}\left[\frac{y''_{brms}(s)}{y_{brms}(s)} - \kappa_q(s)\right]y - \frac{q}{\gamma_b^2 k_B T_\perp(s)}\frac{\partial\phi^{self}(x,y,s)}{\partial y}. \end{aligned}$$

We integrate Eqs. (4.2.11) and (4.2.13) to obtain for the density profile

$$
\begin{aligned}
& n_b(x,y,s) \qquad (4.2.14)\\
= \; & f(s)\exp\left(-\frac{\gamma_b m\beta_b^2 c^2}{2k_B T_\perp(s)}\left\{\left[\frac{x''_{brms}(s)}{x_{brms}(s)}+\kappa_q(s)\right]x^2+\left[\frac{y''_{brms}(s)}{y_{brms}(s)}-\kappa_q(s)\right]y^2\right\}\right)\\
\times \; & \exp\left[-\frac{q\phi^{self}(x,y,s)}{\gamma_b^2 k_B T_\perp(s)}\right],
\end{aligned}
$$

where $f(s)$ is an arbitrary function of s to be determined later [see Eq. (4.2.40)]. It is convenient to rewrite Eq. (4.2.14) as

$$
n_b(x,y,s)=f(s)exp\left\{-\frac{\gamma_b m\beta_b^2 c^2}{2k_B T_\perp(s)}\left[\frac{x^2}{A^2(s)}+\frac{y^2}{B^2(s)}\right]-\frac{q\phi^{self}(x,y,s)}{\gamma_b^2 k_B T_\perp(s)}\right\}, \qquad (4.2.15)
$$

where

$$
A^2(s)\equiv\left[\frac{x''_{brms}(s)}{x_{brms}(s)}+\kappa_q(s)\right]^{-1} \qquad (4.2.16)
$$

and

$$
B^2(s)\equiv\left[\frac{y''_{brms}(s)}{y_{brms}(s)}-\kappa_q(s)\right]^{-1}. \qquad (4.2.17)
$$

Using the density profile in Eq. (4.2.15), we calculate the rms beam envelope in the x-direction. The result is

$$
x_{brms}^2(s)=\frac{k_B T_\perp(s)A^2(s)}{\gamma_b m\beta_b^2 c^2}\left[1-\frac{q}{\gamma_b^2 k_B T_\perp(s)}\left\langle x\frac{\partial\phi^{self}(x,y,s)}{\partial x}\right\rangle\right], \qquad (4.2.18)
$$

where we have used integration by parts and assumed that the beam density at $x=\pm\infty$ is negligibly small, and

$$
\left\langle x\frac{\partial\phi^{self}(x,y,s)}{\partial x}\right\rangle = N_b^{-1}\int_{-\infty}^{\infty}\int_{-\infty}^{\infty} x\frac{\partial\phi^{self}(x,y,s)}{\partial x}n_b(x,y,s)dxdy\,. \qquad (4.2.19)
$$

Similarly, for $y_{brms}(s)$ we obtain

$$y_{brms}^2(s) = \frac{k_B T_\perp(s) B^2(s)}{\gamma_b m \beta_b^2 c^2}\left[1 - \frac{q}{\gamma_b^2 k_B T_\perp(s)}\left\langle y \frac{\partial \phi^{self}(x,y,s)}{\partial y}\right\rangle\right], \qquad (4.2.20)$$

where

$$\left\langle y \frac{\partial \phi^{self}(x,y,s)}{\partial y}\right\rangle = N_b^{-1}\int_{-\infty}^{\infty}\int_{-\infty}^{\infty} y \frac{\partial \phi^{self}(x,y,s)}{\partial y} n_b(x,y,s)\,dxdy\,. \qquad (4.2.21)$$

It is well-known [43] that if the beam density has the simplest elliptical symmetry, i.e.,

$$n_b(x,y,s) = n_b\left(\frac{x^2}{x_{brms}^2(s)} + \frac{y^2}{y_{brms}^2(s)}\right), \qquad (4.2.22)$$

then the averages $\left\langle x \frac{\partial \phi^{self}(x,y,s)}{\partial x}\right\rangle$ and $\left\langle y \frac{\partial \phi^{self}(x,y,s)}{\partial x}\right\rangle$ can be evaluated from the Poisson equation (4.2.4) in the paraxial approximation, i.e.,

$$\left\langle x \frac{\partial \phi^{self}(x,y,s)}{\partial x}\right\rangle = -qN_b \frac{x_{brms}(s)}{x_{brms}(s) + y_{brms}(s)} \qquad (4.2.23)$$

and

$$\left\langle y \frac{\partial \phi^{self}(x,y,s)}{\partial y}\right\rangle = -qN_b \frac{y_{brms}(s)}{x_{brms}(s) + y_{brms}(s)}\,. \qquad (4.2.24)$$

At this point in the derivation, let us assume that Eqs. (4.2.23) and (4.2.24) are satisfied, even though the beam might not have the simplest elliptical symmetry described by Eq. (4.2.22). In the absence of the elliptical symmetry (4.2.22), it is difficult to show Eqs. (4.2.23) and (4.2.24) analytically. However we will demonstrate numerically that Eqs. (4.2.23) and (4.2.24) are in fact satisfied (see Sec. 4.4).

Substituting Eqs. (4.2.23) and (4.2.24) into Eqs. (4.2.18) and (4.2.20) we obtain

$$A^2(s) = \left\{\frac{k_B T_\perp(s)}{\gamma_b m \beta_b^2 c^2 x_{brms}^2(s)}\left[1 + \frac{q^2 N_b}{\gamma_b^2 k_B T_\perp(s)} \frac{x_{brms}(s)}{x_{brms}(s) + y_{brms}(s)}\right]\right\}^{-1} \qquad (4.2.25)$$

and

$$B^2(s)=\left\{\frac{k_B T_\perp(s)}{\gamma_b m\beta_b^2 c^2 y_{brms}^2(s)}\left[1+\frac{q^2 N_b}{\gamma_b^2 k_B T_\perp(s)}\frac{y_{brms}(s)}{x_{brms}(s)+y_{brms}(s)}\right]\right\}^{-1}. \qquad (4.2.26)$$

Finally, substituting Eqs. (4.2.16) and (4.2.17) into Eqs. (4.2.25) and (4.2.26), we arrive at the rms envelope equations

$$x''_{brms}(s)+\kappa_q(s)x_{brms}(s)-\frac{K}{2\left[x_{brms}(s)+y_{brms}(s)\right]}=\frac{k_B T_\perp(s)}{\gamma_b m\beta_b^2 c^2}\frac{1}{x_{brms}(s)} \qquad (4.2.27)$$

and

$$y''_{brms}(s)-\kappa_q(s)y_{brms}(s)-\frac{K}{2\left[x_{brms}(s)+y_{brms}(s)\right]}=\frac{k_B T_\perp(s)}{\gamma_b m\beta_b^2 c^2}\frac{1}{y_{brms}(s)}, \qquad (4.2.28)$$

where $K\equiv 2N_b q^2/\gamma_b^3 m\beta_b^2 c^2$ is the self-field perveance.

We introduce the 2D rms thermal emittances of the beam, ε_{xth} and ε_{yth}, defined by

$$\varepsilon_{xth}^2(s)\equiv(\beta_b c)^{-2}\left\langle x^2\right\rangle_\Gamma\left\langle\left(v_x-V_x\right)^2\right\rangle_\Gamma=\frac{k_B T_\perp(s)x_{brms}^2(s)}{m\gamma_b\beta_b^2 c^2} \qquad (4.2.29)$$

and

$$\varepsilon_{yth}^2(s)\equiv(\beta_b c)^{-2}\left\langle y^2\right\rangle_\Gamma\left\langle\left(v_y-V_y\right)^2\right\rangle_\Gamma=\frac{k_B T_\perp(s)y_{brms}^2(s)}{m\gamma_b\beta_b^2 c^2} \qquad (4.2.30)$$

in the x- and y- directions, respectively. The adiabatic condition in Eq. (4.2.6) implies that

$$\varepsilon_{xth}\varepsilon_{yth}=const. \qquad (4.2.31)$$

This is an important result stating that the product of ε_{xth} and ε_{yth} is conserved, although neither ε_{xth} nor ε_{yth} is conserved by itself.

We introduce the 4D rms thermal emittance ε_{4Dth} defined by

$$\varepsilon_{4Dth}^{4}(s) \equiv (\beta_b c)^{-4} \left\langle x^2 \right\rangle_\Gamma \left\langle y^2 \right\rangle_\Gamma \left\langle (v_x - V_x)^2 \right\rangle_\Gamma \left\langle (v_y - V_y)^2 \right\rangle_\Gamma , \qquad (4.2.32)$$

which is a constant, i.e.,

$$\varepsilon_{4Dth}^{2} = \frac{k_B T_\perp(s) x_{brms}(s) y_{brms}(s)}{m \gamma_b \beta_b^2 c^2} = const . \qquad (4.2.33)$$

Combining Eqs. (4.2.27), (4.2.28), and (4.2.33) yields the following rms beam envelope equations

$$x''_{brms}(s) + \kappa_q(s) x_{brms}(s) - \frac{K}{2[x_{brms}(s) + y_{brms}(s)]} = \frac{\varepsilon_{4Dth}^2}{x_{brms}^2(s) y_{brms}(s)}, \qquad (4.2.34)$$

$$y''_{brms}(s) - \kappa_q(s) y_{brms}(s) - \frac{K}{2[x_{brms}(s) + y_{brms}(s)]} = \frac{\varepsilon_{4Dth}^2}{y_{brms}^2(s) x_{brms}(s)} . \qquad (4.2.35)$$

Substituting Eqs. (4.2.33)-(4.2.35) into Eq. (4.2.15) we obtain the simplified expression for the equilibrium beam density profile

$$\begin{aligned} & n_b(x,y,s) \qquad (4.2.36) \\ = \; & f(s) \exp\left(- \left\{ \frac{K\, y_{brms}(s)}{4\,\varepsilon_{4Dth}^2 \left[x_{brms}(s) + y_{brms}(s) \right]} + \frac{1}{2 x_{brms}^2(s)} \right\} x^2 \right) \\ \times \; & \exp\left(- \left\{ \frac{K\, x_{brms}(s)}{4\varepsilon_{4Dth}^2 \left[x_{brms}(s) + y_{brms}(s) \right]} + \frac{1}{2 y_{brms}^2(s)} \right\} y^2 \right) \\ \times \; & \exp\left(- \frac{q\, \phi^{self}(x,y,s)}{\gamma_b^2 k_B T_\perp(s)} \right) \end{aligned}$$

where the scalar potential for the self-electric field satisfies the Poisson equation

$$\frac{\partial^2 \phi^{self}(x,y,s)}{\partial x^2} + \frac{\partial^2 \phi^{self}(x,y,s)}{\partial y^2} \tag{4.2.37}$$

$$= -4\pi q f(s) exp\left(-\left\{ \frac{K y_{brms}(s)}{4\varepsilon_{4Dth}^2 \left[x_{brms}(s) + y_{brms}(s) \right]} + \frac{1}{2x_{brms}^2(s)} \right\} x^2 \right)$$

$$\times \quad exp\left(-\left\{ \frac{K x_{brms}(s)}{4\varepsilon_{4Dth}^2 \left[x_{brms}(s) + y_{brms}(s) \right]} + \frac{1}{2y_{brms}^2(s)} \right\} y^2 \right)$$

$$\times \quad exp\left(-\frac{q \phi^{self}(x,y,s)}{\gamma_b^2 k_B T_\perp(s)} \right).$$

The velocity and density profiles in Eqs. (4.2.9) and (4.2.36) must satisfy the continuity equation (4.2.3). Substituting Eqs. (4.2.9) and (4.2.36) into Eq. (4.2.3), and integrating over the cross section of the beam yields

$$0 = \left[\frac{x'_{brms}(s)}{x_{brms}(s)} + \frac{y'_{brms}(s)}{y_{brms}(s)} + \frac{1}{f(s)} \frac{df(s)}{ds} \right] \tag{4.2.38}$$

$$- \frac{K}{2\varepsilon_{4Dth}^2} \frac{d}{ds} \left[\frac{x_{brms}(s) y_{brms}(s)}{2} + x_{brms}(s) y_{brms}(s) \left\langle \frac{\phi^{self}(r,s)}{q N_b} \right\rangle \right].$$

Note that Eq. (4.2.38) is equivalent to the conservation of the total number of particles per unit axial length, i.e.,

$$\frac{dN_b}{ds} = 0 \text{ or } N_b = const. \tag{4.2.39}$$

Setting the sum of the first three terms in Eq. (4.2.38) to zero gives

$$f(s) \equiv \frac{C}{x_{brms}(s) y_{brms}(s)}, \tag{4.2.40}$$

where C is a constant of integration.

Finally, the beam density on the axis is

$$n_b(0,0,s) = f(s) \exp\left[-\frac{q \phi^{self}(0,0,s)}{\gamma_b^2 k_B T_\perp(s)} \right], \tag{4.2.41}$$

which will be an important parameter in the numerical calculations.

4.3 Numerical Calculations of Warm-Fluid Beam Equilibria

In this section we discuss our numerical calculations of warm-fluid beam equilibria. The matched rms beam envelopes are determined by solving the rms beam envelope equations (4.2.34) and (4.2.35) with periodic boundary conditions

$$x_{brms}(s) = x_{brms}(s+S), \quad y_{brms}(s) = y_{brms}(s+S). \tag{4.3.1}$$

They are later used in the calculations of the equilibrium beam density and potential using Eqs. (4.2.36) and (4.2.37). For convenience, we introduce the dimensionless parameters and variables

$$\hat{s} = s/S\,,\ \hat{x} = x/\sqrt{4S\,\varepsilon_{4Dth}}\,,\ \hat{y} = y/\sqrt{4S\,\varepsilon_{4Dth}}\,,\ \hat{x}_{brms} = x_{brms}/\sqrt{4S\,\varepsilon_{4Dth}}\,, \tag{4.3.2}$$
$$\hat{y}_{brms} = y_{brms}/\sqrt{4S\,\varepsilon_{4Dth}}\,,\ \hat{\kappa}_q = S^2\kappa_q\,,\ \hat{K} = SK/4\varepsilon_{4Dth}\,,\ \hat{\phi}^{self} = \phi^{self}/qN_b\,.$$

The normalized envelope equations (4.2.34) and (4.2.35) become

$$\hat{x}''_{brms}(\hat{s}) + \hat{\kappa}_q(\hat{s})\hat{x}_{brms}(\hat{s}) - \frac{\hat{K}}{2\left[\hat{x}_{brms}(\hat{s}) + \hat{y}_{brms}(\hat{s})\right]} = \frac{1}{16\hat{x}^2_{brms}(\hat{s})\hat{y}_{brms}(\hat{s})}, \tag{4.3.3}$$

$$\hat{y}''_{brms}(\hat{s}) - \hat{\kappa}_q(\hat{s})\hat{y}_{brms}(\hat{s}) - \frac{\hat{K}}{2\left[\hat{x}_{brms}(\hat{s}) + \hat{y}_{brms}(\hat{s})\right]} = \frac{1}{16\hat{y}^2_{brms}(\hat{s})\hat{x}_{brms}(\hat{s})}. \tag{4.3.4}$$

The normalized Poisson equation (4.2.37) becomes

$$\begin{aligned} &\frac{\partial^2\hat{\phi}^{self}}{\partial\hat{x}^2} + \frac{\partial^2\hat{\phi}^{self}}{\partial\hat{y}^2} \\ = \quad & -\frac{\hat{f}(\hat{s})}{\hat{x}_{rms}(\hat{s})\hat{y}_{brms}(\hat{s})} exp\left\{-\left[\frac{4\hat{K}\,\hat{y}_{brms}(\hat{s})}{\hat{x}_{brms}(\hat{s}) + \hat{y}_{brms}(\hat{s})} + \frac{1}{2\hat{x}^2_{brms}(\hat{s})}\right]\hat{x}^2\right\} \\ \times \quad & exp\left\{-\left[\frac{4\hat{K}\,\hat{x}_{brms}(\hat{s})}{\hat{x}_{brms}(\hat{s}) + \hat{y}_{brms}(\hat{s})} + \frac{1}{2\hat{y}^2_{brms}(\hat{s})}\right]\hat{y}^2\right\} \\ \times \quad & exp\left[-8\hat{K}\,\hat{x}_{brms}(\hat{s})\hat{y}_{brms}(\hat{s})\hat{\phi}^{self}\right], \end{aligned} \tag{4.3.5}$$

where

$$\hat{f}(\hat{s}) = \frac{f(s)}{n_{KV}(0,0,s)} \qquad (4.3.6)$$

and

$$n_{KV}(0,0,s) = \frac{N_b}{\pi a(s) b(s)} \qquad (4.3.7)$$

is the on-axis density of the equivalent KV beam, which has the same rms beam envelopes $x_{brms}(s)$ and $y_{brms}(s)$ as the thermal beam. It also has a constant density across the cross-section of the beam, which is an ellipse with the semi-axes $a(s) = 2x_{brms}(s)$ and $b(s) = 2y_{brms}(s)$.

We calculate the equilibrium potential using the Poisson equation (4.3.5) in the region defined by $-L \le \hat{x} \le L$ and $-L \le \hat{y} \le L$ on a square mesh with a step size of h (see Fig. 4-1). To specify the boundary conditions for $\hat{\phi}(\hat{x},\hat{y},\hat{s})$ on the border of the region, we choose the boundary conditions for $\hat{\phi}(\hat{x},\hat{y},\hat{s})$ to be an asymptotic for the exact solution for potential of the equivalent KV beam [50] for $L >> \hat{x}_{brms}$ and $L >> \hat{y}_{brms}$, i.e.,

$$\hat{\phi}^{self}_{boundary}(\hat{x},\hat{y},\hat{s}) = -2\ln\left[\frac{\sqrt{\hat{x}^2+\hat{y}^2}}{\hat{x}_{brms}+\hat{y}_{brms}}\right] - 1, \qquad (4.3.8)$$

which is derived in Appendix B.

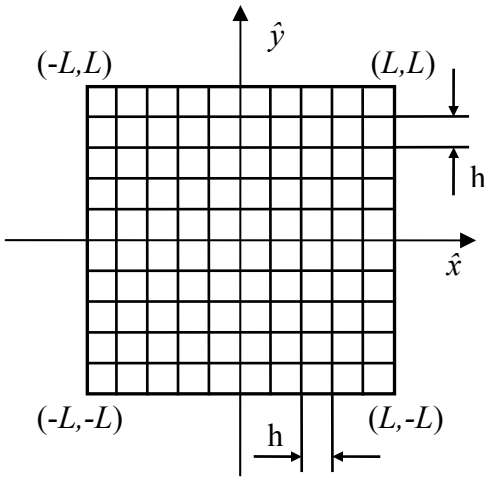

Fig. 4-1 Schematic of the integration region defined by $-L \le \hat{x} \le L$ and $-L \le \hat{y} \le L$ on a square mesh with a step size of h.

Once the equilibrium potential is computed, we compute the normalized equilibrium beam density

$$\begin{aligned} & \hat{n}_b(\hat{x},\hat{y},\hat{s}) \equiv n_b(x,y,s)/n_{KV}(0,0,s) \qquad (4.3.9) \\ = \quad & \hat{f}(\hat{s}) exp\left\{-\left[\frac{4\hat{K}\,\hat{y}_{brms}(\hat{s})}{\hat{x}_{brms}(\hat{s})+\hat{y}_{brms}(\hat{s})}+\frac{1}{2\hat{x}_{brms}^2(\hat{s})}\right]\hat{x}^2\right\} \\ \times \quad & exp\left\{-\left[\frac{4\hat{K}\,\hat{x}_{brms}(\hat{s})}{\hat{x}_{brms}(\hat{s})+\hat{y}_{brms}(\hat{s})}+\frac{1}{2\hat{y}_{brms}^2(\hat{s})}\right]\hat{y}^2\right\} \\ \times \quad & exp\left[-8\hat{K}\,\hat{x}_{brms}(\hat{s})\hat{y}_{brms}(\hat{s})\hat{\phi}^{self}\right]. \end{aligned}$$

We use the Successive Overrelaxation (SOR) method (see, for example, Ref. [51]) to solve Poisson (4.3.5) equation. The function $\hat{f}(\hat{s})$ in Eqs. (4.3.5) and (4.3.9) should be self-consistent with the choice of the total number of particles per unit length, which requires

$$\Delta \equiv 1 - N_b^{-1} \int_{-\infty}^{\infty}\int_{-\infty}^{\infty} n_b(x,y,s)\,dxdy \qquad (4.3.10)$$

$$= \quad 1 - \frac{\hat{f}(\hat{s})}{4\pi\,\hat{x}_{brms}(\hat{s})\hat{y}_{brms}(\hat{s})} \int_{-\infty}^{\infty}\int_{-\infty}^{\infty} exp\left\{ \begin{array}{l} -\left[\dfrac{4\hat{K}\,\hat{y}_{brms}(\hat{s})}{\hat{x}_{brms}(\hat{s})+\hat{y}_{brms}(\hat{s})} + \dfrac{1}{2\hat{x}_{brms}^2(\hat{s})}\right]\hat{x}^2 \\ -\left[\dfrac{4\hat{K}\,\hat{x}_{brms}(\hat{s})}{\hat{x}_{brms}(\hat{s})+\hat{y}_{brms}(\hat{s})} + \dfrac{1}{2\hat{y}_{brms}^2(\hat{s})}\right]\hat{y}^2 \\ -8\hat{K}\hat{x}_{brms}(\hat{s})\hat{y}_{brms}(\hat{s})\hat{\phi}^{self}(\hat{x},\hat{y},\hat{s}) \end{array} \right\} d\hat{x}d\hat{y} = 0.$$

In our numerical calculations, an iterative procedure is applied to determine $\hat{f}(\hat{s})$, and Δ is typically less than 10^{-3}.

4.4 Example of a Warm-Fluid Beam Equilibrium

As an example, we consider a thermal beam, focused by a periodical quadrupole magnetic focusing field defined by the periodic step function $\kappa_q(s) = \kappa_q(s+S)$ illustrated in Fig. 4-2 . The quadrupole coupling coefficient is defined by

$$S^2\kappa_q(s) = \begin{cases} 15, & 0 < s/S < \eta/4, \\ 0, & \eta/4 < s/S < 1/2 - \eta/4, \\ -15, & 1/2 - \eta/4 < s/S < 1/2 + \eta/4, \\ 0, & 1/2 + \eta/4 < s/S < 1 - \eta/4, \\ 15, & 1 - \eta/4 < s/S < 1, \end{cases} \qquad (4.4.1)$$

where η is the filling factor.

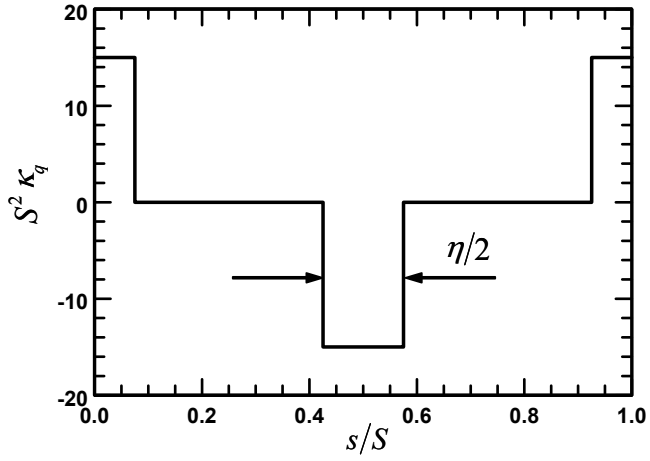

Fig. 4-2 Plot of the normalized quadrupole coupling coefficient $S^2\kappa_q(s)$ versus the normalized axial propagation distance s/S. Here, the choice of system parameters corresponds to $S^2\kappa_q(0)=15$ and $\eta=0.3$.

In Fig. 4-3, the solid curves are the normalized rms envelopes for the warm-fluid beam with $\hat{K} \equiv SK/4\varepsilon_{4Dth} = 4$ and the rest of the system parameters are the same as in Fig. 4-2. For comparison, the dashed curves are the normalized rms beam envelopes for a cold-fluid beam equilibrium. The rms beam envelopes are normalized to $\sqrt{4\varepsilon_{4Dth}S}$. The rms beam envelopes for the cold-fluid beam equilibrium, $x_{brms}^{cold}(s)$ and $y_{brms}^{cold}(s)$, can be determined from Eqs. (4.2.34) and (4.2.35) with the right-hand sides equal to zero. In Fig. 4-3, the effects of the finite temperature enlarge the rms beam envelopes by about 3%.

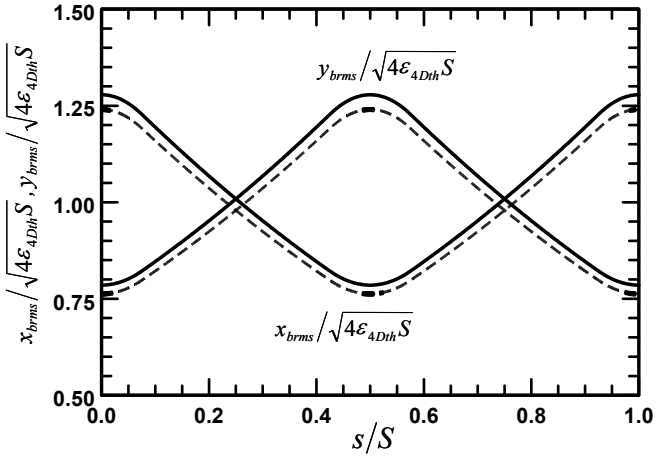

Fig. 4-3 Normalized rms beam envelopes for a warm-fluid (solid curves) beam equilibrium with $\hat{K} = 4$, and a cold-fluid (dashed curves) beam equilibrium. The rms beam envelope profiles are normalized to $\sqrt{4\varepsilon_{4Dth}S}$. The rest of the system parameters are the same as in Fig. 4-2.

In Fig. 4-4 we plot the contours of the self-field potential at $s = 0$ for the warm-fluid beam equilibrium example shown in Fig. 4-3. The normalized rms beam envelopes for this beam at $s = 0$ are $\hat{x}_{brms} = 1.278$ and $\hat{y}_{brms} = 0.785$. For this particular example, the size of the integration region is chosen to be 16×16 in the normalized coordinates and the step size of the grid is $h = 0.0125$, yielding a 1281×1281 grid. The tolerance for the SOR method is chosen to be 10^{-4}. It is interesting to observe in Fig. 4-5 that the equipotential contours are ellipses. Note that the equipotential contours are more elliptical near the center where the beam is located, and become circular far from the beam, which is consistent with the chosen boundary condition in Eq. (4.3.8) which has axial symmetry, as expected.

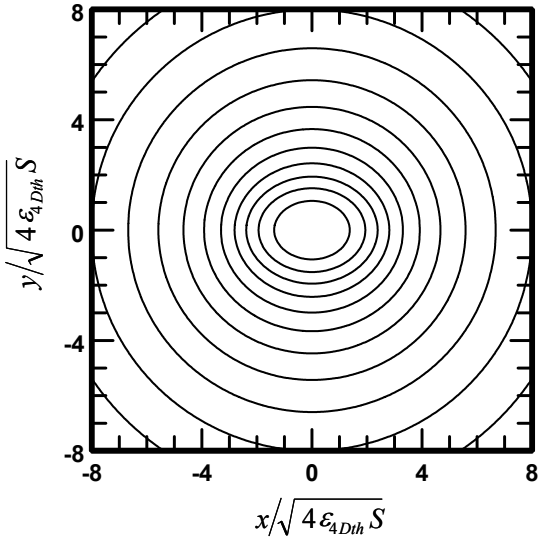

Fig. 4-4 Plot of several equipotential contours at $s = 0$ for the warm-fluid beam shown in Fig. 4-3. The values of $\hat{\phi}/\hat{\phi}_0$ are 0.1, 0.2, 0.3, 0.4, 0.5, 0.6, 0.7, 0.8, 0.9, 1.0, and 1.1, starting from the innermost one, where $\hat{\phi}_0 = \hat{\phi}(\pm 8,0,0) = \hat{\phi}(0,\pm 8,0) = -3.7361$.

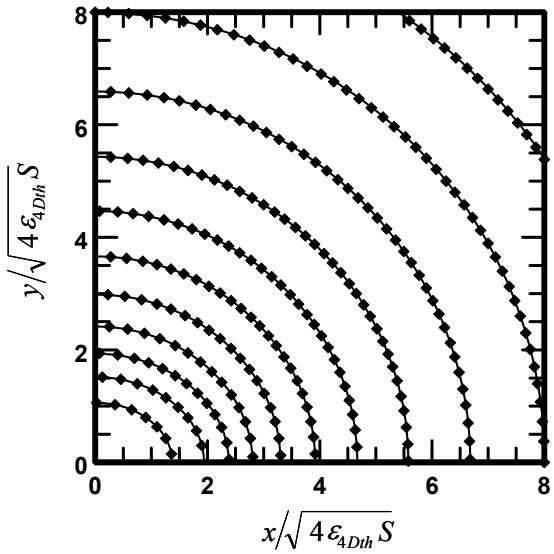

Fig. 4-5 Ellipse fit of the equipotential contours shown in Fig. 4-4, solid lines are the fitted ellipses and the diamonds are the points on the equipotential contours from Fig. 4-4.

If an equipotential contour is an ellipse, the coordinates of the points on the contour have to satisfy the following equation

$$\frac{\hat{x}^2}{\xi^2}+\frac{\hat{y}^2}{\eta^2}=1, \qquad (4.4.2)$$

where ξ and η are the semi-axis of the ellipse. Equation (4.4.2) can be rewritten as

$$\hat{y}^2=-k\hat{x}^2+d, \qquad (4.4.3)$$

where

$$k=\eta^2/\xi^2 \qquad (4.4.4)$$

and

$$d=\eta^2. \qquad (4.4.5)$$

Fitting the squares of the coordinates of the points on the equipotential contours to a straight line in Eq. (4.4.2) we compute the semi-axis of the ellipses using Eqs. (4.4.4) and (4.4.5). The results are shown in Fig. 4-5.

In Fig. 4-6, we plot five constant-density contours for the same beam as shown in Fig. 4-4. The density profile is calculated using the potential distribution shown in Fig. 4-4. The beam density is normalized to the equivalent KV beam density. It is interesting to observe in Fig. 4-7 that the contours of the constant beam densities are ellipses. To fit ellipses into the contours of constant density the same technique as for the fitting of equipotential contours into ellipses was used.

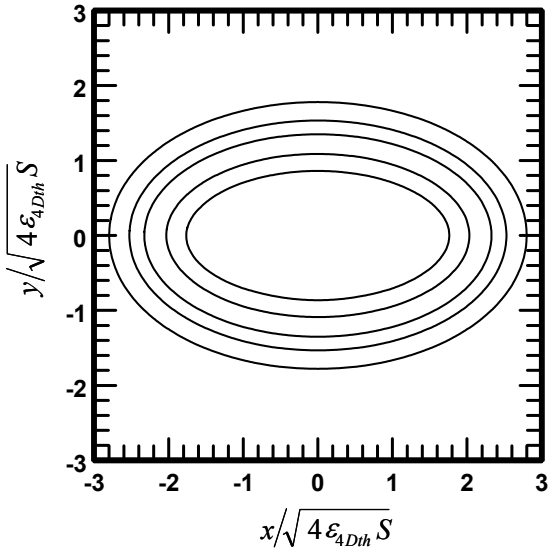

Fig. 4-6 Plot of five contours of constant beam densities at $s = 0$ for the same beam as shown in Fig. 4-4. The values of $n_b^{contour}/n_{KV}(0,0,0)$ are 1.05, 1.0, 0.8, 0.5, and 0.1, starting from the innermost one.

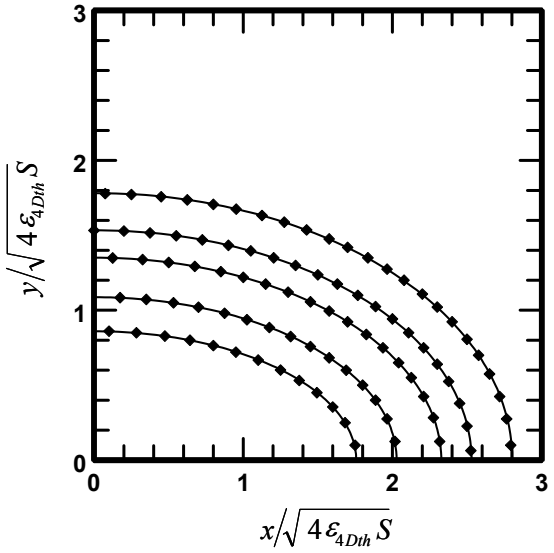

Fig. 4-7 Ellipse fit of the constant-density contours shown in Fig. 4-6, solid lines are the fitted ellipses and the diamonds are the points on the density contours from Fig. 4-6.

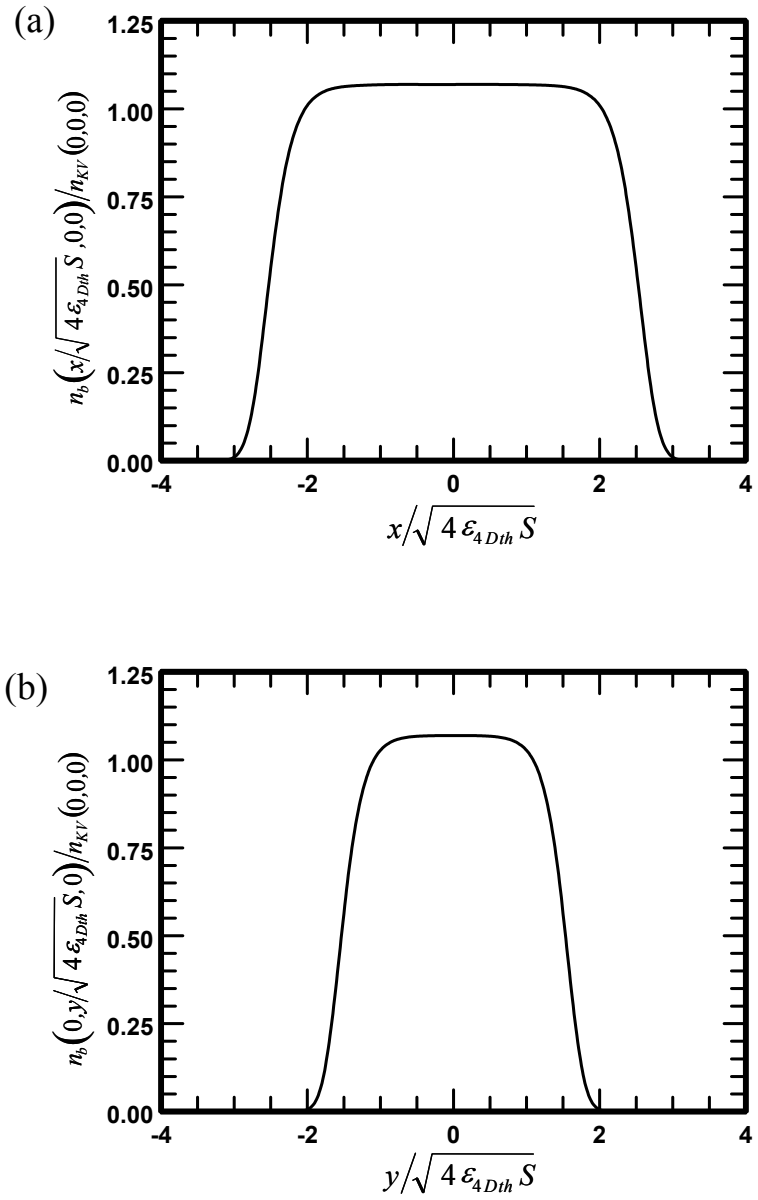

Fig. 4-8 Plot of the beam density profile along (a) $x-$axis and (b) $y-$axis at $s=0$ for the same beam as shown in Fig. 4-3-Fig. 4-7.

In Fig. 4-8(a) and Fig. 4-8(b), we plot the beam density profiles along the $x-$axis and $y-$axis, respectively, for the beam shown in Fig. 4-6. The beam density profile is flat near the center of the beam and then it falls off within a few Debye lengths. Here, the Debye length is defined as

$$\lambda_D \equiv \sqrt{\frac{\gamma_b^2 k_B T_\perp(s)}{4\pi q^2 n_b(0,0,s)}}, \qquad (4.4.6)$$

which is evaluated to be $\lambda_D \Big/ \sqrt{4\varepsilon_{4Dth} S} = 0.171$ for the beam shown in Fig. 4-8. For the warm-fluid beam equilibrium in this example, $x_{brms} \approx 7.5\lambda_D$ and $y_{brms} \approx 4.6\lambda_D$.

Although the constant-density contours are ellipses, the density profile is not self-similar, that is, it does not have the simplest elliptical symmetry as described in Eq. (4.2.22). This is further illustrated in Fig. 4-9, where the percentage difference between the ratio of the semi-axes of constant-density contours and the ratio of the rms envelopes is plotted as a function of the density. In Fig. 4-9 we demonstrate that the beam does not have the simplest elliptical symmetry, i.e., Eq. (4.2.22) is not satisfied. If Eq. (4.2.22) was satisfied the curve on Fig. 4-9 would be horizontal.

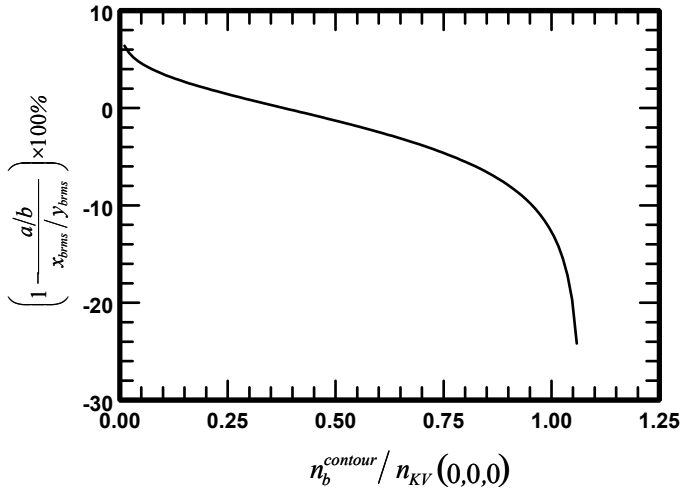

Fig. 4-9 Plot of the difference between the ratio of the semi-axis of the contours of constant density on Fig. 4-8 and the ratio of the rms envelopes sizes in percent.

4.5 Numerical Proof of Averaged Self-Electric Field Relations

We prove numerically the important relations in Eqs. (4.2.23) and (4.2.24). In this proof, we consider several beams propagating in the quadrupole magnetic field with the normalized perveances $\hat{K} = 0.1$, 0.5, 1, 2, 2.5, 3.2, 3.4, 3.8, and 4, and the rest of the parameters are the same as in Fig. 4-3.

First, we check the rms beam envelopes. We calculate numerically the density profiles and use them to compute the rms envelopes of the beams from Eqs. (4.2.7) and (4.2.8). We then compare the numerical rms envelopes with the analytic rms beam envelopes obtained by solving the rms beam envelope equations (4.2.34) and (4.2.35). The results are plotted in Fig. 4-10, where circles correspond to x_{brms} and triangles correspond to y_{brms}. The numerical rms envelopes agree with the analytic rms envelopes within 0.25%.

Second, we use the numerically calculated potential and density profiles to compute the left-hand sides of Eqs. (4.2.23) and (4.2.24), and compare them with the right-hand sides of Eqs. (4.2.23) and (4.2.24), evaluated using the analytical values for the rms beam envelopes. The results are plotted in Fig. 4-11. The difference is less than 0.8%, which is small. Therefore, we conclude that Eqs. (4.2.23) and (4.2.24), are satisfied.

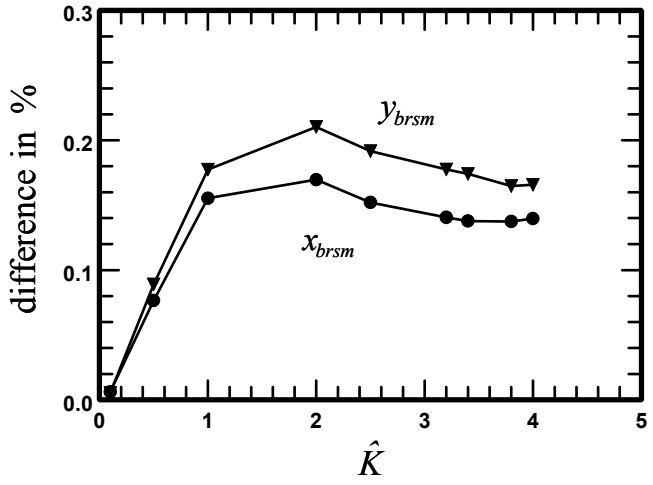

Fig. 4-10 Plots of the percentage differences between the numerical and analytical rms beam envelopes at $s = 0$ for several beams with the normalized perveances $\hat{K} = 0.1$, 0.5, 1, 2, 2.5, 3.2, 3.4, 3.8, and 4, and the rest of the system parameters the same as in Fig. 4-3.

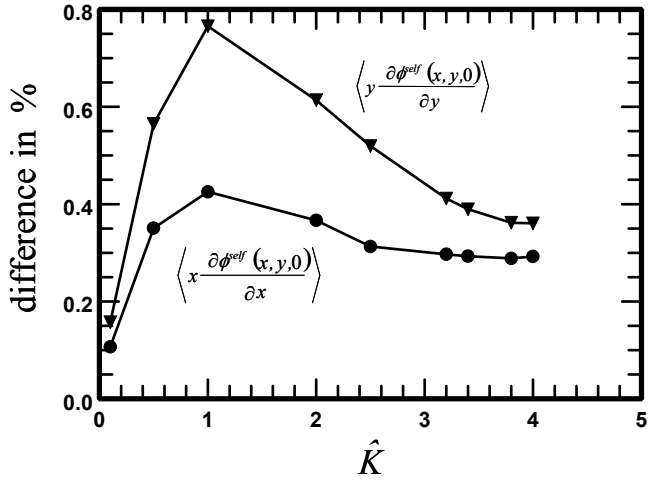

Fig. 4-11 Plots of the percentage differences between $\left\langle x\frac{\partial\phi^{self}(x,y,s)}{\partial x}\right\rangle$ and $-qN_b\frac{x_{brms}(s)}{x_{brms}(s)+y_{brms}(s)}$ (circles); and between $\left\langle y\frac{\partial\phi^{self}(x,y,s)}{\partial y}\right\rangle$ and $-qN_b\frac{y_{brms}(s)}{x_{brms}(s)+y_{brms}(s)}$ (triangles) at $s=0$ for several beams with the normalized perveances $\hat{K}=0.1$, 0.5, 1, 2, 2.5, 3.2, 3.4, 3.8, and 4, and the rest of the system parameters the same as in Fig. 4-3.

4.6 Summary

A paraxial warm-fluid equilibrium theory of a thermal charged-particle beam in a periodic quadrupole magnetic focusing field was presented. The warm-fluid equilibrium equations were solved in the paraxial approximation, and the beam density and flow velocity were obtained. The self-consistent rms beam envelope equations were derived. The self-consistent Poisson equation, governing the beam density and potential distributions, was also derived. The beam motion was considered to be adiabatic, and because of that the 4D thermal rms emittance of the beam is conserved. For such thermal beam equilibria, temperature effects were found to play an important role. Due to

temperature effects, the beam profile is bell-shaped, which is a more realistic representation of the beam density than the uniform density profile in previous theories. For the high-intensity beams the beam density profile is flat in the center of the beam and then it falls off rapidly within a few Debye lengths. An interesting property of the equilibrium is that the rate at which the beam density falls is transversely isotropic. Although the density is not self-similar (which is a key assumption in the classic derivation of the rms envelope equations), the constant-density contours are ellipses.

5 Comparison between Theory and Experiment

5.1 Introduction

The discussion about the thermal beam equilibria cannot be complete without comparisons between theory and experiment. In an ideal thermal beam equilibrium experiment, the beam is in thermal equilibrium when it is generated, it is in thermal equilibrium at the point of its injection into the focusing channel, and it stays in thermal equilibrium as it propagates in the focusing channel.

Several experiments, for example, the UMER [13, 20], the Neutralized Transport Experiment (NTX) [18], and the High Current Experiment (HCX) [17], were designed specifically to explore the physics of high-brightness electron and ion beams. In these experiments, important issues relevant to other accelerator applications that require high-brightness space-charge dominated beams, such as spallation neutron sources, heavy-ion high-intensity accelerator for HIF and HEDP, and high-energy colliders, were studied on small- and full-scale experiments.

In these experiments, the beams were rarely in exact thermal equilibrium. Often times the beam is not in an equilibrium state due to the nonstationary initial distribution. The initial beam distribution has long been recognized as an important factor in determining the evolution of the beam (i.e., rms emittance growth, halo formation, instabilities, etc.). The three most important examples of the nonstationary initial beam distributions are mismatch in the density profile, mismatch in the rms radius, and off-centering, or the combination of these three effects. It is known from thermodynamics that a nonstationary initial beam has a higher total energy per particle than that of the corresponding

stationary beam. The free energy that the nonstationary beam has can then be thermalized by nonlinear space-charge forces, instabilities, or collisions. This produces emittance growth as the beam relaxes toward a final stationary state at a higher kinetic energy per particle [52].

In many experiments, the way the beam is generated and injected into the transport channel creates a nonequilibrium beam distribution. For example, the UMER experiments [34] used a gridded electron gun with a mesh in front of the cathode which perturbed the initial beam current distribution. Also, in the UMER experiments [34, 37] and in the NTX [18], an aperture was used to chop the beam to create a uniform density profile. The aperture, however, created an initial beam distribution that was far from equilibrium around the beam edge, due to the pressure force in the beam created by large density gradient induced by the aperture. The aperture thus introduced the density fluctuations which could lead to wave breaking [53], and transverse wave-like perturbations which created beam hollow density profiles [34, 37]. In the HCX [17], the initial density profile was also far from equilibrium and induced transverse space-charge waves as the beam propagated. Furthermore, the initial non-uniformities in the current density distribution were due to the diode spherical aberrations [54].

Attempts to compare experimental and theoretical beam density profiles have been limited to comparison with the equivalent KV beam density distributions. Indeed, the concept of the equivalent KV beams has often been used in experiments to model intense beams. The concept of equivalent beams was introduced in 1971 by Lapostolle and Sachere [43, 55]. According to this concept, two beams composed of the same particle species and having the same current and kinetic energy are equivalent in an approximate

sense if the second moments of their distributions (i.e., rms beam sizes and emittances) are the same. Although the KV distribution is a good model for the evolution of the rms envelopes of any high-intensity beam, it does not correctly model the actual transverse density profile (see, for example, Fig. 2 in Ref. [34]), and the actual temperature and pressure profiles.

Prior to this thesis, there have been only attempts to draw correlations between the experimental data and the theoretical density profiles of thermal beam equilibria. For a uniform-focusing field such as a uniform solenoidal focusing field, several equilibrium theories predict that in thermal equilibrium for a space-charge dominated beam the beam density profile is flat in the center and falls off in a few Debye lengths at the beam edge [22,56]. The density fall-off has been observed in several experiments, even though the actual beam in the experiment was not in thermal equilibrium [17, 34, 37]. However, a quantitative comparison between theory and experiment has not been made.

In this chapter, we make quantitative comparisons [42] between the equilibrium theories presented in Chapters 2-4 and results of recent experiments at the University of Maryland Electron Ring (UMER) [34, 37] which were made available for this purpose [57]. The thermal equilibria presented in this thesis predicts that for the space-charge dominated beam the beam density profile is flat in the center and then it falls off in a few Debye lengths, for both the periodic solenoidal and quadrupole magnetic focusing fields, and that the Debye length does not change as the beam envelope pulsates. Our equilibrium theories cannot explain several features of the beams observed in experiments, for example, the development of rings or the hollowness of the beam profiles as the beam propagates down the focusing channel. However, in the case of the

periodic solenoidal focusing experiment (see Sec. 5.2), we find good agreement between our theory and experimental measurements from the anode aperture to a distance prior to wave breaking. In the case of the AG focusing experiment (see Sec. 5.3), we also find reasonably good agreement between our theoretical density profile and the experimentally measured density profile in one transverse direction along which the beam is close to a thermal equilibrium.

This chapter is organized as follows. In Sec. 5.2, we compare the equilibrium density profiles for a beam in the measured periodic solenoidal magnetic focusing field using the equilibrium theories presented in Chapters 2 and 3 with the experimental measurements performed on the UMER [34]. In Sec. 5.3, we compare the equilibrium density profiles for a beam in the measured periodic quadrupole magnetic focusing field using the warm-fluid equilibrium theory presented in Chapter 4 with the experimental measurements taken on the UMER [37]. In Sec. 5.4, a summary is presented.

5.2 UMER Experiment with a Periodic Solenoidal Magnetic Focusing Field

The system was a 5 keV electron beam focused by a short solenoidal magnet in one of the experiments on the UMER [34]. In Ref. [34], the electron beam was generated by a gridded gun and exited the gun through an anode aperture at $s = 0$. As discussed in Sec. 5.1, the bell-shaped beam density profiles were imaged by a fluorescent screen while the detailed velocity space distribution was not accessible. The bell-shape beam density profile and the change of the beam density shape as the beam propagates has not been well understood theoretically using previous equilibrium theories, such as the KV beam equilibrium theory.

Using our adiabatic thermal beam equilibrium theories presented in Chapters 2 and 3, we replicate the beam density profiles at different axial distances in good agreement with the experimental measurements [42]. Our equilibrium theory is applicable to this experiment from the anode aperture to a distance prior to wave breaking initiated by high order density distribution fluctuations induced by a pressure force at the anode aperture. Wave breaking [53] occurs at about one quarter of plasma wavelength, which is about 30 cm in this example. Our equilibrium theories in Chapters 2 and 3 can not explain the density distribution distortion in the present form but it is possible to develop a perturbation theory based on the equilibrium in the future.

The calculated rms beam radii from Eq. (2.2.20) or (3.3.9) are shown to agree with the available experimental rms beam radius measurements [34]. In Fig. 5-1, the calculated beam radii $R \equiv \sqrt{2} r_{brms}$ are plotted as solid curves by solving Eq. (2.2.20) for three 5 keV electron beams with currents (emittances): 43 mA ($4\varepsilon_{\tilde{x}rms} = 71$ mm-mrad), 6.5 mA ($4\varepsilon_{\tilde{x}rms} = 30$ mm-mrad) and 1.9 mA ($4\varepsilon_{\tilde{x}rms} = 20$ mm-mrad). The three beams are focused by a short solenoidal magnet whose on-axis magnetic field is shown as a dashed curve. The calculated beam radii for the two beams with currents 43 mA and 1.9 mA agree with the experimental measurements (dotted curves) and previous calculations in Ref. [34], as expected. The calculated beam radius for the 6.5 mA beam will be used for the following density calculations. Note that in this section we are using notation adopted in Chapter 3 and Ref. [42].

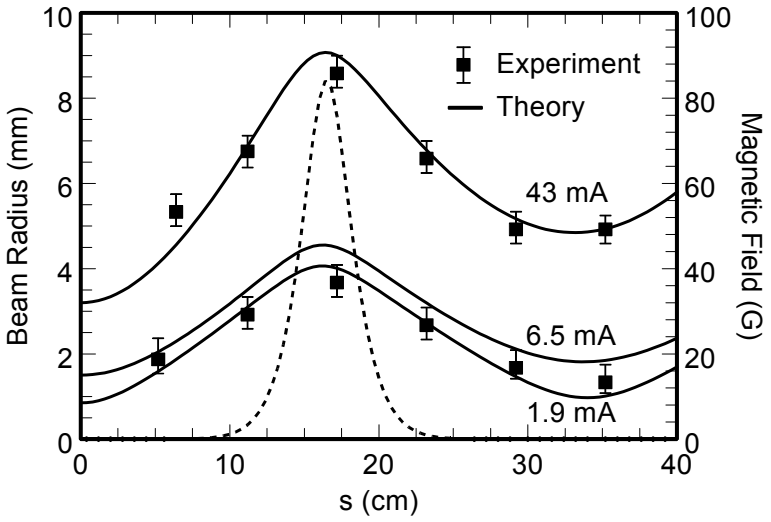

Fig. 5-1. Plots of calculated beam radius $R \equiv \sqrt{2} r_{brms}$ (solid curves) for three 5 keV electron beams with currents (emittances): 43 mA ($4\varepsilon_{\tilde{x}rms} = 71$ mm-mrad), 6.5 mA ($4\varepsilon_{\tilde{x}rms} = 30$ mm-mrad) and 1.9 mA ($4\varepsilon_{\tilde{x}rms} = 20$ mm-mrad). The dotted curves are the available experimental measurement for two beams: 43 mA ($4\varepsilon_{\tilde{x}rms} = 71$ mm-mrad) and 1.9 mA ($4\varepsilon_{\tilde{x}rms} = 20$ mm-mrad). The on-axis magnetic field is shown as a dashed curve [42].

By solving Eqs. (2.2.22) and (2.2.23), or Eqs. (3.3.10) and (3.3.11), we calculate the beam transverse density profiles of the UMER 5 keV, 6.5 mA electron beam at three axial distances: $s = 6.4$ cm, 11.2 cm, and 17.2 cm, as shown as solid curves in Fig. 5-2. The dashed curves are the equivalent KV beam density profiles [34, 43]. Compared with the experimental measurements (dotted curves) (see Ref. [34], Fig. 2), the calculated beam density profiles are in good agreement. As the beam radius increases, the beam density profile approaches to the KV (uniform) beam density profile, because the beam temperature must decrease in order to keep $T_{\perp}(s) r_{brms}^2(s)$ at a constant. In this adiabatic process, the Debye length $\lambda_D \equiv \sqrt{\gamma_b^2 k_B T_{\perp}(s) / 4\pi q^2 n_b(0,s)} = 0.54$ mm is constant [42].

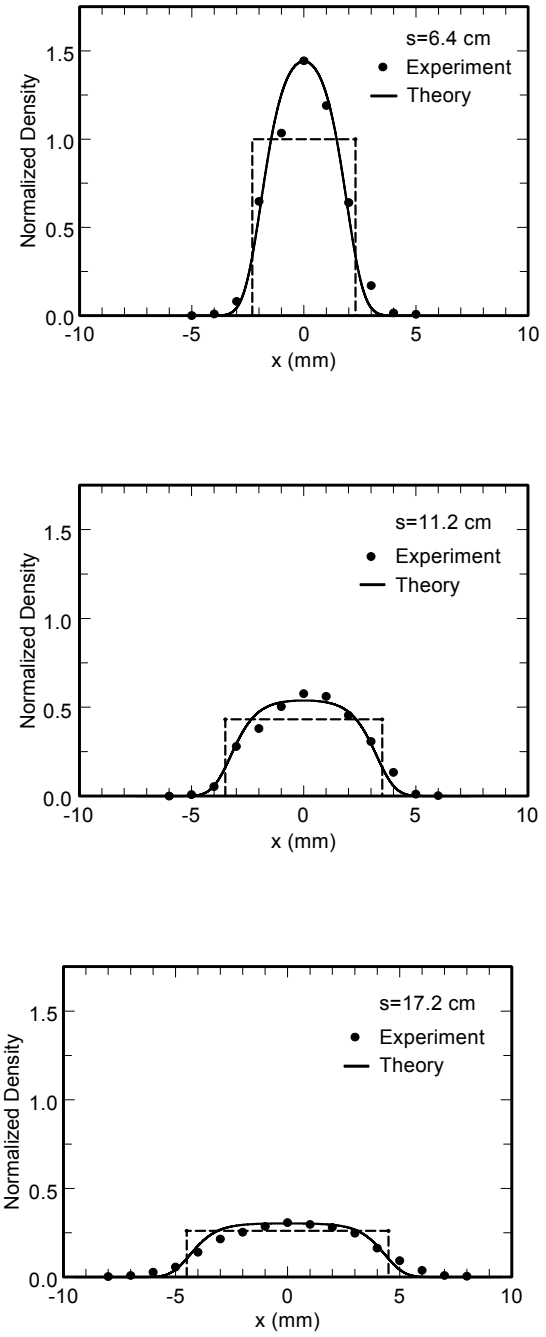

Fig. 5-2. Normalized beam transverse density profiles of a 5 keV, 6.5 mA ($4\varepsilon_{\tilde{x}rms} = 30$ mm-mrad) electron beam at three axial distances: $s = 6.4$ cm, 11.2 cm, and 17.2 cm. The solid curves are from theory, the dotted curves are the experimental measurements, and the dashed lines are the equivalent KV beam density distributions. The densities are normalized to the equivalent KV beam density at $s = 6.4$ cm [42].

5.3 UMER Experiment with a Periodic Quadrupole Magnetic Focusing Field

We analyze the alternating-gradient (AG) focusing experiment presented in Ref. [37]. In this all-quadrupole experiment, the lenses had the same effective length (3.35 cm) and were located at 4.7, 10.5, 20.8, 33.0, 47.3, and 63.3 cm from the aperture. The magnitudes of the peak field gradients were 9.9, 11.6, 7.7, 5.4, 5.4, and 5.8 G/cm. The electron gun, a Pierce-type source, produced 4 keV, 175 mA pulses (5 ms) at a rate of 60 Hz. An aperture, 6.4 mm in diameter, was placed 12.4 cm from the cathode; the aperture size was roughly 1/3 the full beam size at that plane and resulted in an almost uniform, 17 mA beam entering the transport pipe. The beam diagnostics is a 2.54 cm (diameter) phosphor screen that could be moved from the aperture out to a distance of nearly 1 m. The beam pictures were captured with a charge-coupled device (CCD) camera and then digitized and displayed using associated hardware and software [37].

We calculate the effective beam sizes in the $x-$ and $y-$ directions using the envelope equations (4.2.34) and (4.2.35). Hard-edge representation was chosen for the quadrupole focusing field coefficient, which is plotted in Fig. 5-3, where $S = 80$ cm. In Fig. 4-3, effective beam sizes $a \equiv 2x_{brms}$ and $b = 2y_{brms}$ are plotted for a 4keV, 17mA ($4\varepsilon_{4Dth} = 67$ mm-mrad) electron beam.

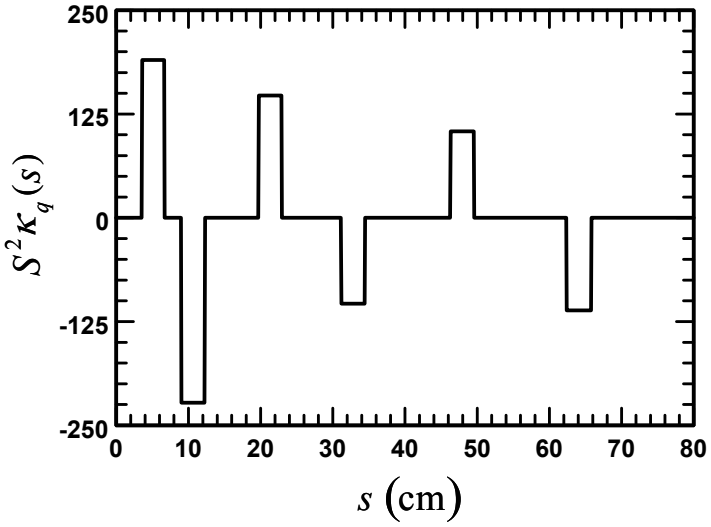

Fig. 5-3 Plot of the normalized quadrupole coupling coefficient $S^2\kappa_q(s)$ versus the axial propagation distance s for the 6-quadrupole lattice.

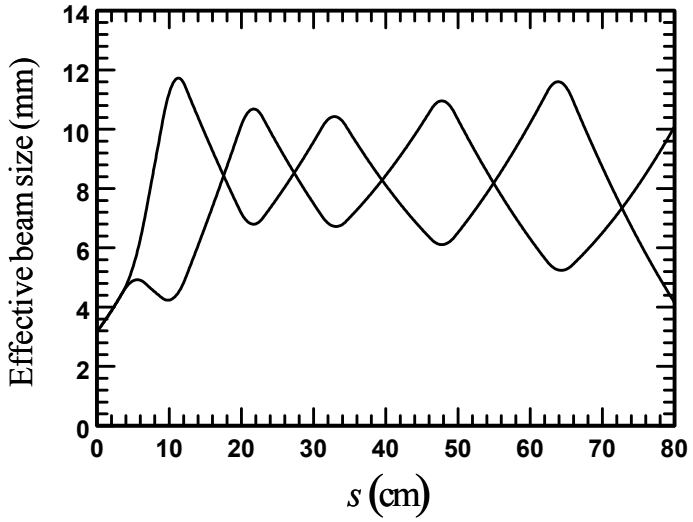

Fig. 5-4 Effective beam sizes in the $x-$ and $y-$ directions for the 4 keV, 17mA ($4\varepsilon_{4Dth} = 67$ mm-mrad) beam focused by a 6-quadrupole lattice with the focusing coefficient $\kappa_q(s)$ presented in Fig. 5-3.

(a) 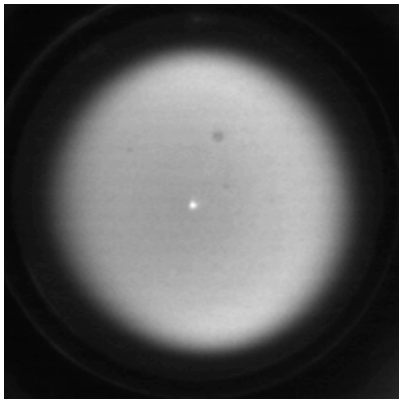 (b) 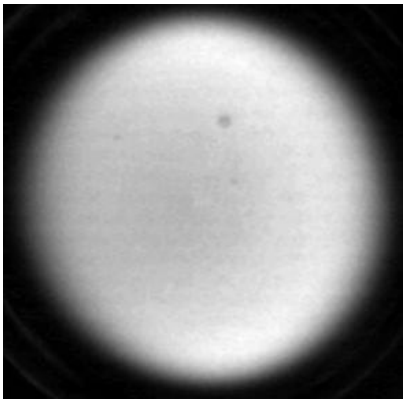

Fig. 5-5. Fluorescent image of the 4 keV, 17 mA ($4\varepsilon_{xrms} = 67$ mm-mrad) electron beam at axial distance $s = 17.3$ cm. (a) Original experimental image and (b) cropped image with subtracted background.

We present the comparison between our theory and the experimental results for the 4 keV, 17 mA ($4\varepsilon_{xrms} = 67$ mm-mrad) electron beam propagating in the AG focusing system [37], at the axial distance $s = 17.13$ cm. The original experimental image [57] is shown in Fig. 5-5(a), the image has 350×350 pixels with the resolution 0.0675+-0.0005 mm/pixel. In our analysis, the image is cropped, and the background is subtracted. The resulting image with 292×288 pixels is shown in Fig. 5-5(b). The bright dot appears in the center of Fig. 5-5(a) because the experimentalists scratched the phosphor screen in the center to set a reference point [57]. We have eliminated this artificial spike in the density profile by smoothing out the profile which is why the bright point is not present in Fig. 5-5(b).

The moments of the experimental density distribution are computed. The first moments of the beam density distribution correspond to the coordinates of the center of the beam, i.e.,

$$x_c(s) = \frac{\iint x n_b(x,y,s)dxdy}{\iint n_b(x,y,s)dxdy} \tag{5.3.1}$$

and

$$y_c(s) = \frac{\iint y n_b(x,y,s)dxdy}{\iint n_b(x,y,s)dxdy}. \tag{5.3.2}$$

After computing the coordinates of the center of the beam, we shift the beam density, such that the center of the beam with coordinates (x_c, y_c) is on the $z-$axis. The second moments of the shifted beam density distribution correspond to the rms sizes of the beam in the $x-$ and $y-$ directions, i.e.,

$$x_{brms}^2(s) = \frac{\iint x^2 n_b(x,y,s)dxdy}{\iint n_b(x,y,s)dxdy} \tag{5.3.3}$$

and

$$y_{brms}^2(s) = \frac{\iint y^2 n_b(x,y,s)dxdy}{\iint n_b(x,y,s)dxdy}. \tag{5.3.4}$$

The 3D plot of the density is shown in Fig. 5-6, where the point $(x=0, y=0)$ corresponds to the center of the beam. The beam density is normalized to the equivalent KV beam density. The red curve corresponds to $n_b(x, y=0, s=17.13\,\text{cm})$, and the blue curve corresponds to $n_b(x=0, y, s=17.13\,\text{cm})$. As can be seen in Fig. 5-6, the beam profile is hollow in the $y-$direction, suggesting that the beam is not in equilibrium. The

rms beam sizes are computed using the beam density profile in Fig. 5-6. The results are $x_{brms} = 4.2807$ mm and $y_{brms} = 4.6122$ mm.

Figure 5-7 shows the comparison between our theory and the experimental data from Fig. 5-6. In Fig. 5-7(a) and Fig. 5-7(b), we plot the beam density profiles along the $x-$axis and $y-$axis, respectively. The solid curves correspond to our theory, the dashed curves represent the equivalent KV beam density, and the dotted curves are from the experimental measurements. The density profile was calculated using Eqs. (4.2.36) and (4.2.37) with the following parameters: $K = 1.015\times10^{-3}$, $x_{brms} = 4.295\,\text{mm}$, $y_{brms} = 4.591\,\text{mm}$, and $\varepsilon_{4Dth} = 16.75\,\text{mm-mrad}$ [37, 57]. In the $x-$direction, there is reasonably good agreement between our theory and the experimental measurements, as shown in Fig. 5-7(a). The rate at which the measured density falls off is well described by the equilibrium theory. However, in the y-direction, there is lack of agreement between the theory and the experiment, as seen in Fig. 5-7(b).

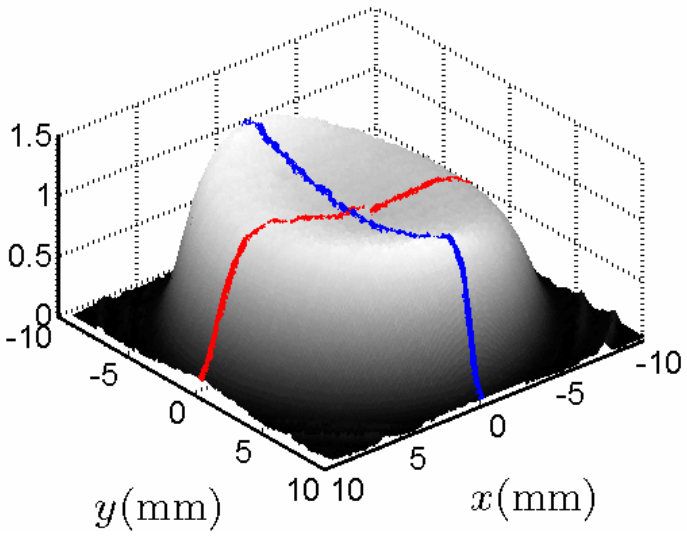

Fig. 5-6. 3D plot of the beam density from Fig. 5-5(b). The red curve corresponds to $n_b(x, y = 0, s = 17.13\,\text{cm})$ and the blue curve corresponds to $n_b(x = 0, y, s = 17.13\,\text{cm})$. The density is normalized to the equivalent KV beam density.

(a)

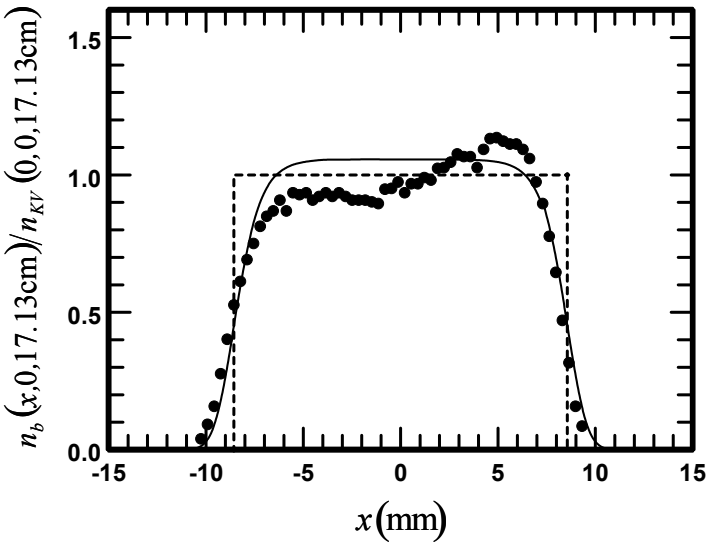

(b)

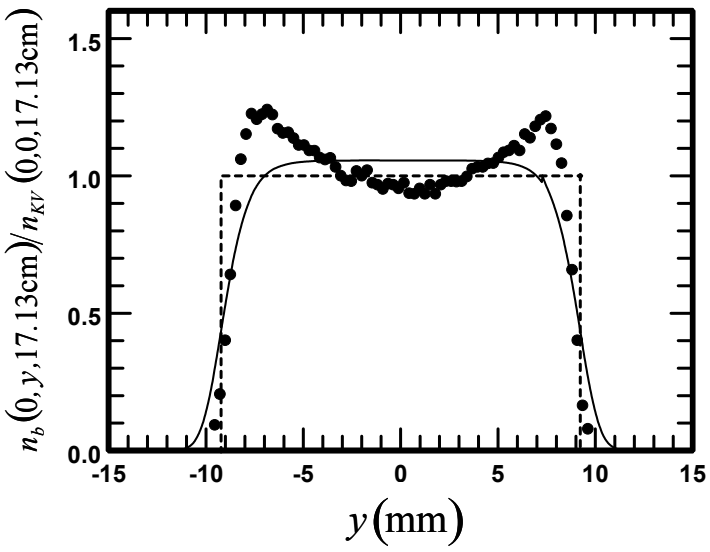

Fig. 5-7. Normalized beam transverse density profiles of a 4 keV, 17 mA ($4\varepsilon_{\tilde{x}rms} = 67$ mm-mrad) electron beam at $s = 17.13$ cm. The solid curves are from theory, the dashed curves are the equivalent KV beam density distributions, and the dotted curves are from the experimental measurements. The density is normalized to the equivalent KV beam density at $s = 17.13$ cm.

We also present comparisons between our theory and experimental measurements for the beam at several other axial positions, $z = 13.43$, 26.83, and 35.28 cm in Fig. 5-8.

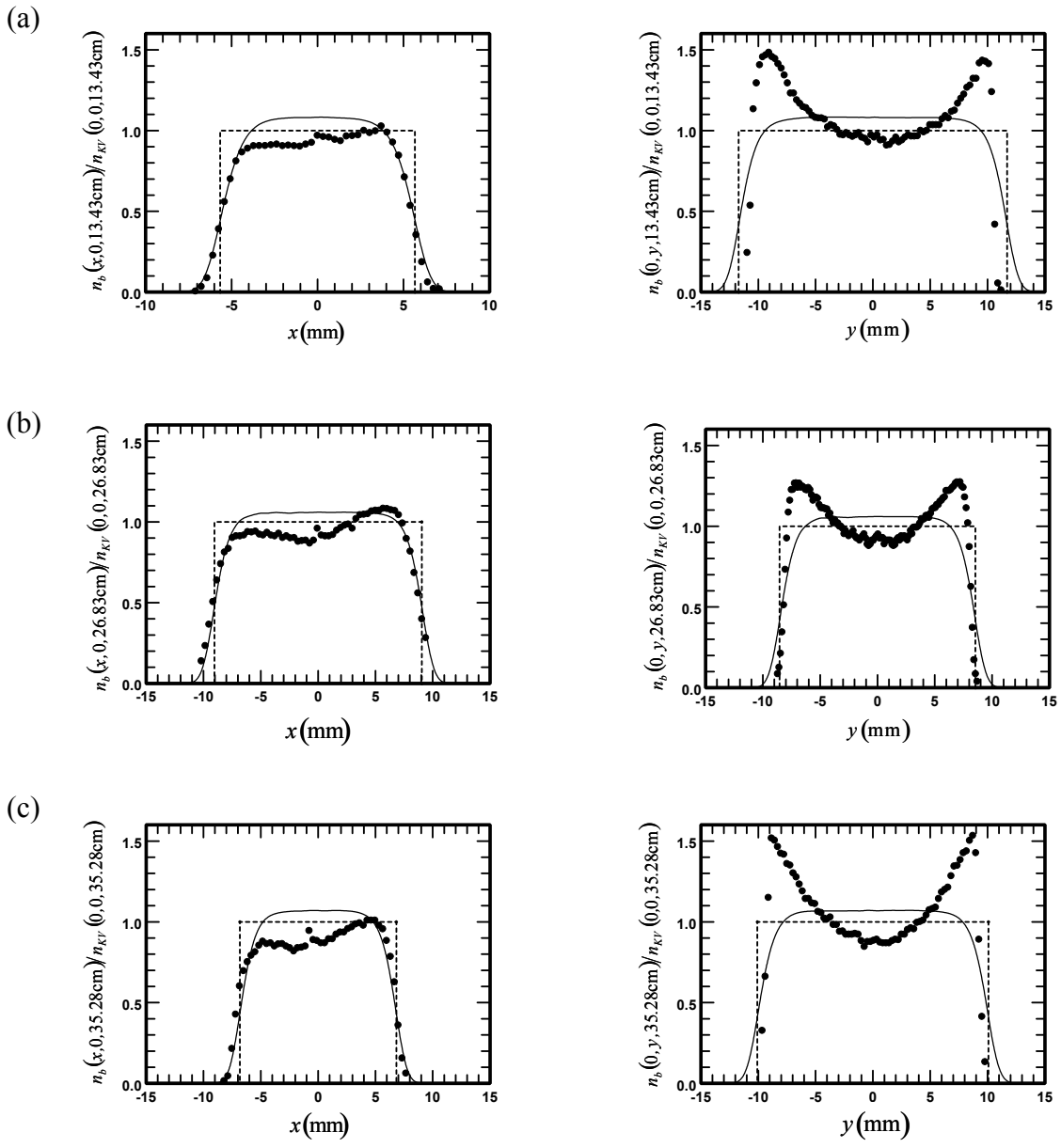

Fig. 5-8. Normalized beam transverse density profiles of a 4 keV, 17 mA ($4\varepsilon_{\tilde{x}rms} = 67$ mm-mrad) electron beam at (a) $s = 13.43$ cm, (b) $s = 26.83$ cm, and (c) $s = 35.28$ cm. The solid curves are from theory, the dashed curves are the equivalent KV beam density distributions, and the dotted curves are from the experimental measurements. The density is normalized to the equivalent KV beam density.

As in the case of the beam at $s = 17.13$ cm in Fig. 5-7, it can be seen in Fig. 5-8 that in the $x-$direction there is reasonably good agreement between our theory and the experimental measurements. The rate at which the measured density falls off is well described by the equilibrium theory. However, in the y-direction, there is lack of agreement between the theory and the experiment.

We give several possible reasons for the discrepancy between theory and experiment shown in Fig. 5-7(b) and Fig. 5-8 (right column). First of all, the beam was not in equilibrium when it entered the focusing channel, because 2/3 of the beam was chopped by the aperture, which introduced a large pressure force on the beam boundary, as was discussed in Sec. 5.1. The pressure force squeezed the beam. As the beam passed the first quadrupole, the magnetic focusing force squeezed the beam in the $x-$direction and stretched it in the $y-$direction. In the $x-$direction, the pressure force introduced by the aperture was in the same direction as the magnetic focusing force. However, in the $y-$direction, the pressure force was in the opposite direction of the magnetic focusing force. That created the ring on the edge of the beam in the $y-$direction, making the slope of the density drop-off steeper.

Secondly, it is evident from the beam density profile in Fig. 5-7(a) that the beam density is not symmetric relative to $x = 0$, suggesting that the quadrupole magnets might have been misaligned in the experiment.

Thirdly, the theory presented in Chapter 4 is developed in the paraxial approximation, assuming the transverse magnetic field is transversely linear. The transverse field from the quadrupole magnets can have some nonlinearities, which may result in distortions in the density profile.

5.4 Summary

A quantitative comparison between our equilibrium theories in Chapters 2, 3, and 4 and recent experiments on the UMER was made. For the case of the periodic solenoidal magnetic focusing field, good agreement was found between the theory and the experiment. For the periodic quadrupole magnetic focusing field, the experimental measurements and theoretical density profiles showed reasonably good agreement in one of the transverse directions. The lack of agreement in the other direction is likely due to the fact that the beam was not in a true thermal equilibrium in the experiment.

6 Conclusions and Future Directions

6.1 Conclusions

In this thesis, we developed a thermal equilibrium theory of periodically focused charged-particle beams in the framework of both warm-fluid and kinetic descriptions. In particular, thermal beam equilibria were discussed for paraxial beams in periodic solenoidal and quadrupole magnetic focusing fields, and the results of the theory were compared with the available experimental measurements [34, 37, 57].

First, we presented a warm-fluid equilibrium theory for a thermal beam in a periodic solenoidal focusing field. The warm-fluid beam equilibrium equations were solved in the paraxial approximation, and the beam density and flow velocity were obtained. The self-consistent rms beam envelope equation and the self-consistent Poisson equation, governing the beam density and potential distributions, were derived. The equation of state for the beam is adiabatic (i.e., there is no heat flow in the system) which results in rms beam emittance being conserved. The beam temperature is constant across the cross-section of the beam. For high-intensity beams, the beam density profile is flat in the center of the beam and falls off rapidly within a few Debye lengths at the edge of the beam. Such a density profile provides a more realistic representation of a laboratory beam than the uniform density profile in the Kapchinskij-Vladimirskij beam equilibrium which had been used in experimental data analyses.

Second, we established a kinetic equilibrium theory for the thermal beam in the periodic solenoidal focusing field which is equivalent to the warm-fluid equilibrium theory. The kinetic equilibrium theory provides more information about the thermal beam

equilibrium, especially the detailed equilibrium distribution function in the particle phase space. The Hamiltonian for single-particle motion was analyzed to find the approximate and exact invariants of motion, i.e., the angular momentum and a scaled transverse Hamiltonian. Using these invariants of motion, a Maxwell-Boltzmann-like beam equilibrium distribution was constructed. The approximation of the scaled transverse Hamiltonian as an invariant of motion was validated analytically for highly emittance-dominated beams and highly space-charge-dominated beams, and was numerically tested to be valid for cases in between with moderate vacuum phase advances ($\sigma_v < 90°$). The beam envelope and emittances were then determined self-consistently with the beam equilibrium distribution.

Third, we presented a warm-fluid equilibrium theory for a thermal beam in a periodic quadrupole magnetic (AG) focusing field, which is a generalization of the warm-fluid equilibrium theory for the thermal charged-particle beam in the periodic solenoidal focusing magnetic field. We considered an adiabatic process and solved the warm-fluid beam equilibrium equations in the paraxial approximation. The rms beam envelope equations and the self-consistent Poisson equation, governing the beam density and potential distributions, were derived. It was shown numerically that the equilibrium equipotential contours and constant density contours are ellipses. Because the thermal beam equilibrium is adiabatic, the 4D thermal rms emittance of the beam is conserved. For high-intensity beams, the beam density profile is flat in the center of the beam and falls off rapidly within a few Debye lengths, which is similar to the beam density profile in the periodic solenoidal focusing field. An interesting property of the equilibrium is that the rate at which the density falls is transversely isotropic.

Finally, we made the quantitative comparisons between the thermal equilibrium theories and recent experiments at the University of Maryland Electron Ring (UMER) [34, 37]. In the case of the periodic solenoidal focusing experiment, we found good agreement between our theory and the experimental measurements from the anode aperture to a distance prior to wave breaking. In the case of the AG focusing experiment, we also found reasonably good agreement between the theoretical and experimentally measured density profiles in one transverse direction along which the beam is close to equilibrium.

6.2 Future Directions

We have gained a fundamental understanding of the thermal equilibrium of the intense charged-particle beams in periodic focusing channels. Our theory is limited to two-dimensional continuous dc beams. Because many charged-particle beams applications require 3D beams or bunched beams, it is important to further explore the physics of space-charge-dominated 3D beams and study the thermal equilibrium properties of such beams. It is well-known that 2D KV beam distribution cannot be extended to bunched beams. It would be interesting to explore the possibility of generalizing our 2D thermal equilibrium theory to a 3D thermal beam equilibrium theory.

It would also be interesting to propose an experiment dedicated to studying the beam equilibrium. Such an experiment would address issues (i.e., beam aperture, magnets misalignment, and magnetic field nonlinearities) that have prevented the beam from being in a true equilibrium. Comparison with the data from such experiments will provide better insight into the applicability of the theoretical thermal beam equilibria presented in this thesis. In addition to providing better insight into the applicability of the theoretical

thermal beam equilibria presented in this thesis, comparison with the data from such experiments may also lead the way towards achieving record high-brightness beams in future beam systems.

Another direction of further research could be a theoretical and numerical study of chaotic particle motion and the possibility of chaos control in the beams using thermal equilibria. Results of such a study could be of significant practical interest to the design and operation of future beam systems.

Appendix A

This Appendix provides a more general derivation of Eqs. (2.2.10), (2.2.12), (2.2.22), (2.2.23), and (2.2.26) in Chapter 2. In particular, starting with the adiabatic equation of state and the radial component of the flow velocity in a more general form, we show that the equation of state can be written in the form of Eq. (2.2.10), and that the radial velocity profile takes a form of Eq. (2.2.12).

A.1 General Formulation of the Problem

We describe beam equilibrium ($\partial/\partial t = 0$) using a warm-fluid description, where we follow the evolution of the particle density $n_b(\mathbf{x})$, the flow velocity $\mathbf{V}(\mathbf{x})$, the flow momentum $\mathbf{P}(\mathbf{x})$, and the pressure tensor $\vec{\vec{\mathbf{P}}}(\mathbf{x})$, defined by

$$n_b(\mathbf{x}) \equiv \int d^3p\, f_b(\mathbf{x},\mathbf{p}), \tag{A.1.1}$$

$$n_b(\mathbf{x})\mathbf{V}(\mathbf{x}) \equiv \int d^3p\, \mathbf{v} f_b(\mathbf{x},\mathbf{p}), \tag{A.1.2}$$

$$n_b(\mathbf{x})\mathbf{P}(\mathbf{x}) \equiv \int d^3p\, \mathbf{p} f_b(\mathbf{x},\mathbf{p}), \tag{A.1.3}$$

$$\vec{\vec{\mathbf{P}}}(\mathbf{x}) \equiv \int d^3p [\mathbf{p}-\mathbf{P}(\mathbf{x})][\mathbf{v}-\mathbf{V}(\mathbf{x})] f_b(\mathbf{x},\mathbf{p}), \tag{A.1.4}$$

where $f_b(\mathbf{x},\mathbf{p})$ is the equilibrium distribution function, and the particle velocity $\mathbf{v}$ and the particle momentum $\mathbf{p}$ are related by

$$\mathbf{v} = (\mathbf{p}/m)\left[1+\mathbf{p}^2/m^2c^2\right]^{-1/2}, \tag{A.1.5}$$

where m is the particle rest mass and c is the speed of light in vacuum.

The equilibrium distribution function $f_b(\mathbf{x},\mathbf{p})$ satisfies the equilibrium Vlasov equation

$$\left\{\mathbf{v}\cdot\frac{\partial}{\partial\mathbf{x}}+q\left(\mathbf{E}+\frac{\mathbf{v}\times\mathbf{B}}{c}\right)\cdot\frac{\partial}{\partial\mathbf{p}}\right\}f_b(\mathbf{x},\mathbf{p})=0\,, \tag{A.1.6}$$

where q is the particle charge.

We take moments of the equilibrium Vlasov equation (A.1.6) [22] to obtain the equilibrium continuity equation

$$\nabla\cdot\left[n_b(\mathbf{x})\mathbf{V}(\mathbf{x})\right]=0\,, \tag{A.1.7}$$

and the equilibrium momentum (or force balance) equation

$$mn_b(\mathbf{x})\left[\mathbf{V}(\mathbf{x})\cdot\nabla\right]\left[\gamma_b\mathbf{V}(\mathbf{x})\right]=qn_b(\mathbf{x})\left[\mathbf{E}(\mathbf{x})+\frac{\mathbf{V}(\mathbf{x})\times\mathbf{B}(\mathbf{x})}{c}\right]-\nabla\cdot\vec{\mathbf{P}}(\mathbf{x}), \tag{A.1.8}$$

where we have assumed that there is no heat flow in the system, i.e., the process is adiabatic,

$$\nabla\cdot\vec{\mathbf{Q}}(\mathbf{x})=0\,, \tag{A.1.9}$$

where $\vec{\mathbf{Q}}(\mathbf{x})$ is the heat flow tensor.

Since we consider only an equilibrium state, the equilibrium self-electric field $\mathbf{E}(\mathbf{x})$ can be described by an equilibrium electrostatic self-field potential, $\mathbf{E}(\mathbf{x})=-\nabla\phi^{self}(\mathbf{x})$. The equilibrium electrostatic potential $\phi^{self}(\mathbf{x})$ satisfies Poisson's equation

$$\nabla^2\phi^{self}(\mathbf{x})=-4\pi qn_b(\mathbf{x}). \tag{A.1.10}$$

The equilibrium magnetic field $\mathbf{B}(\mathbf{x})$ is determined self-consistently from Maxwell's equations

$$\nabla\times\mathbf{B}(\mathbf{x})=\frac{4\pi}{c}qn_b(\mathbf{x})\mathbf{V}(\mathbf{x})\,, \tag{A.1.11}$$

$$\nabla\cdot\mathbf{B}(\mathbf{x})=0\,. \tag{A.1.12}$$

A.2 Paraxial Approximation

We specialize to an axisymmetric case ($\partial/\partial\theta = 0$) and denote $s = z$ as the axial coordinate and $r = \sqrt{x^2 + y^2}$ as the radial distance from the beam axis. Furthermore, we consider a thin, charged-particle beam with characteristic radius r_{brms}, propagating in the z-direction through an applied solenoidal field, which can be approximated in the paraxial approximation by [22]

$$\mathbf{B}^{ext}(r,s) = -\frac{1}{2}B_z'(s)r\,\hat{\mathbf{e}}_r + B_z(s)\hat{\mathbf{e}}_z, \tag{A.2.1}$$

where prime denotes the derivative with respect to s.

We assume that the beam has a large kinetic momentum directed predominately in the axial direction, i.e.,

$$|V_z| >> |V_\perp|, \tag{A.2.2}$$

and that the z-component of the flow velocity does not change much. Under these assumptions, we have

$$V_z(r,s) = V_b + \delta V_z(r,s), \tag{A.2.3}$$

where $V_b = const$ and $|\delta V_z(r,s)| << V_b$. The relativistic mass factor

$$\gamma_b(r,s) = \left[1 - \mathbf{V}^2(r,s)/c^2\right]^{-1/2} \tag{A.2.4}$$

can be approximated to the lowest order [36] as

$$\gamma_b(r,s) \cong \gamma_b = \left(1 - \beta_b^2\right)^{-1/2} = const, \tag{A.2.5}$$

where $\beta_b = V_b / c$.

In the thin-beam approximation, $r_{brms} << S$ is assumed, where S is the characteristic scale over which the external axial magnetic field $B_z(s)$ changes. In the paraxial approximation, we also assume $\nu/\gamma_b^3\beta_b^2 << 1$, where $\nu \equiv q^2 N_b / mc^2$ is the Budker parameter of the beam [22], and $N_b = 2\pi \int_0^\infty dr\, r\, n_b(r,s)$ is the number of particles per unit axial length.

Finally, it is convenient to express the equilibrium self-magnetic field, produced mainly by the axial current of the beam, in terms of the vector potential, i.e., $\mathbf{B}^{self}(r,s) = \nabla \times \mathbf{A}^{self}(r,s)$. In the paraxial approximation we can approximate $A_x^{self} = A_y^{self} = 0$, and retain only the transverse self-field component, $\mathbf{B}^{self}(r,s) = \nabla \times \left[A_z^{self}(r,s)\hat{\mathbf{e}}_z\right]$ generated by the axial beam current $\mathbf{J}_b$. In the present paraxial analysis we can assume that $\mathbf{J}_b = q\beta_b c n_b$, so Maxwell's equation for A_z^{self} can be written as

$$\nabla^2 A_z^{self}(\mathbf{x}) = -4\pi q\beta_b n_b(\mathbf{x}). \qquad (\text{A.2.6})$$

Comparing Eqs. (A.1.10) and (A.2.6), we obtain that the self-field potentials ϕ^{self} and $\mathbf{A}^{self}$ are related by the expression $\mathbf{A}^{self} = A_z^{self}\hat{\mathbf{e}}_z = \beta_b \phi^{self}(r,s)\hat{\mathbf{e}}_z$ [22]. Consequently, the equilibrium self-magnetic field is

$$B_\theta^{self}\hat{\mathbf{e}}_\theta = -\beta_b\left(\partial\phi^{self}/\partial r\right)\hat{\mathbf{e}}_\theta. \qquad (\text{A.2.7})$$

A.3 Particle Velocity Profile

We consider a particular equilibrium profile of the transverse beam velocity

$$V_r(r,s) = r\beta_b c u(s) \qquad (A.3.1)$$

and

$$V_\theta(r,s) = r\,\Omega_b(s), \qquad (A.3.2)$$

which corresponds to a beam undergoing rotation with the angular frequency $\Omega_b(s)$ and pulsating radially. Here, $u(s)$ is a free function of the axial coordinate to be determined later [see Eq. (A.5.11)].

A.4 Pressure Tensor and Equation of State

We assume the pressure tensor in Eq. (A.1.8) to be of the diagonal form, i.e.,

$$\ddot{\mathbf{P}}(r,s) = p_\perp(r,s)\left(\hat{\mathbf{e}}_r\hat{\mathbf{e}}_r + \hat{\mathbf{e}}_\theta\hat{\mathbf{e}}_\theta\right) + p_{||}(r,s)\hat{\mathbf{e}}_z\hat{\mathbf{e}}_z\,. \qquad (A.4.1)$$

We can set $p_{||}(r,s) = 0$ without the loss of generality in the present paraxial theory. We relate the transverse pressure to the transverse beam temperature by an ideal gas law

$$p_\perp(r,s) = n_b(r,s)k_B T_\perp(r,s), \qquad (A.4.2)$$

where the transverse temperature $T_\perp(r,s)$ is defined by

$$n_b(r,s)T_\perp(r,s) = \frac{m\gamma_b}{2k_B}\int\left[\mathbf{v}_\perp(r,s) - \mathbf{V}_\perp(r,s)\right]^2 f_b(\mathbf{x},\mathbf{p})d^3\mathbf{p}\,. \qquad (A.4.3)$$

In the case of the adiabatic process, the equilibrium equation of state can be written as [see, for example Ref. [58], page 118]

$$\mathbf{V}\cdot\nabla\left(\frac{p_\perp}{n^2}\right) = 0\,. \qquad (A.4.4)$$

where we pick $\gamma = 2$, since our system is two-dimensional.

Using the continuity equation (A.1.7), we can rewrite the equation of state (A.4.4) as

$$\mathbf{V}\cdot\nabla T_{\perp}+T_{\perp}\nabla\cdot\mathbf{V}=0\,. \qquad (\text{A.4.5})$$

In the paraxial approximation, we can neglect $T_{\perp}\dfrac{\partial V_z}{\partial z}$ in Eq. (A.4.5) because it is small compared to $V_b\dfrac{\partial T_{\perp}}{\partial z}$. This allows us to rewrite Eq. (A.4.5) as

$$ru(s)\frac{\partial T_{\perp}(r,s)}{\partial r}+\frac{\partial T_{\perp}(r,s)}{\partial z}+2u(s)T_{\perp}(r,s)=0\,, \qquad (\text{A.4.6})$$

where use has been made of Eqs. (A.3.1) and (A.2.3). Equation (A.4.6) is a partial differential equation for the transverse beam temperature $T_{\perp}(r,s)$, which should be solved with the appropriate boundary conditions. We are looking for an equilibrium that would be easy to match into the focusing system with a gun which generates the beam. Since at the exit of the gun the beam temperature is usually uniform, a plausible boundary condition is

$$T_{\perp}(r,s=s_0)=const\,. \qquad (\text{A.4.7})$$

On the other hand, at $r=0$ and $r=\infty$ the temperature should be finite, which is the second boundary condition. Under these boundary conditions, we solve Eq. (A.4.6) using the method of separation of variables, i.e.,

$$T_{\perp}(r,s)=R(r)S(s). \qquad (\text{A.4.8})$$

Substituting (A.4.8) into Eq. (A.4.6) yields

$$r\frac{R'(r)}{R(r)}+\frac{S'(s)}{S(s)u(s)}+2=0\,. \qquad (\text{A.4.9})$$

In Eq. (A.4.9) the first term is only a function of r, while the second term is only a function of s, which means that in order to satisfy Eq. (A.4.9), both terms have to be constant, i.e.,

$$r\frac{R'(r)}{R(r)} = k_1 = const\,, \tag{A.4.10}$$

$$\frac{S'(s)}{S(s)u(s)} = k_2 = const\,, \tag{A.4.11}$$

and

$$k_1 + k_2 + 2 = 0\,. \tag{A.4.12}$$

Integrating Eqs. (A.4.10) and (A.4.11) gives

$$R(r) = r^{k_1} + C_1\,, \tag{A.4.13}$$

$$S(s) = C_2\, exp\left[k_2 \int_0^s u(s')ds' \right], \tag{A.4.14}$$

where $C_1 = const$ and $C_2 = const$. Note that in Eq. (A.4.13) the solution with $k_1 = 0$ keeps the temperature finite at $r = 0$ and $r = \infty$. This solution is also consistent with the boundary condition in Eq. (A.4.7). Setting $k_1 = 0$ in Eq. (A.4.12) yields $k_2 = -2$, and the transverse beam temperature is only a function of the axial coordinate s, i.e.,

$$T_\perp(r,s) = T_\perp(s). \tag{A.4.15}$$

Substituting Eqs. (A.4.13)-(A.4.15) into Eq. (A.4.4) yields

$$T_\perp(s)\exp\left(2\int_0^s u(s')ds' \right) = const\,. \tag{A.4.16}$$

A.5 Momentum Equation

We consider the three components of the equilibrium momentum equation (A.1.8), i.e.,

$$n_b(r,s)\left[V_r\frac{\partial V_r}{\partial r}+V_z\frac{\partial V_r}{\partial s}-\frac{V_\theta^2}{r}\right] \tag{A.5.1}$$
$$= \frac{qn_b(r,s)}{\gamma_b m}\left[-\frac{1}{\gamma_b^2}\frac{\partial\phi^{self}(r,s)}{\partial r}+\frac{1}{c}V_\theta B_z\right]-\frac{k_B T_\perp(s)}{\gamma_b m}\frac{\partial n_b(r,s)}{\partial r},$$

$$n_b(r,s)\left[V_r\frac{\partial V_\theta}{\partial r}+V_z\frac{\partial V_\theta}{\partial s}+\frac{V_r V_\theta}{r}\right] \tag{A.5.2}$$
$$= \frac{qn_b(r,s)}{\gamma_b mc}\left[V_z B_r - V_r B_z\right],$$

$$n_b(r,s)\left[V_r\frac{\partial V_z}{\partial r}+V_z\frac{\partial V_z}{\partial s}\right] \tag{A.5.3}$$
$$= \frac{qn_b(r,s)}{m\gamma_b}\left[-\frac{\partial\phi^{self}(r,s)}{\partial s}-\frac{V_r}{c}\beta_b\frac{\partial\phi^{self}(r,s)}{\partial r}-\frac{1}{c}V_\theta B_r\right],$$

where use has been made of Eqs. (A.2.5), (A.2.7), (A.4.2) and (A.4.15). Note that Eq. (A.5.3) is essentially an equation for determining $\delta V_z(r,s)$. Since $\delta V_z(r,s)$ is small, we will not consider Eq. (A.5.3) in the present paraxial analysis. We will treat V_z in Eqs. (A.5.1) and (A.5.2) as a constant, i.e., $V_z \cong V_b = \beta_b c$.

The radial component of the equilibrium momentum equation (A.5.1) can be rewritten as

$$\frac{\partial}{\partial r}ln\left[n_b(r,s)\right] \tag{A.5.4}$$
$$= -\frac{\gamma_b m\ \beta_b^2 c^2 r}{k_B T_\perp(s)}\left\{u^2(s)+u'(s)-\frac{\Omega_b(s)\cdot\left[\Omega_b(s)+\Omega_c(s)\right]}{\beta_b^2 c^2}\right\}$$
$$- \frac{q}{\gamma_b^2 k_B T_\perp(s)}\frac{\partial\phi^{self}(r,s)}{\partial r},$$

where use has been made of Eqs. (A.2.1), (A.3.1) and (A.3.2), and $\Omega_c(s)=qB_z(s)/mc\gamma_b$ is the relativistic cyclotron frequency. Equation (A.5.4) can be integrated to give the density profile

$$
\begin{aligned}
& n_b(r,s) \qquad\qquad (\text{A.5.5}) \\
= \;& f(s)\exp\left(-\frac{\gamma_b m \beta_b^2 c^2 r^2}{2k_B T_\perp(s)}\left\{u^2(s)+u'(s)-\frac{\Omega_b(s)\cdot[\Omega_b(s)+\Omega_c(s)]}{\beta_b^2 c^2}\right\}\right) \\
\times \;& \exp\left\{-\frac{q\phi^{self}(r,s)}{\gamma_b^2 k_B T_\perp(s)}\right\},
\end{aligned}
$$

where $f(s)$ is to be determined later [see Eq. (A.7.6)].

The θ-component of the equilibrium momentum equation (A.5.2) can be written as

$$
n_b(r,s)\left[r\,u(s)\frac{\partial}{\partial r}+\frac{\partial}{\partial s}\right]\left[\Omega_b(s)r^2+\frac{1}{2}\Omega_c(s)r^2\right]=0, \qquad (\text{A.5.6})
$$

where use has been made of Eqs. (A.2.1), (A.3.1) and (A.3.2). Let us introduce the function

$$
g(s)=\Omega_b(s)+\frac{1}{2}\Omega_c(s), \qquad (\text{A.5.7})
$$

and rewrite Eq. (A.5.6) as

$$
n_b(r,s)\left[2u(s)g(s)+g'(s)\right]=0, \qquad (\text{A.5.8})
$$

which yields

$$
u(s)=-\frac{g'(s)}{2g(s)}. \qquad (\text{A.5.9})
$$

Finally, let us introduce the function

$$
g(s)=\rho^{-2}(s), \qquad (\text{A.5.10})
$$

and rewrite Eqs. (A.5.9) and (A.5.7) as

$$
u(s)=\frac{\rho'(s)}{\rho(s)}, \qquad (\text{A.5.11})
$$

$$
\Omega_b(s)=-\frac{1}{2}\Omega_c(s)+\rho^{-2}(s). \qquad (\text{A.5.12})
$$

Making use of Eq. (A.5.11), the equation of state (A.4.16) can be expressed as

$$T_{\perp}(s)\rho^2(s) = const\,. \qquad \text{(A.5.13)}$$

In the remainder of this Appendix we will show that $\rho(s)$ is proportional to the root-mean squared beam radius $r_{brms}(s)$.

A.6 Root-Mean-Squared Beam Radius

The root-mean-squared (rms) radius of the beam, $r_{brms}^2(s) = \langle r^2 \rangle = N_b^{-1}\int_0^{\infty} 2\pi\, n_b(r,s) r^3 dr$, is an important property of the beam distribution. We calculate the rms beam radius, making use of Eqs. (A.5.11), (A.5.12), and the expression for the beam density in Eq. (A.5.5). The result is

$$\begin{aligned} & r_{brms}^2(s) \qquad \text{(A.6.1)} \\ = \;& \frac{k_B T_{\perp}(s)}{\gamma_b m \beta_b^2 c^2}\left\{\frac{\rho''(s)}{\rho(s)} - \frac{\Omega_b(s)\cdot[\Omega_b(s)+\Omega_c(s)]}{\beta_b^2 c^2}\right\}^{-1} \\ \times \;& \left[2 - \frac{q}{\gamma_b^2 k_B T_{\perp}(s)}\left\langle r\frac{\partial \phi^{self}(r,s)}{\partial r}\right\rangle\right], \end{aligned}$$

where we have used integration by parts and assumed that the beam density approaches zero at $r = \infty$, and

$$\left\langle r\frac{\partial \phi^{self}(r,s)}{\partial r}\right\rangle = N_b^{-1}\int_0^{\infty} 2\pi\, n_b(r,s) r \frac{\partial \phi^{self}(r,s)}{\partial r} r dr\,. \qquad \text{(A.6.2)}$$

From Poisson's equation (A.1.10) in the paraxial approximation, we have

$$r\frac{\partial \phi^{self}(r,s)}{\partial r} = -2q\int_0^{r} 2\pi n_b(r,s) r dr = -2qN_b(r). \qquad \text{(A.6.3)}$$

We can now simplify Eq. (A.6.2) using Eq. (A.6.3) and $dN_b = 2\pi n_b(r,s) r dr$ to obtain

$$\left\langle r\frac{\partial \phi^{self}(r,s)}{\partial r}\right\rangle = -2N_b^{-1}q\int_0^\infty 2\pi\, n_b(r,s)N_b(r)rdr \qquad (A.6.4)$$

$$= \quad -2qN_b^{-1}\int_0^\infty N_b(r)dN_b = -qN_b.$$

Finally, substituting Eq. (A.6.4) into Eq. (A.6.1), we obtain

$$r_{brms}^2(s) = 2\left[\frac{k_B T_\perp(s)}{\gamma_b m\beta_b^2 c^2} + \frac{q^2 N_b}{2\gamma_b^3 m\beta_b^2 c^2}\right]\left\{\frac{\rho''(s)}{\rho(s)} - \frac{\Omega_b(s)[\Omega_b(s)+\Omega_c(s)]}{\beta_b^2 c^2}\right\}^{-1}, \qquad (A.6.5)$$

and simplify the expression for the beam density profile in Eq. (A.5.5) as

$$n_b(r,s) = f(s)\exp\left(-\frac{r^2}{r_{brms}^2(s)} - \frac{r^2\gamma_b m\beta_b^2 c^2}{k_B T_\perp(s)}\frac{K}{4r_{brms}^2(s)} - \frac{q\phi^{self}(r,s)}{\gamma_b^2 k_B T_\perp(s)}\right), \qquad (A.6.6)$$

where $K \equiv 2N_b q^2/\gamma_b^3 m\beta_b^2 c^2$ is the self-field perveance.

A.7 Continuity Equation

The beam density profile in Eq. (A.6.6) and the velocity profile in Eqs. (A.2.3), (A.3.1) and (A.3.2) have to satisfy the continuity equation (A.1.7). In the paraxial approximation, similarly to the equation of state (A.4.5), we can ignore $n_b\frac{\partial V_z}{\partial z}$ compared to $V_b\frac{\partial n_b}{\partial z}$, and rewrite the continuity equation (A.1.7) as

$$\frac{1}{n_b(r,s)}\frac{\partial n_b(r,s)}{\partial s} + \frac{r\rho'(s)}{\rho(s)}\frac{1}{n_b(r,s)}\frac{\partial n_b(r,s)}{\partial r} + \frac{2\rho'(s)}{\rho(s)} = 0, \qquad (A.7.1)$$

where use has been made of Eqs. (A.3.1) and (A.5.11).

We calculate the first two terms in Eq. (A.7.1) separately, using Eqs. (A.6.6) and (A.5.13). The results are

$$\frac{1}{n_b(r,s)}\frac{\partial n_b(r,s)}{\partial s} \tag{A.7.2}$$
$$= \frac{f'(s)}{f(s)} + \frac{r'_{brms}(s)}{r_{brms}(s)}\frac{r^2}{r^2_{brms}(s)}\left[2+\frac{\gamma_b m\beta_b^2 c^2 K}{2k_B T_\perp(s)}\right] - \frac{\gamma_b m\beta_b^2 c^2 K}{2k_B T_\perp(s)}\frac{r^2}{r^2_{brms}(s)}\frac{\rho'(s)}{\rho(s)}$$
$$- \frac{q}{\gamma_b^2 k_B T_\perp(s)}\frac{\partial\phi^{self}(r,s)}{\partial s} - \frac{q\phi^{self}(r,s)}{\gamma_b^2 k_B T_\perp(s)}\frac{2\rho'(s)}{\rho(s)},$$

and

$$\frac{r\rho'(s)}{\rho(s)}\frac{1}{n_b(r,s)}\frac{\partial n_b(r,s)}{\partial r} \tag{A.7.3}$$
$$= -\frac{\rho'(s)}{\rho(s)}\frac{r^2}{r^2_{brms}(s)}\left[2+\frac{\gamma_b m\beta_b^2 c^2 K}{2k_B T_\perp(s)}\right] - \frac{q}{\gamma_b^2 k_B T_\perp(s)}\frac{r\rho'(s)}{\rho(s)}\frac{\partial\phi^{self}(r,s)}{\partial r}.$$

Substituting Eqs. (A.7.2) and (A.7.3) into the continuity equation (A.7.1) and combining terms, we obtain

$$0 = \frac{r^2}{r^2_{brms}(s)}\left[2+\frac{\gamma_b m\beta_b^2 c^2 K}{2k_B T_\perp(s)}\right]\left[\frac{r'_{brms}(s)}{r_{brms}(s)} - \frac{\rho'(s)}{\rho(s)}\right] + \left[\frac{f'(s)}{f(s)} + 2\frac{\rho'(s)}{\rho(s)}\right] \tag{A.7.4}$$
$$- \frac{q}{\gamma_b^2 k_B T_\perp(s)}\left\{\left[\frac{r\rho'(s)}{\rho(s)}\frac{\partial}{\partial r} + \frac{\partial}{\partial s}\right]\phi^{self}(r,s) + \frac{2\rho'(s)}{\rho(s)}\phi^{self}(r,s)\right\}$$
$$- \frac{\gamma_b m\beta_b^2 c^2 K}{2k_B T_\perp(s)}\frac{r^2}{r^2_{brms}(s)}\frac{\rho'(s)}{\rho(s)}.$$

Since $\rho(s)$ is a free function, we can choose it such that the first term in Eq. (A.7.4) vanishes, i.e.,

$$\rho(s) = A r_{brms}(s),\ A = const. \tag{A.7.5}$$

In Eq. (A.7.4), it is convenient to choose

$$f(s) = \frac{C}{r^2_{brms}(s)}, \tag{A.7.6}$$

where $C = const$, so that the second term vanishes. The remaining terms are small and can be neglected in paraxial approximation (see Sec. 2.2).

The equation of state (A.5.13) now becomes

$$T_{\perp}(s) r_{brms}^{2}(s) = const\,, \tag{A.7.7}$$

the radial component of the flow velocity in Eq. (A.3.1) can be rewritten as

$$V_r(r,s) = r\frac{r'_{brms}(s)}{r_{brms}(s)}\beta_b c\,, \tag{A.7.8}$$

and the beam density in Eq. (A.6.6) can be written as

$$n_b(r,s) = f(s)\exp\left\{-\frac{r^2}{4\varepsilon_{th}^2}\left[\frac{K}{2}+\frac{4\varepsilon_{th}^2}{r_{brms}^2(s)}\right]-\frac{q\phi^{self}(r,s)}{\gamma_b^2 k_B T_{\perp}(s)}\right\}, \tag{A.7.9}$$

where $\varepsilon_{th}^2 = \dfrac{k_B T_{\perp}(s) r_{brms}^2(s)}{2m\gamma_b\beta_b^2 c^2}$ is the rms thermal emittance of the beam as defined in Eq. (2.2.18) and the scalar potential for the self-electric field satisfies the Poisson equation

$$\frac{1}{r}\frac{\partial}{\partial r}\left[r\frac{\partial}{\partial r}\phi^{self}(r,s)\right] = -4\pi q\, f(s)\exp\left\{-\frac{r^2}{4\varepsilon_{th}^2}\left[\frac{K}{2}+\frac{4\varepsilon_{th}^2}{r_{brms}^2(s)}\right]-\frac{q\phi^{self}(r,s)}{\gamma_b^2 k_B T_{\perp}(s)}\right\}. \tag{A.7.10}$$

Equations (A.7.6)-(A.7.10) exactly match Eqs. (2.2.26), (2.2.10), (2.2.12), (2.2.22), and (2.2.23) in Chapter 2, respectively. Therefore, the two derivations are equivalent.

Appendix B

In this Appendix we derive the boundary condition in Eq. (4.3.8), where $qN_b\hat{\phi}_{asymptotic}$ is the asymptotic potential outside of a uniform density elliptical beam corresponding to the equivalent KV beam discussed in Sec. 4.3.

The potential outside of the uniform density elliptical beam is [50]

$$\begin{aligned}&\phi(x,y) \\ &= -2qN_b\left[\ln\left(\frac{\sqrt{a^2+\xi}+\sqrt{b^2+\xi}}{a+b}\right)+\frac{x^2\sqrt{b^2+\xi}+y^2\sqrt{a^2+\xi}}{\left(\sqrt{a^2+\xi}+\sqrt{b^2+\xi}\right)\sqrt{\left(a^2+\xi\right)\left(b^2+\xi\right)}}\right],\end{aligned} \tag{B.1}$$

where a and b are the semi-axes of the elliptical beam cross-section, N_b is the number of particles per unit axial length, and

$$\xi=\frac{1}{2}\left[x^2+y^2-a^2-b^2+\sqrt{\left(x^2+y^2-a^2-b^2\right)^2+4\left(b^2x^2+a^2y^2-a^2b^2\right)}\right]. \tag{B.2}$$

For $\frac{x^2}{a^2}+\frac{y^2}{y^2}>>1$, we can approximate ξ in Eq. (B.2) as

$$\xi\cong x^2+y^2, \tag{B.3}$$

and ϕ in Eq. (B.1) as

$$\phi(x,y)\cong\phi_{asymptotic}(x,y)\equiv -2qN_b\left[\frac{1}{2}+\ln\left(\frac{2\sqrt{x^2+y^2}}{a+b}\right)\right]. \tag{B.4}$$

Since $a=2x_{brms}$ and $b=2y_{brms}$, Eq. (B.4) can be rewritten as

$$\phi(x,y)\cong\phi_{asymptotic}(x,y)\equiv -qN_b\left[1+2\ln\left(\frac{\sqrt{x^2+y^2}}{x_{brms}+y_{brms}}\right)\right]. \tag{B.5}$$

Setting $\phi=\phi_{asymptotic}$ at the boundary gives Eq. (4.3.8) in the normalized variables.

7 References

[1] International Linear Collider Reference Design Report, *http://www.linearcollider.org/cms/?pid=1000025* (2007).

[2] LHC Design Report, *http://ab-div.web.cern.ch/ab-div/Publications/LHC-DesignReport.html* (2005).

[3] H. Wiedemann, *Particle Accelerator Physics I: Basic Principles and Linear Beam Dynamics* (Springer; 2nd ed. edition, 1999).

[4] G. S. Bauer, Nucl. Instrum. Methods Phys. Res. A **463**, 505 (2001).

[5] J. P. Carneiro, R. A. Carrigan, M. S. Champion, P. L. Colestock, H. T. Edwards, J. D. Fuerst, W. H. Hartung, K. P. Koepke, M. Kuchnir, and J. K. Santucci, in *Proceedings of the 1999 Particle Accelerator Conference* (New York, NY, USA, 1999), p. 2027.

[6] H. H. Liu, T. R. Mackie, and E. C. McCullough, Med. Phys. **24**, 1960 (1997).

[7] V. L. Granatstein and I. Alexeff, *High-power microwave sources* (Artech House, Boston, MA, 1987).

[8] V. L. Granatstein, R. K. Parker, and C. M. Armstrong, Proceedings of the IEEE **87**, 702 (1999).

[9] G. Dearnaley, Nature **256**, 701 (1975).

[10] M. A. Plum, Nuclear Physics B - Proceedings Supplements, **154**, 105 (2006).

[11] The University of Maryland Electron Ring, *http://www.umer.umd.edu/*.

[12] M. Reiser, P. G. O'Shea, R. A. Kishek, S. Bernal, P. Chin, S. Guharay, Y. Li, M. Venturini, R. York, and D. Lawton, in *Proceedings of the 1999 Particle Accelerator Conference* (New York, NY, USA, 1999), p. 274.

[13] P. G. O'Shea, M. Reiser, R. A. Kishek, S. Bernal, H. Li, M. Pruessner, V. Yun, Y. Cui, W. Zhang, and Y. Zou, Nucl. Instrum. Methods Phys. Res. A **464**, 646 (2001).

[14] S. Bernal, H. Li, T. Godlove, I. Haber, R. A. Kishek, B. Quinn, M. Reiser, M. Walter, Y. Zou, and P. G. O'Shea, Phys. Plasmas **11**, 2907 (2004).

[15] R. A. Kishek, S. Bernal, Y. Cui, T. F. Godlove, I. Haber, J. Harris, Y. Huo, H. Li, P. G. O'Shea, and B. Quinn, Nucl. Instrum. Methods Phys. Res. A **544**, 179 (2005).

[16] P. A. Seidl, F. M. Bieniosek, C. M. Celata*, et al*, Nucl. Instrum. Methods Phys. Res. A **464**, 369 (2001).

[17] L. R. Prost, P. A. Seidl, F. M. Bieniosek*, et al*, Phys. Rev. ST Accel. Beams **8**, 020101 (2005).

[18] P. K. Roy, S. S. Yu, S. Eylon*, et al*, Nucl. Instrum. Methods Phys. Res. A **544**, 225 (2005).

[19] P. K. Roy, S. S. Yu, E. Henestroza, A. Anders, F. M. Bieniosek, J. Coleman, S. Eylon, W. G. Greenway, M. Leitner, and B. G. Logan, Phys. Rev. Lett. **95**, 234801 (2005).

[20] S. Bernal, G. Bai, B. Beaudoin*, et al*, in *Proceeding of the 12th Advanced Accelerator Concepts Workshop, November 27, 2006*, edited by M. Conde and C. Eyberger (AIP, 2006), p. 94.

[21] M. Reiser, *Theory and Design of Charged Particle Beams* (John Wiley & Sons, Inc., USA, 1994).

[22] R. C. Davidson, *Physics of nonneutral plasmas* (Addison-Wesley, Reading, MA, 1990).

[23] H. Boersch, Z. Phys. **139**, 115 (1954).

[24] S. Ichimaru and M. N. Rosenbluth, Phys. Fluids **13**, 2778 (1970).

[25] A. Piwinski, in *Proceedings of the 9th International Conference on High Energy Accelerators* (Stanford, CA, 1974), p. 405.

[26] J. D. Bjorken and S. K. Mtingwa, Part. Accel. **13**, 115 (1983).

[27] K. Kubo, S. K. Mtingwa, and A. Wolski, Phys. Rev. ST Accel. Beams **8**, 81001 (2005).

[28] J. M. Dawson, Phys. Rev. **118**, 381 (1960).

[29] J. M. Dawson, Phys. Fluids **5**, 445 (1962).

[30] J. M. Dawson, Rev. Mod. Phys. **55**, 403 (1983).

[31] I. M. Kapchinskij and V. V. Vladimirskij, in *Proceedings of the Conference on High Energy Accelerators and Instrumentation* (CERN, Geneva, 1959), p. 274.

[32] F. J. Sacherer, *Transverse Space-Charge Effects in Circular Accelerators* (Univ. of California, Berkley, Lawrence Radiation Laboratory, 1968).

[33] C. Chen, R. Pakter, and R. C. Davidson, Phys. Rev. Lett. **79**, 225 (1997).

[34] S. Bernal, B. Quinn, M. Reiser, and P. G. O'Shea, Phys. Rev. Special Topics-Accel. Beams **5**, 064202 (2002).

[35] R. C. Davidson, H. Qin, and P. J. Channell, Phys. Rev. Special Topics-Accel. Beams **2**, 074401 (1999).

[36] R. C. Davidson, P. Stoltz, and C. Chen, Phys Plasmas **4**, 3710 (1997).

[37] S. Bernal, R. A. Kishek, M. Reiser, and I. Haber, Phys. Rev. Lett. **82**, 4002 (1999).

[38] R. C. Davidson and C. Chen, Particle Accelerators **59**, 175 (1998).

[39] K. R. Samokhvalova, J. Zhou, and C. Chen, in *Proceeding of the 12th Advanced Accelerator Concepts Workshop*, edited by M. Conde and C. Eyberger (AIP, 2006), p. 445.

[40] K. R. Samokhvalova, J. Zhou, and C. Chen, Phys Plasmas **14**, 103102 (2007).

[41] J. Zhou, K. R. Samokhvalova, and C. Chen, in *Advanced Accelerator Concepts, November 27, 2006*, edited by M. Conde and C. Eyberger (AIP, 2006), p. 489.

[42] J. Zhou, K. R. Samokhvalova, and C. Chen, Phys Plasmas **15**, 023102 (2008).

[43] F. J. Sacherer, IEEE Trans. Nucl. Sci. **18**, 1105 (1971).

[44] M. Reiser and N. Brown, Phys. Rev. Lett. **71**, 2911 (1993).

[45] R. C. Davidson, Phys. Rev. Lett. **81**, 991 (1998).

[46] R. C. Davidson and H. Qin, *Physics of Intense Charged Particle Beams in High Energy Accelerators* (Imperial College Press, Singapore, 2001).

[47] G. Schmidt, *Physics of high temperature plasmas* (Academic Press, Inc., New York, 1979).

[48] J. Zhou, B. L. Qian, and C. Chen, Phys Plasmas **10**, 4203 (2003).

[49] E. J. N. Wilson, *An Introduction to Particle Accelerators* (Oxford University Press Inc., New York, 2001).

[50] J. Zhou, *Transport of elliptic intense charged -particle beams* (Massachusetts Institute of Technology, 2006).

[51] G. E. Forsythe and W. R. Wasow, *Finite-difference methods for partial differential equations* (Wiley, New York, 1960).

[52] M. Reiser, J. Appl. Phys. **70**, 1919 (1991).

[53] O. A. Anderson, Part. Accel. **21**, 197 (1987).

[54] J. W. Kwan, F. M. Bieniosek, E. Henestroza, L. Prost, and P. Seidl, Laser Part. Beams **20**, 441 (2002).

[55] P. M. Lapostolle, IEEE Trans. Nucl. Sci. **18**, 1101 (1971).

[56] S. M. Lund and R. C. Davidson, Phys Plasmas **5**, 3028 (1998).

[57] S. Bernal (private communication).

[58] R. J. Goldston and P. H. Rutherford, *Introduction to Plasma Physics* (Institute of Physics Publishing, Bristol, 1995).